ULTRACOLD QUANTUM GASES

by

Zixu Zhang

Bachelor of Science, Nanjing University, 2006

Master of Science, University of Pittsburgh, 2007

Submitted to the Graduate Faculty of

the Kenneth P. Dietrich School of Arts and Sciences in partial

fulfillment

of the requirements for the degree of

Doctor of Philosophy

University of Pittsburgh

2012

UNIVERSITY OF PITTSBURGH

KENNETH P. DIETRICH SCHOOL OF ARTS AND SCIENCES

This dissertation was presented

by

Zixu Zhang

It was defended on

April 4th 2012

and approved by

W. Vincent Liu, Associate Professor, Department of Physics and Astronomy

Rob Coalson, Professor, Department of Chemistry

Gurudev Dutt, Assistant Professor, Department of Physics and Astronomy

David Jasnow, Professor, Department of Physics and Astronomy

Adam Leibovich, Associate Professor, Department of Physics and Astronomy

Dissertation Director: W. Vincent Liu, Associate Professor, Department of Physics and Astronomy

ULTRACOLD QUANTUM GASES

Zixu Zhang, PhD

University of Pittsburgh, 2012

In this thesis, we discuss ultracold quantum gases both in continuum and optical lattices. For the continuum Fermi gases in BCS-BEC crossover, we present an effective field theory study on the recently discovered puzzling damping phenomena on the BCS side of the crossover. We find that in contrast to the previous proposed pair-breaking mechanism of damping, the damping process is due to the interaction between superfluid phonons and thermally excited fermionic quasi particles. Results from our effective field theory are compared quantitatively with experiments, showing a good agreement. For the ultracold fermionic atoms in optical lattices, we propose two novel quantum phases. Firstly, we show that a novel superconducting pairing occurs for spin-imbalanced Fermi gases with the spin up and down Fermi levels lying within the p_x- and s- orbital bands of a quasi-one-dimensional optical lattice. The pairs condense at a finite momentum equal to the sum of the two Fermi momenta of spin up and down fermions, and form a p-orbital condensate. The phase diagram shows that the p-orbital pair condensate occurs in a wide range of fillings. Secondly, we study instabilities of single-species fermionic atoms in the p-orbital bands in two-dimensional square optical lattices. From the nearly-perfect nesting Fermi surfaces, charge density wave and orbital density wave orderings with stripe or checkerboard patterns are found for attractive and repulsive interactions, respectively. The superconducting phase, usually expected of attractively interacting fermions, is strongly suppressed. We also use field theory to analyze the possible liquid crystal phases in our system. For bosons, we study ultracold bosonic atoms loaded in a one-dimensional optical lattice of two-fold p-orbital degeneracy at each site, and find an anti-ferro-orbital, a homogeneous p_x Mott insulator phase and two kinds of superfluid

phases distinguished by the orbital ordering.

TABLE OF CONTENTS

LIST OF FIGURES

PREFACE

I would like to thank my supervisor Prof. W. Vincent Liu, for his continued guidance and support during my PhD study. Prof. Liu has always educated me very patiently with his deep and broad knowledge in physics. I have also got the opportunity to study in the Kavli Institute for Theoretical Physics, University of California, Santa Barbara for one academic year, which he made many efforts to make happen. Moreover, in many other aspects I have learned a lot from him in my personal life. I feel honored to be his first student from the University of Pittsburgh.

I am in indebted to my committee members Prof. Rob Coalson, Prof. Gurudev Dutt, Prof. David Jasnow, and Prof. Adam Leibovich. During the committee meetings, I have benefited a lot from their questions and suggestions, which greatly helps with the completion of my thesis.

I enjoy the fruitful discussions with Mr. Meng Cheng, Prof. Andrew Daley, Mr. Xiaopeng Li, Dr. Chungwei Lin, Dr. Chiu-Man Ho, Dr. Hsiang-Hsuan Hung, Dr. Bin Wang, and Dr. Erhai Zhao. I am grateful for the friendship with Mr. Chengdong Li and Mr. Dongyue Yang.

Finally, I deeply thank my mother Lingling Zhang, my father Jinqiu Zhang, and my wife Xuanzi Tong, for their love and support for me.

1.0 INTRODUCTION

The first realization of Bose-Einstein condensation (BEC) in 1995 [5, 6, 7] opened up a new era of studying quantum degenerate systems of atoms and molecules at very low temperatures. The essential idea of this new area is to use external electric and magnetic fields to generate the potential that atoms experience, and also tune the interaction between them. By cooling down the systems to quantum degenerate temperature, statistical properties, such as transport and phase transition, can then be studied. This new field is a combination of traditional condensed matter physics and atomic, molecular, and optical (AMO) physics. On one hand, compared to conventional condensed matter physics, where people focus on the electronic properties in materials, here the trapping potential of atoms are highly tunable by controlling the external electric and magnetic fields. One can also carry on experiments with bosonic atoms in optical lattices, which cannot be realized with materials. On the other hand, compared to the conventional AMO physics, where the single or few-body atomic systems are studied, this new direction emphasizes the many-body effects of the system, and provides an unconventional platform with ultracold atoms and molecules to study statistical properties of quantum systems. As the beginning of the thesis, a brief history of the development of ultracold quantum gases will be introduced as follows.

For bosons, after the realization of BEC in 1995 [5, 6, 7], people soon moved their interests to ultracold bosons in optical lattices. In 2002, M. Greiner et al. successfully observed the quantum phase transition between superfluid and Mott insulator phases by uploading bosonic ^{87}Rb atoms onto a three-dimensional (3D) cubic optical lattices [8]. This landmark result shows the possibility to use optical lattice systems to experimentally simulate the Hubbard model – a very important and widely used model in condensed matter systems such as high-Tc superconductive material.

In addition to studying the Bose-Hubbard model, various research directions regarding ultracold bosonic systems, such as quantum dynamics [9], have been proposed, appealing to growing interests both theoretically and experimentally. Recently, unconventional BEC of bosons on higher orbital bands of optical lattices [10] has been proposed in several theoretical works [11, 12, 13, 14]. In these two years, more and more experiments have studied the higher-band effects of ultracold bosonic gases in optical lattices, and unconventional superfluidity involving bosons on p- or f- orbital bands has been reported [15, 16, 17].

On the fermionic side, the first achievement of degenerate Fermi gases was obtained by JILA group in 1999 [18], where the Fermi statistics was observed with trapped ^{40}K atoms. Later on, a strongly interacting Fermi gas with divergent scattering length was first reported by Duke group [19]. Afterward, by the spectroscopy measurement of pairing gap [20] and the damping rate measurements [21, 22] , strong evidence indicating superfluidity of unitary Fermi gases (divergent scattering length) [23] was discovered. In 2005, The direct observation of vortex lattice provided definitive evidence for superfluidity nature of such systems [24]. Studies on the damping phenomena were continuously carried on in recent years [25, 4].

In addition to the Bardeen-Cooper-Schrieffer (BCS) to BEC (BCS-BEC) crossover and fermionic superfluidity of bulk Fermi gases, ultracold fermionic atoms in optical lattices comprise a very clean and highly tunable quantum simulator to study the strongly correlated periodic electronic systems, which can shed light in the corresponding electronic materials in condensed matter physics. Although for ultracold atomic systems, some traditional measuring technologies in condensed matter systems such as nuclear magnetic resonance or neutron scattering are difficult to apply, new measuring methods, such as time-of-flight imaging, are much easier to implement rather than in traditional condensed matter systems. In 2005, Köhl et al. successfully observed Fermi surfaces in a 3D cubic optical lattice [26]. Before long, the Mott insulator regime was observed for strongly repulsive lattice fermions [27, 28]. Currently, people are still making effects on trying to observe anti-ferromagnetism for repulsive fermions in optical lattices [29, 30]. In addition to 3D optical lattices, quantum phases in lower dimensions such as Fulde-Ferrell-Larkin-Ovchinnikov (FFLO) [31, 32] superconductivity in quasi-one-dimensional systems can also be studied by optical lattice techniques [33].

1.1 OVERVIEW

In this thesis, the ultracold quantum gases in both continuum and optical lattice systems will be discussed. Ultracold quantum gases include atomic and molecular gases, where the latter has a finite-range dipolar interaction. In this thesis we focus on the atomic gases with effectively short-range interactions. The thesis is organized as follows. In Chapter 2, we will discuss the basic atomic physics, i.e., how the atoms behave in external electric and magnetic fields, and how to tune the interaction between atoms by Feshbach resonance. This chapter provides the background to understand the experimental methods to control ultracold atoms. In Chapter 3, the background on bulk Fermi gases is introduced, including cooling, trapping, and manipulating the bulk Fermi gases, and we will also discuss the sound velocity and collective modes in such systems. In Chapter 4, I will present my study on the damping of collective modes observed in recent experiments [34]. Starting from Chapter 5, we will discuss the ultracold quantum gases in optical lattice systems. Chapter 5 provides some background of optical lattices. In Chapter 6, I will present my work on novel multi-band superconductivity in quasi-one-dimensional optical lattices [35]. In Chapter 7, I will present my study on density wave ordering and liquid crystal phases from p-band single-species fermions [36]. In Chapter 8, I will discuss my joint work with Xiaopeng Li on p-orbital bosons in 1D optical lattices [37]. Chapter 9 is the conclusion of the thesis.

A list of my publications during my PhD study is present as follows.

- Chapter 4

  Finite temperature damping of collective modes of a BCS-BEC crossover superfluid, Zixu Zhang, W. Vincent Liu, Physical Review A **83**, 023617 (2011), arxiv:1007.3694
- Chapter 6

  Modulated pair condensate of p-orbital ultracold fermions, Zixu Zhang, Hsiang-Hsuan Hung, Chiu Man Ho, Erhai Zhao, W. Vincent Liu, Physical Review A **82**, 033610 (2010), arxiv:0910.2431
- Chapter 7

  Stripe, checkerboard, and liquid-crystal ordering from anisotropic p-orbital Fermi surfaces in optical lattices, Zixu Zhang, Xiaopeng Li, W. Vincent Liu, Physical Review A

85, 053606 (2012), arxiv:1105.3387

- Chapter 8

  Time reversal symmetry breaking of p-orbital bosons in a one-dimensional optical lattice, Xiaopeng Li, Zixu Zhang, W. Vincent Liu, Physical Review Letters **108**, 175302 (2012), arxiv:1110.3364

2.0 ATOMIC STRUCTURE

Due to the rich internal energy-level structure, an atom can interact with external electric and magnetic fields to induce effective trapping potentials. In this chapter, we will briefly review the behaviors of a single atom in electric and magnetic fields in Sec. 2.1 and 2.2. In Sec. 2.3, we will introduce the scattering between two atoms with the existence of an external magnetic field, i.e., the Feshbach resonance, which is a key ingredient of ultracold atomic physics.

2.1 ZEEMAN SPLITTING

We first consider the Zeeman splitting of an atom in the external magnetic field. In ultracold atomic experiments, alkali atoms, such as ^{6}Li, ^{40}K, and ^{87}Rb, are usually used. In the following, we will use ^{6}Li atoms as an example. ^{6}Li atom has 3 electrons, 3 protons and 3 neutrons, which is a fermion. It has the nuclear spin $I = 1$, and the outer shell electron is at $2s$ orbital with spin $S = 1/2$ and orbital $L = 0$ as the ground state configuration.

We define $\hat{\mathbf{I}}$, $\hat{\mathbf{L}}$, and $\hat{\mathbf{S}}$ as the nuclear, orbital and spin angular momentum operators, and define $\hat{\mathbf{J}} = \hat{\mathbf{L}} + \hat{\mathbf{S}}$ and $\hat{\mathbf{F}} = \hat{\mathbf{I}} + \hat{\mathbf{J}}$ as the total angular momentum operators for spin-orbital coupling and spin-orbital-nucleus coupling. Since the electron is at $L = 0$ orbital state, the spin-orbital coupling is trivial and $\hat{\mathbf{J}} = \hat{\mathbf{S}}$. The Hamiltonian describing hyperfine electron-nucleus coupling reads

$$\hat{H}_{hf} = A\hat{\mathbf{I}} \cdot \hat{\mathbf{J}} = \frac{A}{2}\left(\hat{\mathbf{F}}^2 - \hat{\mathbf{I}}^2 - \hat{\mathbf{J}}^2\right), \tag{2.1}$$

where A is the coupling constant.

Without external magnetic field, $\hat{\mathbf{F}}$ commutes with Eq. (2.1) and the eigenenergy reads

$$E = \frac{A}{2}\left[F(F+1) - I(I+1) - J(J+1)\right]. \tag{2.2}$$

The energy splitting between $F = I + J = 3/2$ and $F = I - J = 1/2$ is given by

$$\Delta E_{hf} = h\nu_{hf} = \frac{3}{2}A. \tag{2.3}$$

As a result, from the measured value of the hyperfine splitting without external magnetic field, we can obtain the coupling constant A. The measured ν_{hf} is 228MHz [38].

Now we consider the ^{6}Li atom in an external magnetic field in z direction $\mathbf{B} = B\mathbf{e_z}$, where $\mathbf{e_z}$ is the unit vector in z direction. The total Hamiltonian is

$$\hat{H}_B = A\hat{\mathbf{I}}\cdot\hat{\mathbf{J}} + C\hat{J}_z + D\hat{I}_z, \tag{2.4}$$

where

$$C = g_s\mu_B B,\ D = -\frac{\mu}{I}B \tag{2.5}$$

are the coupling constants to the external magnetic field B of the electron and the nucleus. Here $g_s \approx 2$ is the g-factor of electron spin, and $\mu_B = e\hbar/(2m_e)$ is the electron magnetic moment (the Bohr magneton), with e=proton charge and m_e=electron mass. In Eq. (2.5), μ is the nuclear magnetic moment, and we can express it as $\mu = \frac{\mu}{\mu_N}\mu_N$, where $\mu_N = e\hbar/(2m_p)$ with m_p the mass of a proton. In general μ/μ_N is a number of order one.

We can diagonalize Eq. (2.4) in the basis $|m_J, m_I\rangle$ (or $|m_s, m_I\rangle$ since $L = 0$), where $m_s = -1/2, 1/2$ and $m_I = -1, 0, 1$ are the z components of the angular momentum of the electron and the nucleus. Eq. (2.4) conserves the z component of the total angular momentum $m_F = m_I + m_s$, and therefore we can evaluate the energy levels in different subspace labeled by m_F. The result for E_{m_F} is

$$\begin{aligned}
E_{3/2} &= \frac{1}{2}A + \frac{1}{2}C + D, \\
E_{1/2} &= \frac{1}{4}\left[-A + 2D \pm \sqrt{8A^2 + (A + 2C - 2D)^2}\right], \\
E_{-1/2} &= \frac{1}{4}\left[-A - 2D \pm \sqrt{8A^2 + (A - 2C + 2D)^2}\right], \\
E_{-3/2} &= \frac{1}{2}A - \frac{1}{2}C - D.
\end{aligned} \tag{2.6}$$

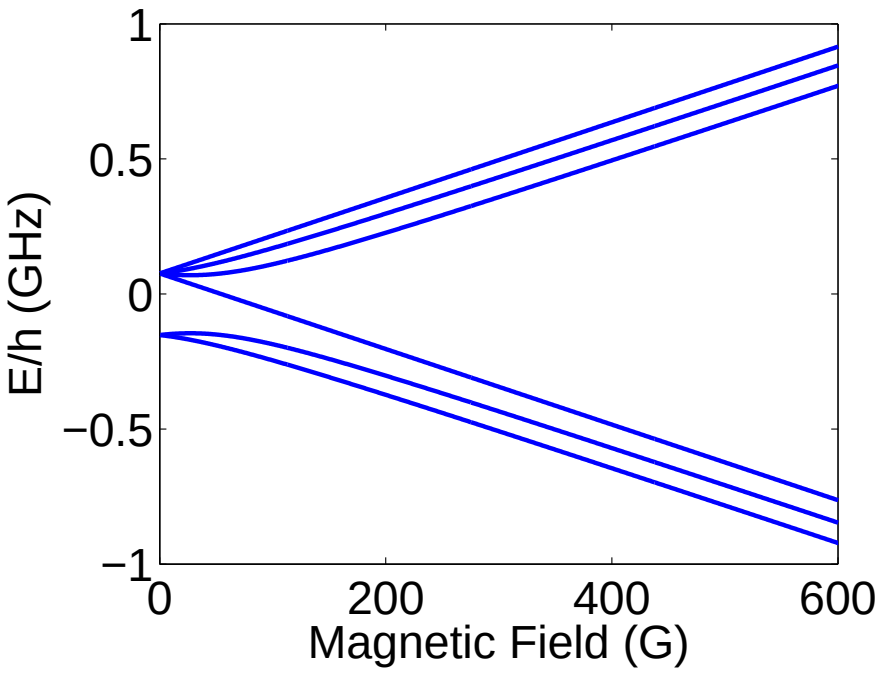

Figure 1: Energy levels of hyperfine states of the ^{6}Li atom with $I = 1$ and $L = 0$ in external magnetic field. Here h is the Planck constant. Notice that, in a large magnetic field where m_s and m_I are approximately good quantum numbers, the states from top to bottom correspond to $|m_s, m_I\rangle = |\frac{1}{2}, 1\rangle, |\frac{1}{2}, 0\rangle, |\frac{1}{2}, -1\rangle, |-\frac{1}{2}, -1\rangle, |-\frac{1}{2}, 0\rangle, |-\frac{1}{2}, 1\rangle$.

As indicated by Eq. (2.5), we have $C/D \sim \mu_B/\mu \sim \mu_B/\mu_N \sim m_p/m_e \sim 2 \times 10^3$, which means D in Eq. (2.6) can be ignored. Using $\nu_{hf} = 228$MHz for ^{6}Li, the energy levels in the external magnetic field are shown in Fig. 1.

2.2 STARK EFFECT

2.2.1 DC Stark Effect

When an atom is placed in an external static electric field $\boldsymbol{\mathcal{E}}_0$, its energy levels are shifted and an electric dipole moment is induced. From a semi-classical point of view, without external

electric field the electrons have the orbit center coincide with the nucleus. When an external electric field is applied, the orbital center of electrons will be moved away from the position of the nucleus. Thus an electric dipole moment is induced. We can define the polarizability $\alpha > 0$ as

$$\mathbf{d} = \alpha \boldsymbol{\mathcal{E}}_0, \tag{2.7}$$

where $\mathbf{d}$ is the induced dipole moment of the atom. The induced electric dipole moment is in the same direction as the external electric field. Therefore, the induced potential energy of the atom is

$$\Delta E = -\frac{1}{2}\alpha |\boldsymbol{\mathcal{E}}_0|^2. \tag{2.8}$$

In quantum mechanics, this effect is the well known DC Stark effect. For simplicity, we consider a two-level system, where the ground state has even parity, and the excited state has odd parity. The external electric field introduces the coupling Hamiltonian

$$\hat{H}' = -\hat{\mathbf{d}} \cdot \boldsymbol{\mathcal{E}}_0, \tag{2.9}$$

where $\hat{\mathbf{d}} = -e\sum_i \hat{\mathbf{r}}_i$ is the dipole moment operator for the electrons with $\hat{\mathbf{r}}_i$ the position operator of the ith electron. By parity consideration it can be shown that the energy shift from the first order perturbation is zero. The general form of second order correction to the energy level m is given by

$$\Delta E_m = \sum_{n \neq m} \frac{|\langle m|\hat{H}'|n\rangle|^2}{E_m - E_n}. \tag{2.10}$$

For a simple two-level system with $|g\rangle$ and $|e\rangle$ as ground state and excited state, we can see from Eq. (2.10) that $\Delta E_g < 0$ and $\Delta E_e > 0$, i.e., the energy levels repel each other.

In experiments, we always prepare the atoms at lower energy states, and the external electric fields couple them to higher energy states. Therefore, we only consider the shift of the ground state energy in a two-level system here. Assuming the electric field is in z direction, the ground state energy shift is

$$\Delta E = \frac{|\langle g|\hat{d}_z \mathcal{E}_0|e\rangle|^2}{E_g - E_e}, \tag{2.11}$$

where $\hat{d}_z$ is the z component of the operator $\hat{\mathbf{d}}$. Comparing Eq. (2.8) and Eq. (2.11), we get the polarizability

$$\alpha = \frac{2|\langle g|\hat{d}_z|e\rangle|^2}{E_e - E_g}. \tag{2.12}$$

2.2.2 AC Stark Effect

In experiments, the electric field is provided by laser beams. Therefore, we need to consider the situation that the AC external electric field is oscillating as $\boldsymbol{\mathcal{E}}(t) = \boldsymbol{\mathcal{E}}_0 \cos\omega t$. Notice that, the electric field of a laser beam $\boldsymbol{\mathcal{E}}(t) = \boldsymbol{\mathcal{E}}_0 \cos(\mathbf{kr} - \omega t)$ is spatially dependent. However, since the size of an atom is much smaller than the laser beam wavelength, a single atom will experience approximately a spatially uniform electric field within the atomic size. Therefore, we can also use $\boldsymbol{\mathcal{E}}(t) = \boldsymbol{\mathcal{E}}_0 \cos\omega t$ for the laser beams.

We can understand the situation here from DC Stark effect discussed in the previous subsection. The perturbation of the Hamiltonian can be written as

$$\hat{H}'' = -\hat{\boldsymbol{d}} \cdot \boldsymbol{\mathcal{E}}(t) = -\frac{\hat{\boldsymbol{d}} \cdot \boldsymbol{\mathcal{E}}_0}{2} \left(e^{i\omega t} + e^{-i\omega t}\right), \tag{2.13}$$

and we can view the two-level atom as dressed in the external photon reservoir with photon frequency ω. The average effect by the photon field is shifting the atomic energy levels by ω, from emitting or absorbing one photon. For example, as the lower level absorb one photon with frequency ω, the energy difference between the ground and excited states becomes $\hbar(\omega_{eg} - \omega)$, instead of $\hbar\omega_{eg}$ in the previous static case. Here we define $\omega_{eg} = (E_e - E_g)/\hbar$, where $\hbar = h/2\pi$ with h the Planck constant. Taking all these process into account, in average the polarizability α can be written down directly from Eq. (2.12) as

$$\begin{aligned} \alpha(\omega) &= |\langle g|\hat{d}_z|e\rangle|^2 \left(\frac{1}{\hbar\omega_{eg} + \hbar\omega} + \frac{1}{\hbar\omega_{eg} - \hbar\omega}\right) \\ &= \frac{2\hbar\omega_{eg}|\langle g|\hat{d}_z|e\rangle|^2}{(\hbar\omega_{eg})^2 - (\hbar\omega)^2}. \end{aligned} \tag{2.14}$$

In Eq. (2.14), when $\omega - \omega_{eg} > 0$, it is called blue detuning, where the laser frequency ω is on the blue side of the resonance frequency ω_{eg}. In this case, we have $\alpha(\omega) < 0$ in Eq. (2.14), which means the energy shift Eq. (2.8) is positive. In other words, the atom experiences a higher potential where the light intensity is stronger, and tends to be repelled from such

regimes. Similarly, it is called red detuning when $\omega - \omega_{eg} < 0$. In this case, we have $\alpha(\omega) > 0$ and the energy shift Eq. (2.8) is negative. Therefore, in this red detuning situation the atom tends to stay in the regimes of stronger light intensity. The attractive or repulsive force can be evaluated as the gradient of the induced energy shift $\Delta E(\mathbf{r})$ in Eq. (2.8), i.e., $\mathbf{F} = -\nabla\left[\Delta E(\mathbf{r})\right]$. In the $\omega \to 0$ (static) limit, Eq. (2.14) reproduces Eq. (2.12) in the DC stark case.

A more rigorous derivation from time-dependent perturbation theory is given as follows. A state in this two-level system can be written in the general form as

$$|\psi(t)\rangle = a_g(t)e^{-i\omega_g t}|g\rangle + a_e(t)e^{-i\omega_e t}|g\rangle. \tag{2.15}$$

Applying Schrödinger equation to $|\psi(t)\rangle$ we obtain

$$\begin{aligned} i\hbar\dot{a}_g &= a_e\langle g|\hat{H}''|e\rangle e^{-i\omega_{eg}t}, \\ i\hbar\dot{a}_e &= a_g\langle e|\hat{H}''|g\rangle e^{i\omega_{eg}t}. \end{aligned} \tag{2.16}$$

Suppose the unperturbed system is at the ground state $|g\rangle$, and we want to study the energy shift of the ground state in the presence of the perturbation $\hat{H}''$. To calculate the first order result, we put in $a_g = 1$ and $a_e = 0$ (zeroth order result) to the right hand side (RHS) of Eq. (2.16), and obtain

$$a_e^{(1)} = \frac{\langle e|\hat{d}_z\mathcal{E}_0|g\rangle}{2\hbar}\left[\frac{e^{i(\omega_{eg}+\omega)t}-1}{\omega_{eg}+\omega} + \frac{e^{i(\omega_{eg}-\omega)t}-1}{\omega_{eg}-\omega}\right] \tag{2.17}$$

after integrating over time. Plugging Eq. (2.17) (first order result) into the RHS of the first equation of Eq. (2.16) we obtain the second order result of a_g as $a_g^{(2)}$. Rewrite $a_g^{(2)} = e^{i\phi_g}$, where ϕ_g is complex. The real part of ϕ_g tells the energy of the state, and the imaginary part tells the amplitude of the state. The first equation of Eq. (2.16) reduces to

$$\hbar\dot{\phi}_g = \frac{\mathcal{E}_0^2}{2\hbar a_g^{(2)}}|\langle e|\hat{d}_z|g\rangle|^2 e^{-i\omega_{eg}t}\cos\omega t\left[\frac{e^{i(\omega_{eg}+\omega)t}-1}{\omega_{eg}+\omega} + \frac{e^{i(\omega_{eg}-\omega)t}-1}{\omega_{eg}-\omega}\right]. \tag{2.18}$$

In RHS of Eq. (2.18), $a_g^{(2)}$ can be replaced by $a_g^{(0)} = 1$ (zeroth order), since we are only interested in the second order perturbation result. The next step is to average Eq. (2.18) over

time, i.e., getting rid of all the time-dependent terms, since these terms are just oscillating with time evolving and the overall effect vanishes. Afterward, we obtain

$$\hbar\langle\dot{\phi}_g\rangle_t = \frac{\mathcal{E}_0^2}{4\hbar}|\langle e|\hat{d}_z|g\rangle|^2\left[\frac{1}{\omega_{eg}+\omega}+\frac{1}{\omega_{eg}-\omega}\right], \tag{2.19}$$

where $\langle ...\rangle_t$ means the average over time. Eq. (2.19) is real, which means the amplitude of the state keeps the same with average over time. Using the fact that the real part of the phase evolving rate is just the energy of the state divided by $\hbar$, $\Delta E = \hbar\langle\dot{\phi}_g\rangle_t$ of the ground state is identified with Eq. (2.19). Meanwhile, the energy shift in the AC field case can be defined in a similar manner that $\Delta E = -\alpha(\omega)\langle|\boldsymbol{\mathcal{E}}(t)|^2\rangle_t/2$. Comparing these two expressions and using $\langle|\boldsymbol{\mathcal{E}}(t)|^2\rangle_t = \mathcal{E}_0^2/2$, $\alpha(\omega)$ derived from this approach is the same as in Eq. (2.14).

2.3 SCATTERING AND FESHBACH RESONANCE

In this section, we will study the scattering of two atoms in the presence of an external magnetic field [23]. We will introduce the Feshbach resonance in ultracold atomic gases, where the scattering length of the collision between two atoms can be tuned by external magnetic field. Feshbach resonance makes it possible to tune the interaction, not only the magnitude, but also the sign of the interaction, which is crucial in ultracold atom experiments.

In a scattering problem, we know that for the low energies where the scattering momentum k is very small, s-wave scattering dominates. The scattering amplitude can be written as

$$f_0(k) = \frac{1}{k\cot\delta_0(k) - ik}, \tag{2.20}$$

where $\delta_0(k)$ is the s-wave phase shift. We can define the scattering length a as

$$-\frac{1}{a} \equiv \lim_{k\to 0} k\cot\delta_0(k). \tag{2.21}$$

Therefore, the scattering amplitude also has the limit $f_0(k) \to -a$ when $k \to 0$. It was shown by Huang and Yang [39] that a zero-range pseudo-potential

$$V_{eff}(\mathbf{r}) = g\delta(r)\frac{\partial}{\partial r}r \tag{2.22}$$

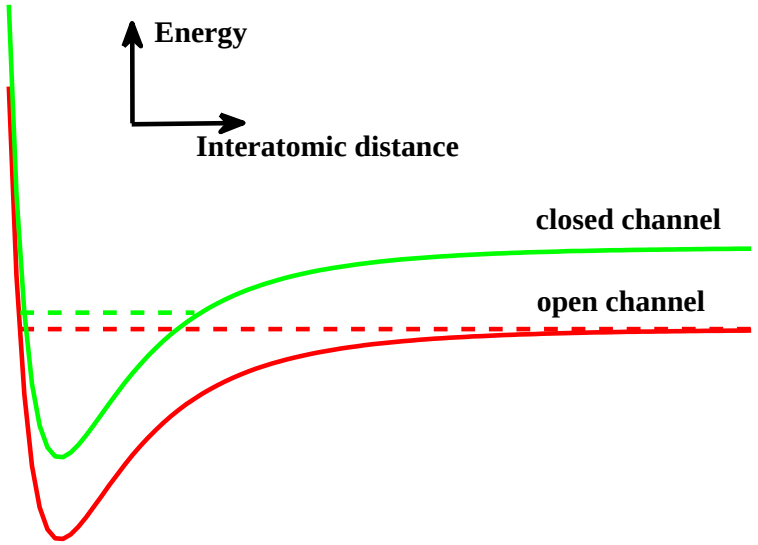

Figure 2: A schematic plot of the two bare channels in the scattering process. Red (Green) solid curve: the potential energy between the two scattering atoms in bare open (closed) channel. Red dashed line: the energy of the free scattering fermions in the open channel. Green dashed line: the energy of the weakly bound fermions in the closed channel. The energy difference of the free scattering and the weakly bound cases, i.e., the difference between the red and green dashed lines, can be tuned by external magnetic field.

can produce the scattering length a. Here $g = 2\pi\hbar^2 a/m_r$, with m_r the reduced mass. For two identical atoms, we have $m_r = m_a/2$ with m_a the mass of the atom.

The scattering length for two particles without internal structure in the scattering channel is fixed and not tunable. Due to the internal energy-level structure of atoms, Feshbach resonance makes it possible to control the scattering length by involving two channels. For ^{6}Li atoms, we use the two lowest energy states in Fig. 1. With magnetic field of hundreds of gauss, these two states have approximately $m_s = -1/2$, and $m_I = 0, 1$. Consider the elastic scattering process between two ^{6}Li atoms 1 and 2, i.e., the internal states of the outgoing atoms after scattering are the same as that of the incoming atoms before scattering. A schematic illustration of energy levels in the scattering process is shown in Fig. 2. During

the scattering, if the states of the two atoms are unchanged, it is called the open channel as shown by the red dashed line in Fig. 2. In this open channel, two $2s$ electrons of the two atoms have the same spins $m_s = -1/2$, so this channel is also called triplet channel. However, due to the hyperfine coupling, it is possible that during the scattering, one of the electron spins is flipped, and the two electrons from the two atoms form a spin singlet, as long as the total spin $m_s^1 + m_s^2 + m_I^1 + m_I^2$ is conserved, with one of the nuclear spins also flipped. In this case, the two atoms form a weakly bound intermediate molecular state, as shown by the green dashed line in Fig. 2. This weakly bound state is called closed channel, or singlet channel. We know that for spin-triplet and spin-singlet states, their magnetic moments are totally different (the nuclear magnetic moment is negligible), which means we can tune the energy difference between spin-triplet open channel (free scattering) and spin-singlet closed channel (weakly bound state) by using the external magnetic field. When the energy of the weakly bound state is close to the energy of scattering state, the free scattering process will have resonance with this weakly bound state, and the scattering length diverges. This resonant divergence is called Feshbach resonance.

The above analysis is incomplete. Near Feshbach resonance, the open channel and closed channel are coupled to each other, and the eigenstates of the system are from the hybridization of the uncoupled (or bare) spin-singlet and spin-triplet states. As a result, the position of Feshbach resonance is not at the magnetic field where the bare open channel has the same energy as the bare closed channel. The actual resonance position is shifted.

In the presence of Feshbach resonance, the scattering length of two atoms is given by

$$a = a_{bg}\left(1 - \frac{\Delta_B}{B - B_0}\right). \tag{2.23}$$

Here, a_{bg} is named the background scattering length, and Δ_B is the width of the resonance. When the external magnetic field reaches the resonance magnetic field B_0, the scattering length a diverges. An illustration of the scattering length of ^{6}Li is shown in Fig. 3. We can see that a changes from positive to negative infinity as an increasing B across B_0, or vice versa.

A more detailed discussion of Feshbach resonance is given in Appendix A. In Sec. 3.2, we will discuss the BCS-BEC crossover of bulk Fermi gases with Feshbach resonance.

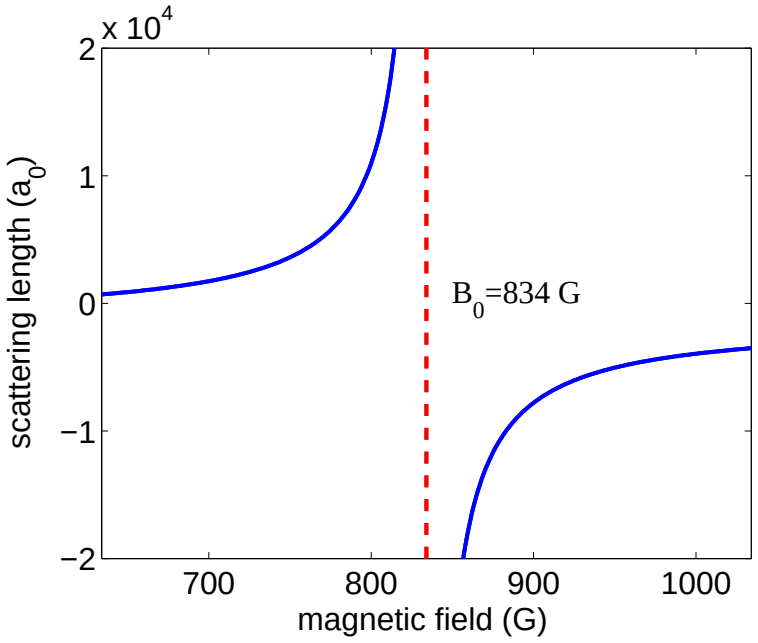

Figure 3: The scattering length (blue solid lines) of ^{6}Li from Eq. (2.23). Here we use the experimental data from Ref. [1] that $B_0 = 834$G (red dashed line), $a_{bg} = -1405a_0$ with a_0 the Bohr radius, and $\Delta_B = -300$G.

3.0 BULK FERMI GASES

In this chapter, we will discuss ultracold bulk fermionic gases. In section. 3.1, we will briefly introduce some experimental methods to trap and cool the quantum gases, including the magneto-optic trap, the far-off resonance trap, and evaporative cooling. In section. 3.2, we will introduce the ultracold bulk fermonic gases with Feshbach resonance in BCS-BEC crossover. In section. 3.3, we will discuss measurable quantities such as sound velocity, frequency and damping rate of collective modes, which can be used to investigate the physical properties of the system.

3.1 TRAPPING AND COOLING

3.1.1 Magneto-Optic Trap

The magneto-optical trap (MOT) is an experimental apparatus that traps and cools the atoms simultaneously. With spontaneously applied magnetic and optical fields, MOT is widely used as the first step to trap and cool the atoms [40].

Consider a two-level atom with resonance frequency ω_r. When a laser beam incident on a rest atom has frequency $\omega_l = \omega_r$, the photon will be absorbed by the atom and the atom acquires the photon momentum. In a MOT, the atoms have non-vanishing velocities in all directions. If we use a red-detuned laser beam with frequency $\omega_l < \omega_r$, the atoms moving in the opposite direction to the propagating laser beam will feel a higher photon frequency ω_l' which is closer to the resonance frequency ω_r. In contrast, the atoms that move in the same direction with the propagating laser beam will experience an even lower photon frequency

ω_l'' away from the resonance. Therefore, in the former case where the atoms move opposite to the laser beam, they are more likely to absorb an photon since ω_l' is closer to ω_r than ω_l'', after which they lose momenta. In other words, the atoms feel an effective Doppler force against its movement. In experiments, two counter-propagating laser beams are applied and we make three of such pairs in x, y and z directions.

After absorbing a photon, the excited atom will re-emit a photon spontaneously in a random direction, where the atom may gain or lose momentum. If originally the atom is fast, i.e., it has the kinetic energy much larger than the recoil energy, in average this absorption and randomly emission process will slow the atom down. The recoil energy is defined as $E_R = \mathbf{q}^2/2m_a$, where $\mathbf{q}$ is the photon momentum and m_a is the mass of the atom.

In experiments, at first the laser frequency is well below the resonance frequency, where the Doppler effect of the fast atoms will induce optical transition as discussed above. These fast atoms will be distinguished by the laser beam, and will gradually lose their momenta by the absorption-emission process. The slow atoms will be less affected, since the Doppler effect is weaker for them, and even the Doppler-shifted laser frequency is off-resonance. Therefore, the whole system is cooling down. As more and more atoms become slower, we need to increase the laser frequency to cool the system further, since now the atoms are slower than before, which means the Doppler effect is weaker and a larger laser frequency has to be applied to reach the resonance.

On the other hand, the optical transition always has a finite frequency width, which means after cooling the system to some certain temperature, we have to use a laser beam with frequency near resonance. In this case, the relatively fast and slow atoms cannot be distinguished by the laser beam due to the finite frequency width of optical transition. Therefore, all the atoms will have the absorption-emission process, and the random emission process will set a low temperature limit, which is called the Doppler limit. To further cool the system, one needs to use other methods, such as the evaporative cooling, which will be discussed later.

The laser cooling provides the optical part of the MOT, which can only cool the system. Since it has no spatial dependence, spatial trapping can not be provided if we only have laser beams. To confine atoms in space, a spatially inhomogeneous magnetic field is also

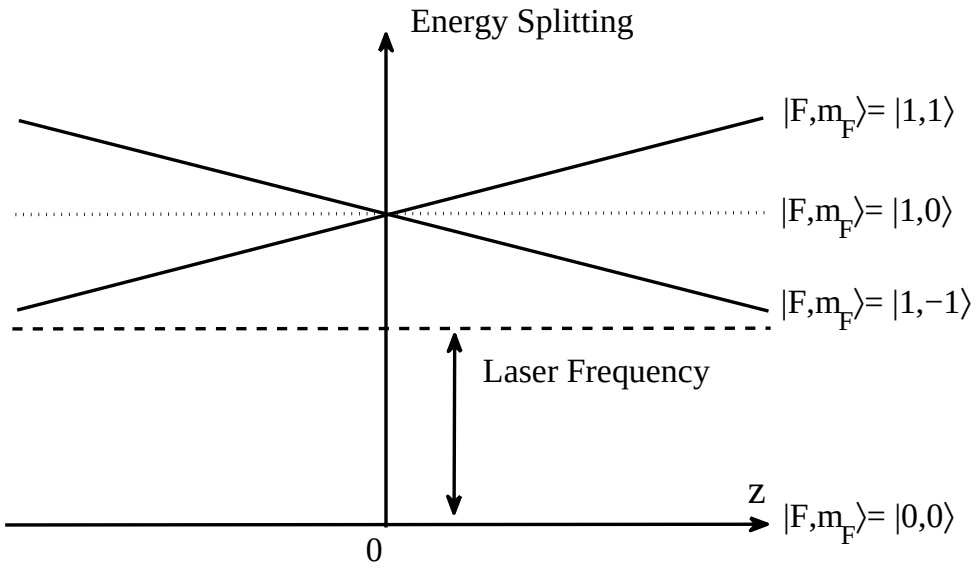

Figure 4: Scheme of the MOT. The spatially inhomogeneous magnetic field causes the Zeeman splitting as shown. We can see that for $z < 0$, the energy difference between $|F, m_F\rangle = |0, 0\rangle$ and $|1, 1\rangle$ is closer to the frequency of the laser beam, which means in this regime a σ_+ photon coupling $|0, 0\rangle$ and $|1, 1\rangle$ propagating from left to right is more likely to be absorbed by the atom. Similarly, for $z > 0$ a σ_- photon propagating from right to left is more likely to be absorbed.

needed. Consider an atom with angular momentum $F = 0, 1$. An inhomogeneous magnetic field is generated such that $\mathbf{B} = B(z)\mathbf{e_z}$, where $B(z) > 0$ for $z > 0$ and $B(z) < 0$ for $z < 0$. Therefore, the $m_F = 0, \pm 1$ states of the $F = 1$ case have the energy level splitting depending on the spatial position of the atom, as shown schematically in Fig. 4. With a red-detuned laser beam of polarization σ_+ propagating from left to right, this laser beam couples the $|F, m_F\rangle = |0, 0\rangle$ atomic state to $|1, 1\rangle$ state. Meanwhile, another red-detuned laser beam of polarization σ_- with the same frequency is propagating from right to left, which couples $|0, 0\rangle$ to $|1, -1\rangle$. As shown in Fig. 4, to the negative z axis, the laser frequency is closer to the energy splitting between $|0, 0\rangle$ and $|1, 1\rangle$ than that between $|0, 0\rangle$ and $|1, -1\rangle$, which means the atom is more likely to absorb the σ_+ photon than σ_- in the left space. Therefore, the

atom in the left space is more likely to absorb the photon propagating to the right, which induces an effective photon pressure towards the origin. Similarly, to the positive z axis, the atom is more likely to absorb the σ_- photon, and the atoms in the right space feel an effective photon pressure to the left, i.e., also towards the origin. It provides the spatial trap of the atoms. Therefore, atoms in the MOT can be trapped and cooled simultaneously.

3.1.2 Far-Off Resonance Trap

As discussed in Chapter 2, a two-level atom experiences an effective potential due to the Stark effect. This electric response is used in the far-off resonance trap (FORT) as the final stage to store and manipulate the ultracold atoms. The laser beam frequency is red-detuned far away from the resonance frequency, so the absorption and emission rates are very small, and the potential is approximately conservative, i.e., the number of atoms at a certain state does not change significantly from optical transition.

In experiments, atoms with the two lowest hyperfine states are used. In the unpolarized case, we have a $50:50$ number ratio for the atoms with two states. For example, with an external magnetic field, we consider a system of ^{6}Li atoms with the two lowest states in Fig. 1 as $1, 2$. FORT couples the atoms at state 1 to a higher p state (not shown in Fig. 1), and induces a Stark trapping potential. Meanwhile, FORT also induces another Stark trapping potential for the atoms at state 2, by couple them to another higher p state. Therefore, the trapping potential reads $U_\sigma = -\frac{1}{2}\alpha_\sigma \langle |\boldsymbol{\mathcal{E}}(t)|^2 \rangle_t$. Here $\sigma = 1, 2$ indicates that the polarizability α_σ depends on whether the ^{6}Li atom is at state 1 or 2. However, in FORT the laser beam is detuned far away from the resonance frequency, and the polarizability is essentially the same for the two components, i.e., α_σ is independent of σ. Such a state-independent trap allows us to treat the system as a two-component system with the same trapping potential for each component.

3.1.3 Evaporative Cooling

In addition to the laser cooling, evaporative cooling is also very widely used in ultracold atomic experiments [40]. Consider a system in a potential trap at thermal equilibrium. By

collisions, some of the particles can gain more energy and escape from the trap, where the remaining particles lose the same amount of energy. The distribution is no long at thermal equilibrium, with more particles occupying the lower energy states. After thermalization, the temperature of the system will decrease. This idea of evaporative cooling can be imagined as similar to the cooling of a cup of hot water. The most energetic water molecules can escape from the surface of water and take away a larger share of energy, and the remaining water will thermalize and becomes colder.

Collisions play a crucial role in evaporative cooling. The atoms are trapped in a finite height potential. By collisions, some atoms can acquire more energy to escape from the trap, and the thermalization for the remaining atoms can happen only via collisions. This is the reason that fermions are more difficult to cool than bosons in experiments. Due to the Pauli-exclusion principle, collisions between fermions are much less frequent than for bosons, since if the final state after collision is occupied, the collision is forbidden. In other words, the available states in phase space for collision is very limited for fermions. Moreover, the *s*-wave scattering between identical fermions is absent. To overcome this limit of collisions for fermions, one solution is to introduce another species of atoms, e.g., one can put bosonic ^{7}Li and fermonic ^{6}Li together, where the former acts like a thermal bath. Since the collisions between ^{7}Li and ^{6}Li are not forbidden and the former can be cooled to a very low temperature, ^{6}Li can also be cooled at the same time.

3.2 BCS-BEC CROSSOVER

Feshbach resonance discussed in Chapter 2 is a key ingredient in bulk ultracold quantum gases, which makes the controlling of the sign and magnitude of interaction experimentally feasible. In this section, we will discuss a 3D Fermi atomic gas with two components, and using external magnetic field to induce Feshbach resonance. With tunable scattering length from negative to positive, BCS-BEC crossover occurs in such systems.

A schematic illustration of the BCS-BEC crossover is shown in Fig. 5. The energies of the bare open and closed channels are the same at magnetic field B_{bare}. However, as discussed

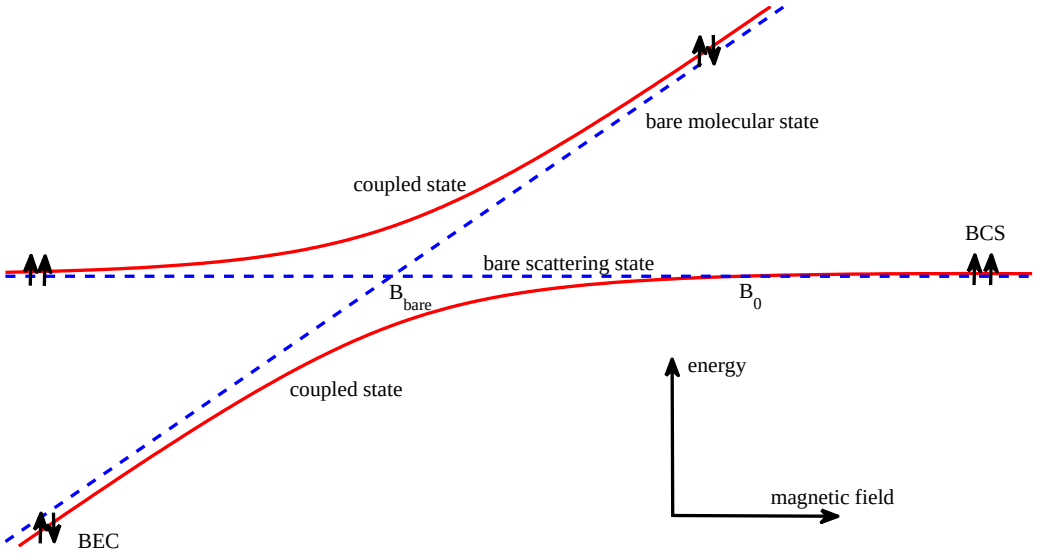

Figure 5: A schematic illustration of the BCS-BEC crossover. Blue dashed lines: the bare open (horizontal) and closed (tilted) channels. Red solid lines: the energy states with coupling between the open and closed channels. $B_{\rm bare}$: the magnetic field at which the energy is the same for the bare open and closed channels. B_0: the resonance magnetic field at which the scattering length diverges, and a bound state emerges. The black arrow indicates the electron spins of the two interacting atoms. For example, for the two lowest states of ^{6}Li in Fig. 1, on the BCS side, the electron spins of the two atoms are the same (spin triplet). On the BEC side, the electron spins inside a tightly bound molecule are opposite (spin singlet).

in Sec. 2.3, due to the coupling between the two bare channels, the actual resonance with divergent scattering length $|a| \to \infty$ is at a shifted magnetic field B_0, where a bound state also emerges. Recall that the scattering length a can be described by Eq. (2.23) as

$$a = a_{bg}\left(1 - \frac{\Delta_B}{B - B_0}\right). \tag{3.1}$$

We start from the BCS side of the crossover to the right of resonance B_0 as shown in Fig. 5, where the scattering length is negative and its amplitude is small. The induced attractive interaction between the two Fermi components can induce superconductivity (fermionic

superfluidity) through the usual BCS mechanism. The two components such as the two lowest states of ^{6}Li atoms have the same electron spin in this case. As we adiabatically decrease the magnetic field, i.e., move to the left in Fig. 5, the Cooper pairs on the BCS side evolve along the lower branch of the red curves, and smoothly become molecules on the BEC side across the Feshbach resonance. On the BCS side, the Cooper pairs are large in space and can be viewed as "fat" molecules. As one moves to the BEC side, the size of the Cooper pairs becomes smaller and smaller, and eventually the two fermionic atoms are tightly bound as a composite molecule, which is a boson with small size. In the composite molecule, two fermionic atoms have opposite electron spins.

When the system reaches the BEC side and assume that we stay in the lower energy branch as discussed before, the scattering length of the original fermions is positive and small. It was shown that the molecular scattering length a_m is connected to the atomic scattering length a on this BEC side as $a_m \approx 0.60a$ [23]. Therefore, the composite bosonic molecules are weakly repulsive. As is well known, the bosonic particles with weakly repulsive interaction is a BEC state, and therefore this positive scattering length side is called the BEC side of the crossover. A 3D weakly interacting Bose gas is known to be a superfluid. Thus we expect bosonic superfluidity on this BEC side. Notice that, although BEC and superfluidity usually appear simultaneously, they are not the same concept. Superfluidity is a transport property, which has non-dissipative and irrotational features, and can be described by a macroscopic wave function. BEC is a massive occupation of the lowest energy state, which is defined in a system at equilibrium. For example, in 2D no BEC occurs for Bose gases, however superfluid can still exist. Also, an ideal 3D Bose gas is a BEC state at low temperature, but no superfluidity is present.

To get the BEC of tightly bound molecules, one has to start from the BCS side and adiabatically sweep magnetic field to the BEC side, in order to stay in the lower branch in Fig. 5. Therefore we call it a BCS-BEC rather than BEC-BCS crossover. If we start from the positive scattering length side, i.e., the left side of Fig. 5, the system will stay in the upper branch if we increase magnetic field, and becomes a strongly repulsive Fermi gas near resonance.

If we sweep magnetic field fast instead of adiabatically, the initial momentum distribution

of BCS Cooper pairs can be obtained [41, 42, 43, 44]. This method is useful if we want to study the superconductivity carrying finite center-of-mass momentum, as we will discuss in Chapter 6.

Since there is no phase transitions observed in experiments, the regime between the BCS and BEC sides is a crossover regime rather than phase transitions. In other words, the fermionic superfluidity on the BCS side is smoothly connected to the bosonic superfluidity on the BEC side. Therefore, the behavior of physical quantities such as phase transition temperature and superfluid density in the BCS-BEC crossover becomes an interesting physical problem.

We first discuss the homogeneous case, i.e., there is no trapping potential. An interesting regime is the resonance limit $|a| \to \infty$, which is also called the unitary limit. This name comes from the scattering theory that when $|a| \to \infty$, the cross section is limited by $\sim 1/k^2$ due to the unitarity of the scattering matrix. In contrast, in the low energy limit, the cross section is limited by $\sim a^2$ [45]. In the unitary limit, all the other length scales are not important, and the only two relevant length scales come from the density (inter-particle distance) and temperature (thermal wavelength). At $T = 0$, only the density matters, and we can define an energy scale E_F from the density as

$$E_F = \frac{\hbar^2}{2m_a}(3\pi^2 n)^{\frac{2}{3}}. \tag{3.2}$$

The atomic mass is denoted by m_a and the gas density is n. This is the Fermi energy of a non-interacting two-species Fermi gas without polarization. The Fermi momentum k_F and Fermi temperature T_F can be defined correspondingly. In the unitary limit, regardless of the component of the Fermi gases, e.g., either ^{40}K or ^{6}Li, we have the universal relationship of the chemical potential $\mu = (1+\beta)E_F$ and the phase transition temperature $T_c = \alpha T_F$, where α and β are universal constants regardless of the gas component. The energy per particle and the pressure of the system are also related to E_F by β as $E/N = (1+\beta)3E_F/5$ and $P = (1+\beta)2nE_F/5$. Therefore, the determination of α and β is related to many physical quantities of the unitary gases. In quantum Monte Carlo study [46, 47], it is shown that $\beta = -0.58 \pm 0.1$ and $\alpha = 0.157 \pm 0.007$ [23].

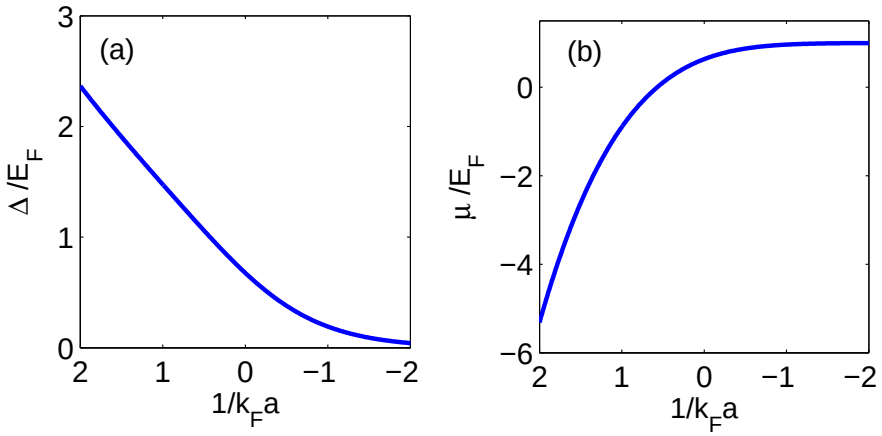

Figure 6: Mean field solution of Eq. (3.3) at $T = 0$. Here Δ is the gap order parameter and μ is the chemical potential.

A basic but widely used theoretical approach of BCS-BEC crossover in this homogeneous case is the mean field theory from single-channel model [48, 49, 50]. The detailed procedure of this approach to get the mean field equations will be discussed in Chapter 4, and we will only present the result here as follows (with Boltzmann constant $k_B = 1$)

$$\begin{aligned} \frac{m_a}{4\pi a} &= \sum_{\mathbf{k}} \left[\frac{1}{2\epsilon_k} - \frac{1}{2E_k} \tanh\left(\frac{E_k}{2T}\right) \right], \\ n &= \sum_{\mathbf{k}} \left[1 - \frac{\xi_k}{E_k} \tanh\left(\frac{E_k}{2T}\right) \right]. \end{aligned} \tag{3.3}$$

In Eq. (3.3), Δ is the gap order parameter, and $E_k = \sqrt{\xi_k^2 + \Delta^2}$ is the energy spectrum of the Fermi Bogoliubov quasiparticle, where $\xi_k = \epsilon_k - \mu$ with $\epsilon_k = \mathbf{k}^2/2m_a$.

In Fig. 6, we shows Δ/E_F and μ/E_F at $T = 0$ by solving Eq. (3.3). This mean field result in Fig. 6 only gives a qualitative picture of the BCS-BEC crossover since fluctuation around the mean field solution is not considered. Quantum Monte Carlo simulations, or a field-theory approach incorporating the fluctuation [51], can give more precise results. It has been shown that the fluctuation can greatly suppress the ordering, i.e., giving a smaller Δ at $T = 0$ compared with Fig. 6 and a lower phase transition temperature T_c.

Now we consider the situation that a harmonic trap is present, where the trapping potential can be described by the quadratic form

$$V = \frac{1}{2}m_a\omega_x^2x^2 + \frac{1}{2}m_a\omega_y^2y^2 + \frac{1}{2}m_a\omega_z^2z^2. \tag{3.4}$$

In real experiments the traps are not in perfect quadratic form, but we will ignore this effect here. In general trapped quantum gases can be studied by local density approximation, where the trapping potential is taken into account as an effective local chemical potential. Local density approximation is applicable if the energy scale of the trapped gas is much larger than the trapping frequency, i.e., $\mu \gg \hbar\omega_{x,y,z}$ [23]. For non-interacting Fermi gases with two components in the trapping potential Eq. (3.4), we can find the following relationship between the chemical potential μ and the total number of particles N to define the effective Fermi energy E_F

$$E_F \equiv \mu = (3N)^{\frac{1}{3}}\hbar\omega_0, \tag{3.5}$$

where we have $\omega_0 = (\omega_x\omega_y\omega_z)^{1/3}$. The Fermi energy E_F Eq. (3.5) in harmonic trap can be defined in another way. Supposing the density at the center of the trap is n_c, the Fermi energy E_F in Eq. (3.5) turns out to be

$$E_F = \frac{\hbar^2}{2m_a}(3\pi^2n_c)^{\frac{2}{3}}. \tag{3.6}$$

It means that the Fermi energy E_F in a harmonic trap coincides with the Fermi energy of a spatial-uniform non-interacting Fermi gas with density the same as the density n_c at the center of the trap.

For interacting Fermi gases in BCS-BEC crossover in the presence of the harmonic trap, in the unitary limit, a similar universal relationship as in the homogeneous can also be found. For example, we have $\mu = \sqrt{1+\beta}E_F$ with the harmonic trap. The β has the same value as before in the homogeneous case.

As we will show in the following section, by manipulating the traps in different manners, collective properties of the trapped gas, such as collective mode frequency and damping rate, can be measured to investigate the state of the system.

3.3 SOUND VELOCITY AND COLLECTIVE MODES

3.3.1 Sound Velocity

Sound velocity is a very important physical quantity not only for Fermi gases exhibiting BCS-BEC crossover, but also for many other physical systems. For Fermi liquids (no superconductivity or other symmetry breaking), the sound velocity is different for collisionless and collisional cases. The latter can be described by classical hydrodynamics, where the collisions between fermions are so frequent that the system can be considered at local equilibrium, and the first (normal) sound can propagate in this case. We can also use the Boltzmann equation to study the sound velocity in this collisional Fermi liquid. In contrast, the fermions barely collide with each other in the collisionless regime, which can only be described by Landau Fermi liquid theory. In this case, the collisionless Boltzmann equation can be used to determine the sound velocity, and the sound propagating here is known as zero sound. It is well known that in Fermi liquids, the first sound and zero sound have different velocities.

If the system is in a superfluid phase, the Fermi liquid theory cannot apply. However, the superfluidity can also be well described by hydrodynamics, since a superfluid can be viewed as an irrotational perfect liquid [52]. Determining the sound velocity can help identify whether the system is in collisionless or hydrodynamic regimes, while it cannot distinguish hydrodynamic superfluid and hydrodynamic collisional Fermi liquid.

We review a very simple theory [53] for the sound velocity of the superfluid phase in BCS-BEC crossover in the homogeneous case by using the well known expression for sound velocity

$$c_s^2 = \frac{n}{m_a}\frac{\partial \mu}{\partial n}. \tag{3.7}$$

Here, we consider $T = 0$ for simplicity. Start from Eq. (3.3) with $T = 0$

$$\begin{aligned} \frac{m_a}{4\pi a} &= \sum_{\mathbf{k}} \left(\frac{1}{2\epsilon_k} - \frac{1}{2E_k} \right), \\ n \equiv \frac{k_F^3}{3\pi^2} &= \sum_{\mathbf{k}} \left(1 - \frac{\xi_k}{E_k} \right). \end{aligned} \tag{3.8}$$

Integrating by parts, Eq. (3.8) reduces to

$$\begin{aligned} \frac{\pi}{2a} &= \frac{\Delta^2+\mu^2}{2m_a}J_2 - \frac{\mu}{2m_a^2}J_4, \\ k_F^3 &= \frac{\Delta^2}{2m_a}J_4, \end{aligned} \tag{3.9}$$

where J_2, J_4 are defined as

$$J_2 = \int_0^\infty dk \frac{k^2}{E_k^3}, J_4 = \int_0^\infty dk \frac{k^4}{E_k^3}. \tag{3.10}$$

By differentiating the first equation in Eq. (3.8), we get $\partial\mu/\partial\Delta = J_2\Delta/J_\xi$, where J_ξ is defined as

$$J_\xi = \frac{1}{2m}J_4 - \mu J_2 = \int_0^\infty dk \frac{k^2\xi_k}{E_k^3}. \tag{3.11}$$

Differentiating the second equation in Eq. (3.8) yields $4\pi^2(\partial n/\partial\mu)_\Delta = J_2\Delta$ and $4\pi^2(\partial n/\partial\Delta)_\mu = J_\xi\Delta$. By putting all these relations together in Eq. (3.7), we get

$$c_s^2 = \frac{1}{3m_a^2}\frac{J_2J_4\Delta^2}{J_2^2\Delta^2+J_\xi^2}. \tag{3.12}$$

We can study some limiting cases of Eq. (3.12). In the deep BCS side, $\Delta \to 0$ and $c_s^2 \to k_F^2/(3m_a^2)$, which is the well known result for the weakly interacting BCS fermionic superfluidity. In the unitary limit where $|1/a| \to 0$, Eq. (3.12) leads to $c_s^2 = 2\mu/(3m_a)$.

In Chapter 4, we will provide a different theoretical approach from effective field theory, which leads to a more general expression of sound velocity at finite temperature. As $T \to 0$, the result in Chapter 4 reproduces Eq. (3.12).

On the experimental side, in 2007 the Duke group reported their result of measuring the sound velocity [54]. They excited a sound wave in a Fermi gas in BCS-BEC crossover regime and then observe the sound propagation at low temperature to extract the sound velocity. The result agrees with multiple theoretical approaches very well, and confirms the hydrodynamic behavior of the system.

3.3.2 Collective Modes

In addition to the sound velocity, measuring collective modes is also a very useful experimental tool to determine the state of the system. Collective mode is the oscillation of the entire trapped gas. Similar as before, on the theoretical side hydrodynamics is widely used to study the collective mode frequency for collisional Fermi liquid and superfluid with traps. The Boltzmann equation can handle both the collisional and collisionless Fermi liquids, but it cannot be used to study the superfluid.

In experiments, there are several kinds of collective modes that can be implemented. For example, for an isotropic trap, a so-called breathing mode [22] can be realized by slightly shrinking or expanding the trap isotropically, after which the bulk gas will oscillate radially as shown in Fig. 7(a). In a 3D isotropic gas, the oscillation of the breathing mode is also isotropic. In contrast, for a cigar-like anisotropic gas, which is more widely used in experiments, the radial breathing mode can be studied by applying the above shrinking and expanding method in the radial direction. Fig. 7(b) shows the quadrupole mode, where the bulk gas oscillates with compression in one dimension and elongation in another. Another class of collective modes is called the scissor mode, where the cigar-like gas is rotated a little bit against the trap, and then oscillates with respect to the trap axis, as shown in Fig. 7(c).

The collective mode is measured by the absorption imaging at a certain time after the excitation [55, 21], where the spatial density profile is read out from the light absorption of the trapped gas. This measurement is destructive, and therefore repeating experiments have to be done to determine the spatial density profile at different instance [22]. The density profile oscillating in time is then fit to extract the oscillation frequency and the damping rate (the decaying of the oscillation amplitude).

In fact, in experiments collective mode is much easier to measure than measuring the sound velocity, and the former experiments were implemented much earlier than the latter. Similarly as in the situation of sound velocity, a collisionless Fermi liquid will in general have different collective mode frequency from that of a collisional Fermi liquid or a superfluid governed by hydrodynamics. However, with a non-rotating gas, measuring the collective mode frequency cannot distinguish the collisional Fermi liquid and the superfluid either,

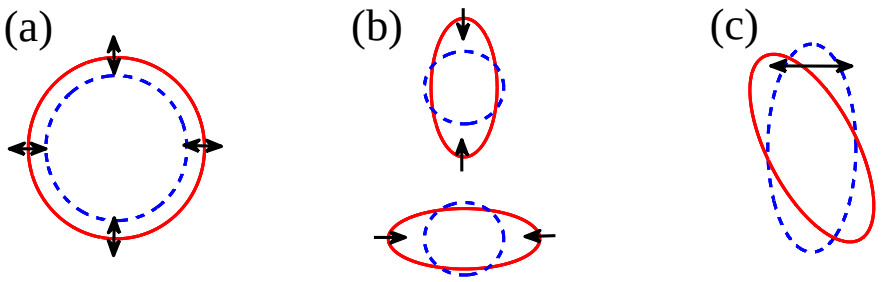

Figure 7: Three types of collective modes in experiments. Red lines indicate the shape of the ultracold gas in space. Blue lines indicate the equilibrium position of the ultracold gas in the presence of a trap. Black arrows indicate the direction of the collective oscillations. (a) Breathing mode. (b) Quadrupole mode. (c) Scissor mode.

since the equation of motion to determine the oscillation frequency for both are governed by hydrodynamics.

The damping rate measurement can provide strong evidence to distinguish a collisional Fermi liquid and a superfluid, besides the direct observation of the vortex lattices as a concrete evidence for the superfluidity [24]. We take Duke experiment [22] as an example. Duke group measured both the collective mode frequency and the damping rate of the radial breathing mode in the unitary limit as a function of temperature. They found that the collective mode frequency varies very smoothly and slightly with the temperature, and agrees with a hydrodynamic theory very well. The hydrodynamic behavior of the collective mode frequency means the system is either a collisional Fermi liquid or a superfluid.

For a collisional Fermi liquid, at low temperature the collision rate has the temperature dependence $1/\tau \propto T^2$. Here τ is the life time of the Fermi quasiparticles, and it is the inverse of the collision rate. Therefore, as the temperature decreases, the collision rate also decreases, which should increase the damping rate of a collisional Fermi liquid. The reason is that the first sound can propagate in a collisional Fermi liquid due to the very frequent collisions between Fermi quasiparticles, which drive the system to local equilibrium much faster than the sound frequency. It is also the reason that the classical hydrodynamics can

be applied in this case. If we decrease the collision rate, the local equilibrium will be harder to maintain, which means the first sound will be more difficult to propagate in the system, i.e., a stronger damping occurs. This point can also be seen from a Boltzmann equation analysis [56], where it is shown that for a collisionless Fermi liquid the damping rate is proportional to $1/\tau$, while for a collisional Fermi liquid the damping rate is proportional to τ.

In contrast, the Duke group found that as temperature increases from $\sim 0.05T_F$ to $\sim 0.25T_F$, the damping rate keeps increasing linearly, and afterward it increases nonlinearly. This result indicates that the system is not a collisional Fermi liquid either. Assuming the system is in a superfluid phase, the decreasing damping with decreasing temperature is reasonable, since from the two-fluid model, the normal component portion of the system will decrease when the temperature decreases. The superfluid component is not dissipative, and the contribution to the damping is from the normal component. With smaller normal component portion at lower temperature, the damping should become weaker. This experiment provides strong evidence of the existence of superfluidity at unitarity of the BCS-BEC crossover fermionic gas.

4.0 DAMPING OF ULTRACOLD FERMI GASES

Recently, several experiments on ultracold fermions in the BCS-BEC crossover have shown that puzzling damping phenomena of collective excitations occur in superfluid regime where the system is at a finite temperature and on the BCS side of the crossover [21, 25, 4]. Especially, in Ref. [4], on the BCS side of the crossover, two puzzling damping peaks of scissor mode were found with varying temperature. The first one is sharp and in the superfluid regime, while the other is broad and in the normal Fermi liquid regime. In this chapter, we will present the effective field theory study on these damping phenomena [34], focusing on the experiment in Ref. [4]. Our effective theory is constructed based on a single-channel model, which is known to be adequate for a broad Feshbach resonance. Furthermore, we focus on the BCS side of the crossover, where puzzling damping phenomena have been observed and received much attention [21, 4, 25]. In this regime, the BEC molecular effect is negligible, and hence the single-channel calculation which we adopt is simple and valid. Our theory shows that the dominant damping process is due to interaction between superfluid phonons and thermally excited fermionic quasiparticles at finite temperature, in contrast to the previously proposed pair-breaking mechanism [57, 4]. Such a process is similar to the well-known Landau damping, which was previously discussed in a semiclassical approach [58, 59]. We also calculate the damping rate of collective excitations for the physical systems and find a good comparison with the experimental findings [4]. Throughout this chapter, the Planck constant $\hbar$ and Boltzmann constant k_B are set unity ($\hbar \equiv k_B \equiv 1$ in units).

4.1 MEAN FIELD SOLUTION OF EFFECTIVE FIELD THEORY

We consider a homogeneous unpolarized ultracold fermionic system with two species (spin $\uparrow$ and $\downarrow$) of equal mass, and apply the path integral field theory to our system [60]. The partition function of the system in the grand canonical ensemble can be described in the path integral formalism

$$Z = \int D(\psi_\sigma^*, \psi_\sigma) \exp(-S_\psi), \tag{4.1}$$

where $S_\psi = \int dx \mathcal{L}_\psi(x)$ is the action. Here ψ_σ is the fermionic field for spin $\sigma = \uparrow, \downarrow$, and x is a four vector $x = (\mathbf{x}, \tau)$, where $\mathbf{x}$ is the spatial coordinate and τ is imaginary time in the range $0 < \tau < \beta$. We have $\beta = 1/T$ and T is the temperature. The integration $\int D(\psi_\sigma^*, \psi_\sigma)$ in path integral formalism is introduced in Ref. [60]. The following Lagrangian is used to describe the system:

$$\mathcal{L}_\psi = \psi_\sigma^* \left(\partial_\tau - \frac{\nabla^2}{2m_a} - \mu \right) \psi_\sigma + g \psi_\uparrow^* \psi_\downarrow^* \psi_\downarrow \psi_\uparrow, \tag{4.2}$$

where m_a is the mass of the fermion, g is the interaction (negative on the BCS side), and μ is the chemical potential. The summation over σ is implicit.

We use a Hubbard-Stratonovich transformation [60] by introducing an auxiliary complex bosonic field $\Delta(x)$ to eliminate the quartic term in Eq. (4.2) and get

$$Z = \int D(\psi_\sigma^*, \psi_\sigma) D(\Delta^*, \Delta) \exp(-S_{\psi,\Delta}), \tag{4.3}$$

where the lagrangian is now

$$\mathcal{L}_{\psi,\Delta} = \psi_\sigma^* \left(\partial_\tau - \frac{\nabla^2}{2m_a} - \mu \right) \psi_\sigma + (\psi_\uparrow^* \psi_\downarrow^* \Delta + c.c) - \frac{|\Delta|^2}{g}. \tag{4.4}$$

In this transformation, the auxiliary field $\Delta(x)$ acquires exactly the same expectation value as the pair field at the saddle point:

$$\langle \Delta \rangle = \langle \psi_\downarrow \psi_\uparrow \rangle.$$

The fermionic field is now in quadratic form and can be integrated out to get an effective action for the field Δ

$$Z = \int D(\Delta^*, \Delta) \exp(-S_\Delta), \tag{4.5}$$

where

$$S_\Delta = -\int d^4x \left(\frac{|\Delta|^2}{g} + \mathrm{tr}\ln G^{-1} \right) \tag{4.6}$$

and

$$G^{-1} = \begin{pmatrix} \partial_\tau - \frac{\nabla^2}{2m_a} - \mu & \Delta \\ \Delta^* & \partial_\tau + \frac{\nabla^2}{2m_a} + \mu \end{pmatrix}. \tag{4.7}$$

In the mean field approximation, we seek for a spatially uniform saddle point solution Δ_0 of S_Δ, together with the requirement of fixing the number density n. These two conditions determine the mean field equations in the crossover

$$\begin{aligned} \frac{\delta S_\Delta}{\delta \Delta} &= 0, \\ \frac{\partial \ln Z}{\partial \mu} &= n. \end{aligned} \tag{4.8}$$

In momentum space we get

$$\begin{aligned} \frac{1}{g} + \sum_{\mathbf{k}} \frac{1}{2E_k} \tanh\left(\frac{\beta E_k}{2}\right) &= 0, \\ \sum_{\mathbf{k}} \left[1 - \frac{\xi_k}{E_k} \tanh\left(\frac{\beta E_k}{2}\right) \right] &= n, \end{aligned} \tag{4.9}$$

where $E_k = \sqrt{\xi_k^2 + \Delta^2}$ and $\xi_k = \mathbf{k}^2/2m_a - \mu$.

We use the regularization procedure to express the coupling g in terms of the scattering length a as mentioned in Appendix A:

$$\frac{m_a}{4\pi a} = \frac{1}{g} + \sum_{\mathbf{k}} \frac{1}{2\epsilon_k}, \tag{4.10}$$

where $\epsilon_k = \mathbf{k}^2/2m_a$ and a is the effective scattering length. Eq. (4.9) can be expressed in terms of a as

$$\begin{aligned} \frac{m_a}{4\pi a} &= \sum_{\mathbf{k}} \left[\frac{1}{2\epsilon_k} - \frac{1}{2E_k} \tanh\left(\frac{\beta E_k}{2}\right) \right], \\ n &= \sum_{\mathbf{k}} \left[1 - \frac{\xi_k}{E_k} \tanh\left(\frac{\beta E_k}{2}\right) \right]. \end{aligned} \tag{4.11}$$

Eq. (4.11) includes two equations with Δ and μ as two variables. By using the secant method to solve Eq. (4.11), we can get Δ and μ as function of $1/k_F a$ and T/T_F in mean field

level, where k_F and T_F are the Fermi momentum and temperature of the non-interacting Fermi gas in free space with the same number density n. The values of Δ and μ from this mean field calculation at $T = 0$ are shown in Fig. 6 in Chapter 3.

In the following sections, we will assume the system is ordered, i.e., the gap Δ is non-zero, and will use the mean field results, such as the gap order parameter, as input to calculate the physical quantities of excitations.

4.2 QUANTUM FLUCTUATIONS

To consider the quantum fluctuations, we no longer treat the order parameter Δ as a homogeneous constant in Eq. (4.4), but write it as

$$\Delta(x) = \Delta_0 \left[1 + \lambda(x)\right] e^{i2\varphi(x)}. \tag{4.12}$$

Here λ is the amplitude fluctuation and φ is the phase fluctuation around the saddle point solution Δ_0 from Eq. (4.11), and both of them are real. The energy spectrum of φ is gapless, i.e., in the long wavelength limit the excitation energy vanishes, which indicates the sound (phonon) excitation of the system. The spectrum of φ is also related to the oscillation frequency of the collective mode, where an experimentally excited collective oscillation with frequency ω yields the same phonon frequency ω of the φ field. Then one can apply a local U(1) gauge transformation to a new gauge where the order parameter is real everywhere in space

$$\Delta = \tilde{\Delta} e^{i2\varphi(x)}, \psi_\sigma(x) = \tilde{\psi}_\sigma(x) e^{i\varphi(x)}, \tag{4.13}$$

where $\tilde{\Delta} = \Delta_0(1 + \lambda)$ is real. We have $1 + \lambda > 0$ and $\varphi \in [0, 2\pi)$ as the constrain. The integration over λ can be extended to the range $1 + \lambda < 0$, which only yields an overall constant phase π add to φ. Since φ only appears in gradient form, this overall phase does not change the effective action for φ. In addition, we treat the Jacobian of the transformation as a constant using the same approximation in Ref. [51, 61], which is valid at low temperature [61].

With the above considerations, in the new gauge, the Lagrangian density Eq. (4.4) becomes

$$\begin{aligned}\mathcal{L}_{\tilde{\psi},\varphi,\lambda} &= \tilde{\psi}^*_\sigma(\partial_\tau - \frac{\nabla^2}{2m_a} - \mu)\tilde{\psi}_\sigma + (\Delta_0\tilde{\psi}^*_\uparrow\tilde{\psi}^*_\downarrow + c.c.) + \tilde{\psi}^*_\sigma\tilde{\psi}_\sigma[i\partial_\tau\varphi + \frac{(\nabla\varphi)^2}{2m_a}] + \nabla\varphi\cdot\hat{\mathbf{J}}_\sigma \\ &+(\Delta_0\lambda\tilde{\psi}^*_\uparrow\tilde{\psi}^*_\downarrow + c.c.) - \frac{\Delta_0^2\lambda^2}{g}, \end{aligned} \tag{4.14}$$

where $\hat{\mathbf{J}}_\sigma = \hat{\mathbf{J}}_\sigma(x) = -\frac{i}{2m_a}[\tilde{\psi}^*_\sigma(\nabla\tilde{\psi}_\sigma) - (\nabla\tilde{\psi}^*_\sigma)\tilde{\psi}_\sigma]$ is the fermion current field.

We now integrate out the fermionic field. The fermionic field is gapped, which means even in the long wavelength limit, the fermionic excitations (the Bogoliubov quasiparticles) cost finite energy. In momentum space, for the fermionic field $\tilde{\psi}$, we use $k = (\mathbf{k}, i\omega_m)$, where $\omega_m = (2m+1)\pi/\beta$ is the fermionic Matsubara frequency and m is an integer. For the bosonic field λ and φ, we use $q = (\mathbf{q}, i\omega_n)$, and $\omega_n = 2n\pi/\beta$, where n is an integer.

Introducing two-component spinor in momentum space $\Psi^*_k = (\tilde{\psi}^*_{k\uparrow}, \tilde{\psi}_{-k\downarrow})$, we can rewrite the action in momentum space as $S = \sum_{k_1,k_2}\Psi^*_{k_1}G^{-1}(k_1,k_2)\Psi_{k_2}$, where $G^{-1} = G_0^{-1} + \chi_1 + \chi_2$ is 2×2 matrix. Here G_0, χ_1, and χ_2 are given by

$$\begin{aligned} G_0(k_1,k_2) &= \frac{\delta_{k_1,k_2}}{\omega^2_{m_1} + E^2_{k_1}}\begin{pmatrix} i\omega_{m_1} + \xi_{k_1} & \Delta_0 \\ \Delta_0 & i\omega_{m_1} - \xi_{k_1}\end{pmatrix} \\ \chi_2(k_1,k_2) &= -\sum_q \frac{\mathbf{q}\cdot(\mathbf{k_1}-\mathbf{k_2}-\mathbf{q})}{2m_a\beta V}\varphi_q\varphi_{k_1-k_2-q}\begin{pmatrix} 1 & 0 \\ 0 & -1\end{pmatrix} \\ \chi_1(k_1,k_2) &= \begin{pmatrix} \chi_1^{11}(k_1,k_2) & \chi_1^{12}(k_1,k_2) \\ \chi_1^{21}(k_1,k_2) & \chi_1^{22}(k_1,k_2)\end{pmatrix} \end{aligned} \tag{4.15}$$

with

$$\begin{aligned} \chi_1^{11}(k_1,k_2) &= \left[\frac{\omega_{m_1}-\omega_{m_2}}{\sqrt{\beta V}} + \frac{i(\mathbf{k_1^2}-\mathbf{k_2^2})}{2m\sqrt{\beta V}}\right]\varphi_{k_1-k_2} \\ \chi_1^{22}(k_1,k_2) &= \left[-\frac{\omega_{m_1}-\omega_{m_2}}{\sqrt{\beta V}} + \frac{i(\mathbf{k_1^2}-\mathbf{k_2^2})}{2m\sqrt{\beta V}}\right]\varphi_{k_1-k_2} \\ \chi_1^{12}(k_1,k_2) &= \chi_1^{21}(k_1,k_2) = \frac{\Delta_0}{\sqrt{\beta V}}\lambda_{k_1-k_2}. \end{aligned} \tag{4.16}$$

We adopt Gaussian approximation for the amplitude field λ and low energy expansion φ for the superfluid phase field, which means we keep the λ and φ fields to quadratic order

$$\int D(\Psi^*,\Psi)e^{-S_{\Psi,\lambda,\varphi}} \approx e^{\mathrm{tr}[G_0\chi_2-\frac{1}{2}G_0\chi_1G_0\chi_1]} = e^{-S'}. \tag{4.17}$$

The effective action reads

$$S' = S_\varphi + S_\lambda + S_{\varphi,\lambda}, \tag{4.18}$$

where

$$\begin{aligned}
S_\varphi &= \sum_q \varphi_q\varphi_{-q}[f_1(q)\omega_n^2 + [f_4(q)+\frac{n}{2m_a}]\mathbf{q}^2], \\
S_\lambda &= \sum_q \lambda_q\lambda_{-q}f_3(q), \\
S_{\varphi,\lambda} &= \sum_q [f_2(q)\lambda_q\varphi_{-q}(-\omega_n - \frac{i}{m_a}\mathbf{q}\cdot\mathbf{k}) - f_2(q)\lambda_{-q}\varphi_q(-\omega_n+\frac{i}{m_a}\mathbf{q}\cdot\mathbf{k})],
\end{aligned} \tag{4.19}$$

and

$$\begin{aligned}
f_1 &= \frac{1}{\beta V}\sum_k \frac{\omega_m\omega_{m+n}-\xi_k\xi_{k+q}+\Delta_0^2}{(\omega_m^2+E_k^2)(\omega_{m+n}^2+E_{k+q}^2)}, \\
f_2 &= \frac{\Delta_0^2}{\beta V}\sum_k \frac{i\omega_m + i\omega_{m+n}+\xi_k+\xi_{k+q}}{(\omega_m^2+E_k^2)(\omega_{m+n}^2+E_{k+q}^2)}, \\
f_3 &= -\frac{\Delta_0^2}{g} - \frac{\Delta_0^2}{\beta V}\sum_k \frac{\omega_m\omega_{m+n}+\xi_k\xi_{k+q}-\Delta_0^2}{(\omega_m^2+E_k^2)(\omega_{m+n}^2+E_{k+q}^2)}, \\
f_4 &= \frac{1}{\beta V}\sum_k \frac{k^2\cos^2\theta}{m_a^2}\frac{-\omega_m\omega_{m+n}+\xi_k\xi_{k+q}+\Delta_0^2}{(\omega_m^2+E_k^2)(\omega_{m+n}^2+E_{k+q}^2)}.
\end{aligned} \tag{4.20}$$

We can also start from Eq. (4.6) and get the same result. Here in Eq. (4.14), we follow the procedure in Ref. [60], where the coupling between the order parameter (amplitude λ and phase φ) and the fermions is explicitly shown.

The next step is to integrate out the amplitude fluctuation field λ and keep only the phase field φ. Define

$$\begin{aligned}
C_1(q) &= f_1 + f_2^2/f_3, \\
C_2(q) &= f_4 + \frac{n}{2m_a},
\end{aligned} \tag{4.21}$$

and the effective action of phase field φ is obtained as

$$S_\varphi = \sum_q \varphi_q\varphi_{-q}[C_1(q)\omega_n^2 + C_2(q)\mathbf{q}^2]. \tag{4.22}$$

4.3 SOUND VELOCITY

To test our theory before calculating the damping rate, we first evaluate superfluid density and sound velocity. Superfluid density is the non-dissipative density component of the system. For a BEC superfluid, the superfluid density is not the condensate density. At $T = 0$, the superfluid density is the total density, while the condensate density is only a fraction of the total density. Since superfluid is irrotational, a rotating-bucket experiment can be used to determine the superfluid density [52]. On the theoretical side, the superfluid density can be directly calculated from the known expressions for both BEC and BCS cases [52].

In our problem of BCS-BEC crossover, we can apply a Galilean boost on the order parameter in Eq. (4.13), and get the superfluid density from the shift of free energy in the superfluid hydrodynamic model with normal and superfluid components [62, 63, 64]. The total normal density includes bosonic fluctuation part and non-condensed fermionic Bogoliubov quasiparticle part. From the calculations of Ref. [62, 63, 64], the main contribution to the normal density on the BEC side is the bosonic excitation part, while on the BCS side, the main contribution is from the non-condensed Bogoliubov fermionic quasiparticle part. Since our main focus is on the BCS side, we can neglect the contribution to the normal density from bosonic excitations.

To the zeroth order of q, or in the long wavelength limit $q \to 0$, all coefficients f_1, f_2, f_3, and f_4 are real, in terms of which superfluid density and sound velocity can be expressed. Since the imaginary part is zero, there is no damping for the collective modes, to the zeroth order. We have $C_1' \equiv \lim_{q\to 0} C_1$ related to the density of states, and $C_2' \equiv \lim_{q\to 0} C_2 = n_s/2m_a$ is related to superfluid density n_s [60]. In $q \to 0$ limit, we neglect the bosonic fluctuation contribution to the normal density, which is the $q \neq 0$ fluctuation contribution from the Δ field [64].

Take the limit of $q \to 0$ in the coefficients Eq. (4.20), and define $f_1' \equiv \lim_{q\to 0} f_1$ and so

on. After carrying out the Matsubara summation for $i\omega_m$, we get

$$\begin{aligned} f_1' &= \frac{1}{V}\sum_{\mathbf{k}}[\beta n_k(1-n_k)\frac{\xi_k^2}{E_k^2}+\frac{\Delta_0^2}{2E_k^3}(1-2n_k)]\,, \\ f_2' &= \frac{\Delta_0^2}{V}\sum_{\mathbf{k}}[\beta n_k(n_k-1)\frac{\xi_k}{E_k^2}+(1-2n_k)\frac{\xi_k}{2E_k^3}]\,, \\ f_3' &= \frac{\Delta_0^4}{V}\sum_{\mathbf{k}}[\beta n_k(n_k-1)\frac{1}{E_k^2}+\frac{1}{2E_K^3}\tan\frac{\beta E_k}{2}]\,, \\ f_4' &= \sum_{\mathbf{k}}\frac{\beta}{V}\frac{k^2\cos^2\theta}{m_a^2}n_k(n_k-1)\,, \end{aligned} \tag{4.23}$$

where

$$n_k = \frac{1}{e^{\beta E_k}+1}$$

is the quasiparticle Fermi-Dirac distribution. Eq. (4.22) becomes

$$S_\varphi = \sum_q \varphi_q\varphi_{-q}[C_1'\omega_n^2 + C_2'\mathbf{q}^2] \tag{4.24}$$

with

$$\begin{aligned} C_1' &= f_1' + f_2'^2/f_3'\,, \\ C_2' &= f_4' + \frac{n}{2m_a}\,. \end{aligned} \tag{4.25}$$

To switch from the Matsubara frequency to real frequency (or from imaginary time to real time), we apply a Wick rotation $i\omega_n = \omega_q + i0^+$ [60], and then the zero of the action Eq. (4.24) gives the spectrum $\omega_q = v_s|\mathbf{q}|$ of the φ field. This spectrum is the superfluid phonon excitation, where v_s tells the sound velocity. Thus, we get the following physical quantities,

$$\begin{aligned} \frac{n_s}{2m_a} &= f_4' + \frac{n}{2m_a}\,, \\ v_s^2 &= \frac{f_4' + n/2m_a}{f_1' + f_2'^2/f_3'}\,. \end{aligned} \tag{4.26}$$

At zero temperature, Eq. (4.23) reduces to

$$\begin{aligned} f'_{1,T=0} &= \frac{\Delta_0^2}{V}\sum_{\mathbf{k}}\frac{1}{2E_k^3}, \\ f'_{2,T=0} &= \frac{\Delta_0^2}{V}\sum_{\mathbf{k}}\frac{\xi_k}{2E_k^3}, \\ f'_{3,T=0} &= \frac{\Delta_0^4}{V}\sum_{\mathbf{k}}\frac{1}{2E_k^3}, \\ f'_{4,T=0} &= 0. \end{aligned} \tag{4.27}$$

Perform the summation for f''s over $\mathbf{k}$ as integration in the thermodynamic limit, and define the following integral quantities as mentioned in Chapter 3 that

$$J_2 = \int_0^\infty dk \frac{k^2}{E_k^3}, \;\; J_4 = \int_0^\infty dk \frac{k^4}{E_k^3}, \;\; J_\xi = \int_0^\infty dk \frac{k^2\xi_k}{E_k^3}. \tag{4.28}$$

After some calculations, the sound velocity Eq. (4.26) at $T = 0$ is

$$v_{s,T=0}^2 = \frac{1}{3m_a^2}\frac{J_2 J_4 \Delta_0^2}{J_2^2\Delta_0^2 + J_\xi^2}, \tag{4.29}$$

which reproduces the result Eq. (3.12) in Chapter 3, albeit that was derived in a different method. The success in deriving the sound velocity verifies the validity of our effective field theory approach.

Fig. 8 shows the numerical plot of superfluid density and superfluid sound velocity with varying temperature and scattering length in the BCS regime, as a visualization for the real part of the effective action from our effective field theory approach.

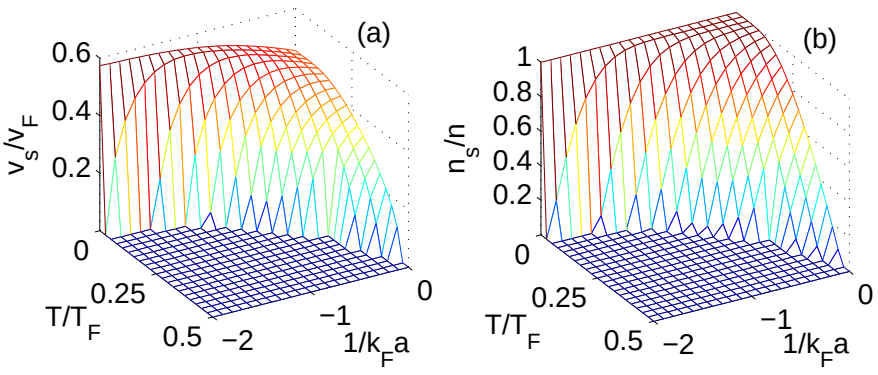

Figure 8: (a) Superfluid sound velocity compared with Fermi velocity v_s/v_F in superfluid regime. (b) Superfluid density compared with the total density n_s/n. The superfluid sound velocity from our effective field theory Eq. (4.29) reproduces the result Eq. (3.12) in Chapter 3 from hydrodynamic approach, which verifies the validity of our theory. We also see that the superfluid density portion of total density decreases with increasing temperature, which is expected.

4.4 DAMPING OF COLLECTIVE MODES

4.4.1 Formalism of the Damping Rate

We start from the effective action, Eq. (4.22), for the superfluid phase field. Keeping q small but finite when evaluating the coefficients C_1 and C_2 in Eq. (4.21), imaginary terms appear in Eq. (4.20), which corresponds to the damping of the collective modes. To get exact dispersion relation including damping for the superfluid phonons, one needs to solve for poles of the effective action Eq. (4.22) of φ. However, in the regime where the damping is small, we can simplify the calculation.

The dispersion relation is determined by setting the quadratic field term Eq. (4.22) to be zero. To evaluate the damping rate, we can apply a Wick rotation to change from the Matsubara frequency to real frequency part and imaginary damping part as $i\omega_n = \omega_0 - i\gamma$,

and get

$$-C_1(\tilde{q})(\omega_0 - i\gamma)^2 + C_2(\tilde{q})\mathbf{q}^2 = 0, \tag{4.30}$$

$$\tilde{q} \equiv (\mathbf{q},\ i\omega_n \to \omega_0 + i0^+), \tag{4.31}$$

where ω_0 is the oscillation frequency, or the real part of the phonon mode, and γ is the damping rate. Although in principle, we should also keep γ when applying the Wick rotation to the ω_n's in coefficients f_1, f_2, f_3, and f_4, for small damping, it is sufficient to just apply $i\omega_n = \omega_0 + i0^+$ for the coefficients to get the lowest order results. This approximation is similar to that adopted in the calculation for self-energy, for example, Ref. [65].

For the numerators in Eq. (4.20), we can still set $q = 0$ (zeroth order of q). The reason for this is that the numerators are all real, and hence the small q expansion gives only higher order corrections to the zeroth order contribution. If we want only the leading order in the long wavelength expansion of the damping rate, the higher order corrections in the numerators can be ignored, as we have checked.

Also, we can still use the results Eq. (4.23) obtained from last section for the real parts of C_1, C_2, f_1, f_2, f_3, and f_4 (zeroth order of q), because we are not interested in the higher order corrections (first and higher order of q) to the real parts of coefficients, which just give higher order correction to the damping rate.

Adopting the above approximation, we can write $C_1 = C_1' + iC_1'', C_2 = C_2' + iC_2'', f_1 = f_1' + if_1''$ and so on, to find the poles of the effective action

$$(C_1' + iC_1'')(\omega_0 - i\gamma)^2 - (C_2' + iC_2'')\mathbf{q}^2 = 0\,. \tag{4.32}$$

Solving this equation gives the damping rate

$$\frac{\gamma}{\omega_0} = \frac{1}{2}\left(\frac{C_1''}{C_1'} - \frac{C_2''}{C_2'}\right)\,. \tag{4.33}$$

From Eq. (4.21), assuming that all the imaginary parts are small, i.e., only keeping up to the first order of the imaginary part for f's, we have

$$\begin{aligned} C_1'' &= f_1'' + 2\frac{f_2'}{f_3'}f_2'' - \left(\frac{f_2'}{f_3'}\right)^2 f_3''\,, \\ C_2'' &= f_4''\,. \end{aligned} \tag{4.34}$$

After some calculation, we find that the imaginary parts of the coefficients f'''s contain two different contributions, which we call channel a and b. In channel a we have

$$\begin{aligned}
f''_{1,a} &= \frac{\pi}{V}\sum_{\mathbf{k}}(1-\frac{\Delta_0^2}{E_k^2})\delta[\omega_0-(E_{k+q}-E_k)](n_k-n_{k+q})\,,\\
f''_{2,a} &= -\frac{\pi\Delta_0^2}{V}\sum_{\mathbf{k}}\frac{\xi_k}{E_k^2}\delta[\omega_0-(E_{k+q}-E_k)](n_k-n_{k+q})\,,\\
f''_{3,a} &= -\frac{\pi\Delta_0^4}{V}\sum_{\mathbf{k}}\frac{1}{E_k^2}\delta[\omega_0-(E_{k+q}-E_k)](n_k-n_{k+q})\,,\\
f''_{4,a} &= -\frac{\pi}{V}\sum_{\mathbf{k}}\frac{\mathbf{k}^2\cos^2\theta}{m_a^2}\delta[\omega_0-(E_{k+q}-E_k)](n_k-n_{k+q})\,,
\end{aligned} \tag{4.35}$$

and in channel b

$$\begin{aligned}
f''_{1,b} &= \frac{\pi}{V}\sum_{\mathbf{k}}\frac{\Delta_0^2}{2E_k^2}\delta(\omega_0-E_k-E_{k+q})(1-n_k-n_{k+q})\,,\\
f''_{2,b} &= \frac{\pi\Delta_0^2}{V}\sum_{\mathbf{k}}\frac{\xi_k}{2E_k^2}\delta(\omega_0-E_k-E_{k+q})(1-n_k-n_{k+q})\,,\\
f''_{3,b} &= -\frac{\pi\Delta_0^2}{V}\sum_{\mathbf{k}}(\frac{1}{2}-\frac{\Delta_0^2}{2E_k^2})\delta(\omega_0-E_k-E_{k+q})\,,\\
&\quad\times(1-n_k-n_{k+q})\,,\\
f''_{4,b} &= 0\,.
\end{aligned} \tag{4.36}$$

The physical meaning of channel a and b, as defined in the above expressions, is illustrated in Fig. 9. Channel a (Fig. 9(a)) is similar to the Landau damping in Fermi liquid. In channel a, a fermionic quasiparticle absorbs or emits a superfluid phonon and becomes another quasiparticle state at a different momentum within the same energy branch. In channel b (Fig. 9(b)), a superfluid phonon excites a quasiparticle from the lower branch to the upper branch, creating a particle-hole pair excitation in the quasiparticle eigenstate basis, which corresponds to a Cooper pair breaking process in terms of original fermions. Both channels cause imaginary part of superfluid phonon dispersion (collective excitations of the superfluid state), which corresponds to the damping of phonon excitation, or collective oscillation.

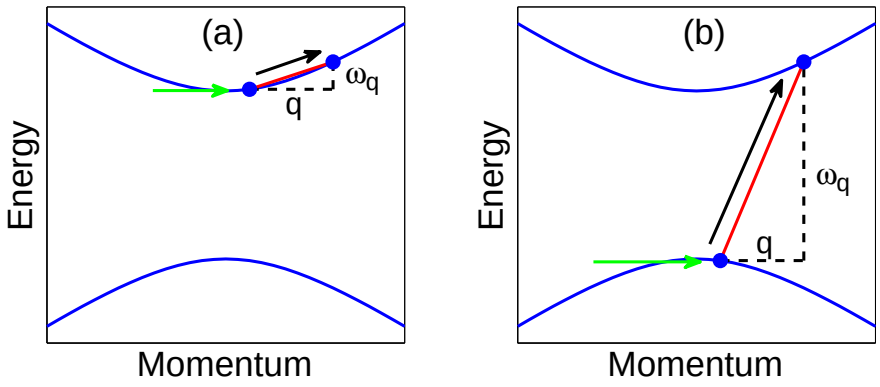

Figure 9: Two separate damping channels. The blue curves are the fermionic quasiparticle spectrum. At $T = 0$, the lower branch is fully occupied and the higher branch is empty. The green arrow is the incident phonon. The black arrow indicates the excitation of a fermionic quasiparticle. The red straight line is the linear spectrum of the phonon, where the slope is the sound velocity. The two black dashed lines are the changes of momentum and energy of fermionic quasiparticle, as indicated. (a) A phonon scatters an existing (at finite temperature) fermionic quasiparticle to a different state in the same energy branch. Such a process is similar as Landau damping in Fermi liquid. This process can also happen in the lower branch at finite temperature, which is not shown here. (b) A phonon creates a quasi-particle-hole pair across the lower and upper bands, equivalent to Cooper pair breaking in the representation of original fermions.

Before applying our result to real experimental systems, let us discuss the properties of the damping in the $\omega_0 \to 0$ limit (with $\omega_0/|\mathbf{q}| = v_s$ fixed) at low temperature, where channel b vanishes. To satisfy the δ function in Eq. (4.35), we need to have

$$|\cos\theta| = \left|\frac{E_k m_a v_s}{\xi_k k}\right| \leq 1, \tag{4.37}$$

which is difficult to solve analytically.

We can still get some analytical properties if we combine the numerical and analytical analysis. At $1/k_F a = -0.45$ and $T/T_F < 0.1$, numerical analysis shows that $k < k_\mu$ does not

contribute to the integral, with k_μ the momentum corresponding to the chemical potential μ. For $k > k_\mu$, we can substitute $k = k_\mu$ in Eq. (4.37), except for ξ_k, to get the range of ξ_k. We then apply a one-step iteration to get a more precise range for ξ_k. To satisfy Eq. (4.37), we need to have

$$\xi_k > \frac{\sqrt{\xi_0^2 + \Delta^2} m_a v_s}{\sqrt{2m_a(\xi_0 + \mu)}} \equiv \xi_1, \ \xi_0 = \frac{\Delta m_a v_s}{k_\mu}. \tag{4.38}$$

The next step is to write

$$n_k - n_{k+q} \approx \frac{\partial n_k}{\partial E_k} \cdot (E_k - E_{k+q}) = \beta\omega_0 n_k(1 - n_k) \approx \beta\omega_0 e^{-\beta E_k}. \tag{4.39}$$

The first approximation comes from $\omega_0 \ll T$ and the second approximation comes from $T \ll \Delta$. Also, numerical analysis shows that the contribution from C_1'' is much smaller than that from C_2'' in the above regime. In addition, at low temperature, $C_2' \approx n/2m_a$ since the normal density is negligible. Taking all the above into account, we get

$$\frac{\gamma}{\omega_0} \approx \frac{3\pi}{4} \frac{v_s^3}{v_f^3} \frac{1}{T} \int_{E_k > \sqrt{\xi_1^2 + \Delta^2}} dE_k \frac{E_k^4}{\xi_k^4} e^{-\beta E_k}. \tag{4.40}$$

The integral in Eq. (4.40) needs to be evaluated numerically in general cases. At extremely low temperature, where $e^{-\beta E_k}$ changes much faster than E_k^4/ξ_k^4 with changing E_k, we can approximately treat E_k^4/ξ_k^4 in Eq. (4.40) as a constant and substitute in $\xi_k = \xi_1$, which gives

$$\frac{\gamma}{\omega_0} \approx \frac{3\pi}{4} \frac{v_s^3}{v_f^3} \frac{(\xi_1^2 + \Delta^2)^2}{\xi_1^4} e^{-\frac{\sqrt{\xi_1^2 + \Delta^2}}{T}}. \tag{4.41}$$

An interesting feature of damping is that in Eq. (4.40) and (4.41), γ/ω_0 is independent of ω_0 when $\omega_0 \ll T$. Therefore, we should observe the damping even in the $\omega_0 \to 0$ limit in finite temperature. A physical understanding of this feature is that the damping from channel a is due to the coupling between superfluid sound (phonons) and thermally excited Fermi quasiparticles, so that

$$\gamma \propto \int dk f(k, \Delta, \mu)(n_k - n_{k+q}) \propto \omega_0 \int dk f(k, \Delta, \mu) \frac{dn_k}{dE_k}, \tag{4.42}$$

where $f(k, \Delta, \mu)$ is some function independent of ω_0. This provides an experimental method to verify our theory, which will be discussed later.

4.4.2 Comparison with Experiments

The above theory can be applied to real physical systems numerically. We will focus on the regime of $\gamma/\omega_0 \ll 1$ on the BCS side of the Feshbach resonance, where our approximations are quantitatively controlled. One should notice that in experiments, the cold gases are trapped in anisotropic harmonic potentials. The parameters used here, i.e., the Fermi energy, chemical potential, etc., correspond to the values at the center of the trap. We apply our method to the experimental configuration in Ref. [4] and calculate the damping rate as function of both temperature and scattering length. The number of particles is $N = 4 \times 10^5$. The trapping frequencies are $\omega_x = 2\pi \times 830$ Hz, $\omega_y = 2\pi \times 415$ Hz and $\omega_z = 2\pi \times 22$ Hz. Thus, $\bar{\omega} = (\omega_x \omega_y \omega_z)^{1/3} = 2\pi \times 196$ Hz. Reading from Ref. [4], the oscillation (phonon) frequency is $\omega_0 \approx 2\pi \times 940$ Hz $\approx 4.8\ \bar{\omega}$. According to $\bar{\omega}/T_F = 1/(3N)^{1/3}$, we get the ratio between the phonon energy and Fermi temperature

$$\frac{\omega_0}{T_F} = 0.045. \tag{4.43}$$

From $\omega_0 = v_s|\mathbf{q}|$ and $E_F = \frac{1}{2} v_F k_F$, we get

$$\frac{|\mathbf{q}|}{k_F} = \frac{1}{2} \frac{v_F}{v_s} \frac{\omega_0}{E_F}.$$

Since in most regime $v_F/(2v_s) \sim O(1)$ as shown in Fig. 8, using Eq. (4.43) we conclude that $|\mathbf{q}|$ is also much smaller than the Fermi momentum k_F. Thus, our model, which requires q to be small, can be applied to this physical system.

Fig. 10 shows the numerical results of damping rate from channel a. It shows that the damping rate increases for higher temperature and smaller scattering amplitude $|a|$. In the superfluid regime, when T is close to T_c, the damping rate γ/ω_0 becomes big. When solving the equations for the damping rate in the preceding section, we assumed a small damping γ compared with the oscillation frequency ω_0, i.e., kept only the leading order in the perturbative expansion of γ/ω_0. In the regime of large γ/ω_0 where a significant correction is expected, our damping formula is no longer reliable. Thus, in Fig. 10 we use a plateau to indicate the regime of $\gamma/\omega_0 > 0.5$. Also, in the normal Fermi Liquid regime $T > T_c$ where our theory no longer applies, we keep the damping plot open with no data points shown, and will discuss this regime later.

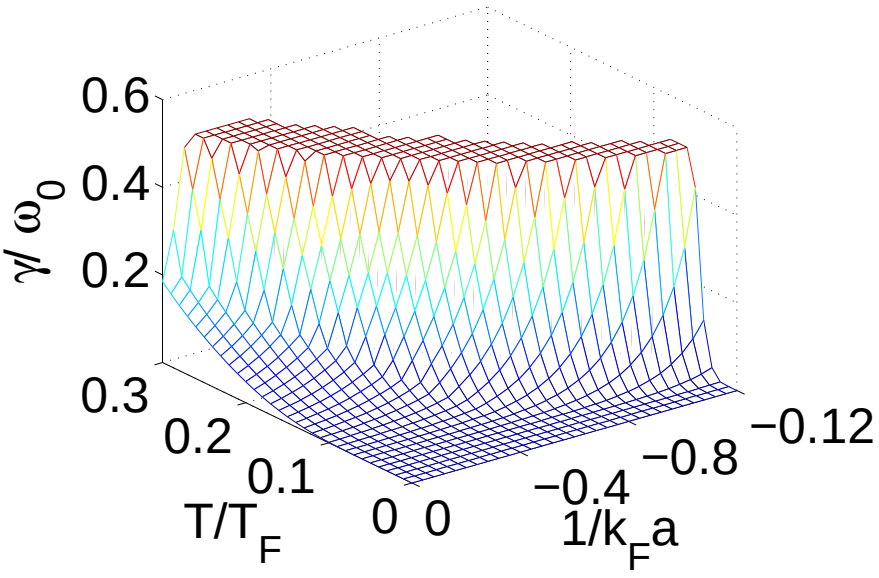

Figure 10: Damping rate of collective excitations in superfluid regime showing dependence on T/T_F and $1/k_F a$. When T is close to T_c, the results from our approximation are no longer reliable since the damping rate γ is already very large compared with ω_0. This regime is indicated by the plateau. Also, when the system is no longer superfluid ($T > T_c$), our effective field theory does not apply, and the damping rate is then not plotted there. The phase transition temperature T_c/T_F is indicated by the boundary of the plateau beyond which there are no data points shown.

We did not include channel b when plotting Fig. 10. The reason is that we found that under the experimental conditions [4], the contribution to damping from channel b is much smaller than from channel a. To investigate the features of channel a and channel b in more detail, let us start from the relationship $\omega_q = v_s|\mathbf{q}|$. We focus on the regime of long wavelength and low temperature such that $k_F \gg |\mathbf{q}|$, and T is not close to T_c. Thus $\Delta(T)$ is of the same order as E_F. In channel a, the first requirement is finite temperature, so that the upper (lower) band is populated by quasiparticles (quasiholes) due to thermalization. This fact is enforced by the factor $(n_k - n_{k+q})$ in Eq. (4.35). The second requirement is energy conservation. The energy change of the fermionic quasiparticle after scattering with

a phonon is as follows,

$$\delta E = E_{k+q} - E_k \approx \frac{\xi_k}{E_k}\frac{\mathbf{k}\cdot\mathbf{q}}{m_a} \leq \frac{\xi_k}{E_k}\frac{|\mathbf{k}||\mathbf{q}|}{m_a}. \tag{4.44}$$

$\omega_q \approx \delta E$ is needed to satisfy energy conservation. Therefore, we have

$$\omega_q = v_s|\mathbf{q}| \leq \frac{\xi_k}{E_k}\frac{|\mathbf{k}||\mathbf{q}|}{m_a}. \tag{4.45}$$

If $|\mathbf{k}|$ is too far away from k_F, both the finite-temperature occupation number and the density of states are greatly suppressed. Equivalently, the most effective scattering of phonons is from quasiparticle states around the upper (lower) band's minimum (maximum). In addition, we have learned in Fig. 8 that v_s does not exceed the order of v_F. As long as $|\mathbf{k}|$ is of the order k_F or smaller, in principle, phonons of both large and small v_s may excite fermionic quasiparticles in channel a. However, the condition Eq. (4.45) suggests that small v_s is much more favored in channel a.

In channel b, the pair breaking process is allowed by the condition of occupation number at $T = 0$ ($n_k = n_{k+q} = 0$ in Eq. (4.36)). However, in this case,

$$\delta E = E_{k+q} + E_k \geq 2\Delta\,, \tag{4.46}$$

where the minimal value of δE takes place for k around k_F. Again, by energy conservation, $\omega_q \approx \delta E$ is required. Subsequently, we find the minimal condition required of the sound velocity v_s,

$$v_s \geq \frac{\Delta}{E_k}\frac{k_F}{|\mathbf{q}|}v_F. \tag{4.47}$$

As long as Δ is of the same order of E_F, and given that $k_F/|\mathbf{q}|$ is quite large, the condition Eq. (4.47) in turns requires that the sound velocity v_s be much larger than the Fermi velocity v_F. In the superfluid phonon case, the condition $k_F \gg |\mathbf{q}|$ is satisfied, and when the temperature is still far away from T_c, channel b is prohibited, since $v_s < v_F$ as shown in Fig. 8. Another way to understand that the damping channel b is suppressed is to directly use energy conservation. Since $\omega_q \ll 2\Delta$, channel b can not happen.

At finite temperature, channel a becomes possible since some fermionic quasiparticles and quasiholes are thermally created in the upper and lower band, respectively. They can

scatter with superfluid phonons to cause decay. However, channel b is still greatly suppressed as long as $w_q < 2\Delta$.

In the experiment, since $\omega_0/E_F \approx 0.04$, channel b can happen only when when $\Delta(T)/E_F \approx 0.02$. From mean field analysis, near $1/k_F a \approx -0.5$, to satisfy $\Delta(T)/E_F \approx 0.02$, we need to have $T/T_c \approx 99.7\%$, which is very near the phase transition. However, according to Ref. [4], the damping happens at $T \approx 0.6T_c$ near $1/k_F a \approx -0.5$, which is too low to let channel b contribute in our calculation. Even if one uses some theories including quantum fluctuation [63], at $T \approx 0.6T_c$, $\Delta(T)/E_F$ is still much larger than 0.02. Thus the damping peak should not correspond to the pair breaking channel b. As T getting closer to T_c, channel a will be more and more enhanced because of more and more thermally excited fermionic quasiparticles. When $\Delta(T)/E_F \approx 0.02$, channel b also happens, while the damping from channel a is already very large. It is not clear which channel dominates because T near T_c is outside the valid regime of our low energy effective field theory. It remains to be a challenge to formulate a quantum theory beyond the classical Boltzmann equation. Thus, our calculation just considered the contribution from channel a. We also double checked channel b by numerical method and confirmed that the contribution from channel b is zero for most regime, since the δ function in Eq. (4.36) cannot be satisfied in most superfluid regime.

There is another piece of experimental evidence showing that why channel b does not dominate. In experiments varying the magnetic field [21, 25], if the pair breaking mechanism had dominated, one should also have observed very sharp peaks in these experiments. However, the damping rate changes relatively smoothly [21, 25], which means channel a should be the reason for the smoothly increasing damping. Therefore, we expect the damping observed by changing the temperature [4] to be due to channel a too, since increasing the magnetic field at a finite temperature has the same effect as increasing the temperature at fixing magnetic field, both just reducing the gap. Nevertheless, the pair breaking channel b is also possible to contribute near the phase transition, but it does not necessarily dominate in contrary to what has been suggested [57, 4].

We did not consider the fact that in the experiment, the fermionic gases are trapped and inhomogeneous in space. The above consideration is effective for gas at the center of the trap. On the edge of the trapped gas, by local density approximation, the effective density

and Fermi energy is smaller than that of center, which means ω_0/E_F is larger and channel b may contribute at lower temperature (but not very low). However, channel a also happens on the edge since the above analysis still works for lower gas density on the edge, and the effect of channel b is just to increase the damping rate, not giving a sudden peak.

To verify our main conclusion that channel a is the dominating process, we propose an experiment, which is to measure the damping rate γ while varying the oscillation frequency ω_0, and observe how γ/ω_0 changes. This can be done by either increasing the particle number or reducing the trapping potential. If channel b, the pair breaking mechanism, were dominating, one should observe that the damping peak becomes increasingly narrow, and eventually becomes too narrow to be observable, as ω_0 decreases. The reason is that the parameter regime to satisfy the energy conservation $\omega_0 \approx 2\Delta$ diminishes with decreasing ω_0, and eventually vanishes. On the other hand, if channel a, the Landau damping mechanism, dominates, no matter how small ω_0 is, as long as Eq. (4.37) is satisfied, the energy conservation law is always satisfied. Eventually γ/ω_0 will be independent of ω_0 in the limit of vanishing ω_0 as discussed before in Eq. (4.42), and therefore the peak in γ/ω_0 remains unchanged and should always be observable.

The mechanism discussed here is different from the conventional acoustic attenuation process in solid-state superconductors, where channel b overwhelms channel a and $\omega_q \approx 2\Delta$. For the conventional case, v_s is large, so that a relatively large phonon energy ω_q corresponds to a very small momentum $\mathbf{q}$. Channel a is suppressed as v_s is too large to satisfy the energy conservation condition (4.45). At the same time, a channel b pair breaking process (Fig. 9(b)), associated with small momentum but large energy transfer from acoustic phonons to Fermi quasiparticles, may happen. The original fermion pair breaking process is the creation of a pair comprising particle and hole in the upper and lower branches of quasiparticle energy spectrum, respectively. A small $|\mathbf{q}|$ ensures that fermionic quasiparticles are created at the band extrema, which is known to result in a peak of damping rate, $\gamma \propto 1/\sqrt{\omega - 2\Delta}$, due to the singularity of density of states. Therefore, the damping for large v_s in the traditional case is due to the pair breaking process (channel b).

In the regime $T > T_c$, where the system is no longer superfluid and our effective theory breaks down, the classical Boltzmann equation can be used to calculate the oscillation fre-

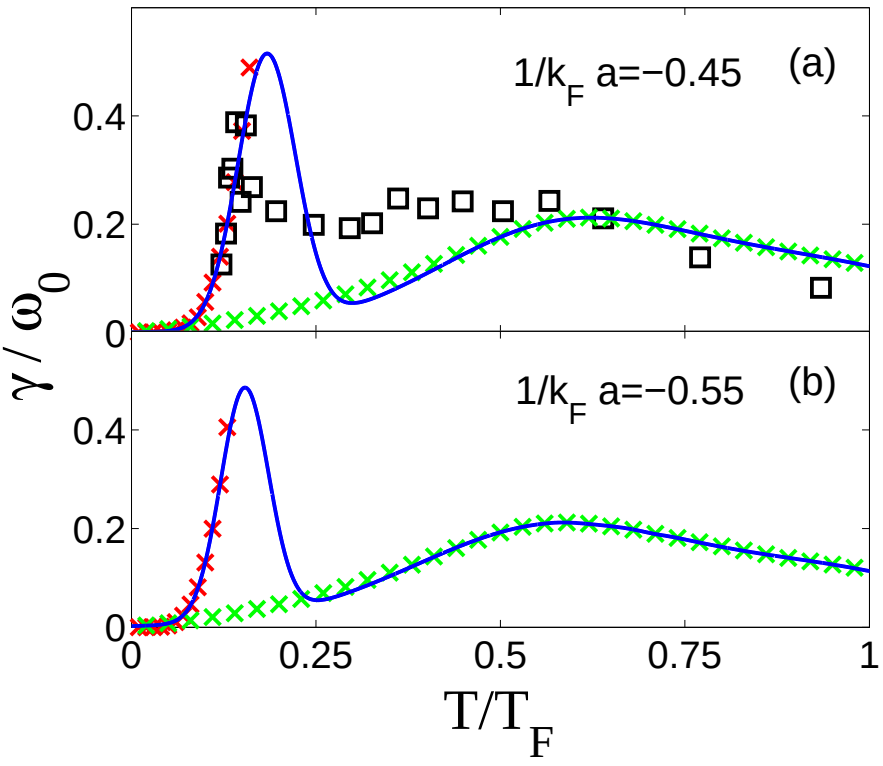

Figure 11: Damping rate of collective excitations by interpolating results from our effective field theory in low temperature and the classical Boltzmann equation in high temperature. Red crosses are the prediction from our calculation in low temperature superfluid regime, and green crosses are calculated from the classical Boltzmann equation approach we adopt from Ref. [2]. The blue solid line is the interpolation. The black squares are the experimental data of damping [3]. (a) $1/k_F a = -0.45$; (b) $1/k_F a = -0.55$. The first peak moves toward higher temperature when the system gets closer to the resonance (i.e., smaller $|1/k_F a|$).

quency and damping rate, as shown in Ref. [2]. As supplement to our main result above, we use the classical Boltzmann equation approach in Ref. [2] to calculate the oscillation frequency and damping rate at high temperatures. As mentioned there, the formulas did not take into account the effect of Pauli blocking, which means that this Boltzmann results are more reliable at high temperatures. The calculation takes into account the trapping potential. At $1/k_F a = -0.45$, if we interpolate our theory in the low temperature super-

fluid regime with the results from Boltzmann equation in the high temperature Fermi liquid regime, two peaks by two different methods appear in Fig. 11, which agrees with the experimental results fairly well (cf. Fig. 2(b) in Ref. [4]). Thus, we conclude that the first sharp peak observed in Ref. [4] is due to the superfluid phonon and fermionic quasiparticle interaction, mostly through channel a in Fig. 9(a). The second broad peak is given by the Boltzmann equation from Ref. [2], which signals the collisional to collisionless transition of Fermi liquid. Our model further shows that the first damping peak moves toward higher temperature when the system gets closer to resonance (i.e., smaller $|1/k_F a|$), as one can see in the change from Fig. 11(b) to Fig. 11(a). This phenomenon was first reported in the experiments of Ref. [4] (cf. Fig. 3 therein). Therefore, our theory provides a consistent explanation for the experiments on damping as represented by Ref. [4].

According to our calculation, a damping due to phonon-fermion interaction should happen in the unitary limit. While this was not reported in the experiments of Ref. [4], in the experiments of Ref. [22], the authors found that the damping rate of a Fermi gas at unitarity displays a weak peak immediately followed by a notch near phase transition from superfluid to normal state as temperature increases. Such a damping notch is consistent with the dip of Fig. 11 that we propose here.

There are several reasons for the quantitative discrepancy between our calculation and the experiments, due to the simplification we have made. The most important thing is that our calculation is based on mean field results of Δ_0 and μ from solving Eq. (4.11). Quantum fluctuations tend to destroy the superfluid phase, i.e., reduce the transition temperature T_c below the mean field results. More reliable inputs for Δ_0 and μ from a calculation including quantum fluctuations [51] will give a lower T_c, which will make our results better agree with experiments. Secondly, our calculation is based on a Fermi gas in free space while in the experiments, the gas is always trapped. Thirdly, we used approximation to solve for the damping. However, to be specific one needs to exactly solve for the poles. Also, ω_0 is read from Ref. [4] and treated as a constant in our work. That is just an approximation since ω_0 is also changing slightly with temperature.

Finally, we summarize the physical origin of the damping phenomena. As shown in Fig. 12, by varying the temperature [4] as indicated by the red arrow, our theory predicts

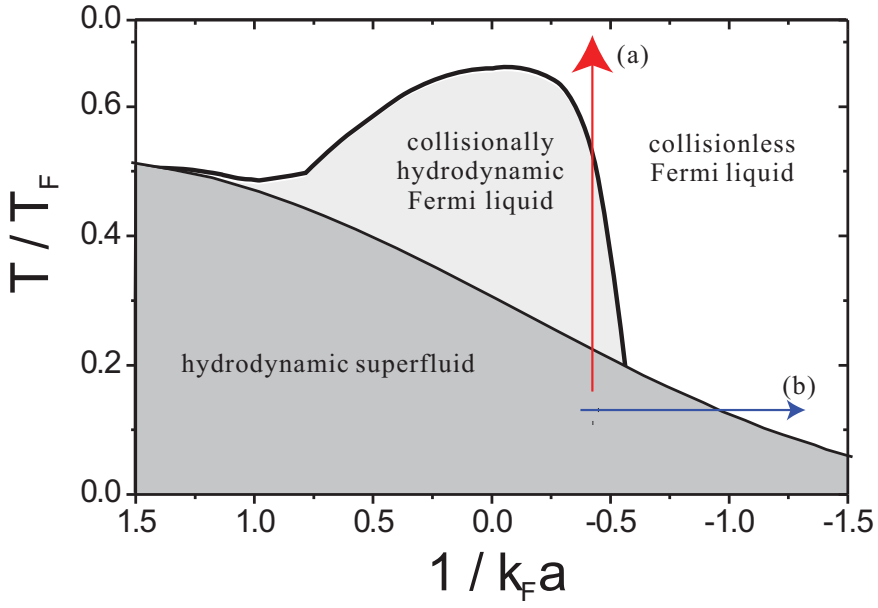

Figure 12: An illustrative phase diagram adapted from Ref. [4] showing the damping mechanism in the relative experiments. Red arrow: the evolution of system when we fix the magnetic field and vary the temperature. Blue arrow: the evolution of system when we fix the temperature and vary the magnetic field.

that one should find two peaks in the damping. The first is a sharp peak due to the finite-temperature phonon-fermionic quasiparticle interaction, and the system changes from hydrodynamic superfluid to collisionally hydrodynamic Fermi liquid. The second is a broad peak due to the transition from the collisionally hydrodynamic to collisionless Fermi liquid. In the experiment that varies the magnetic field [21, 25] but keeps temperature sufficiently low as indicated by the blue arrow in Fig. 12, one should see only the peak due to the phonon-fermionic quasiparticle interaction. After passing this peak, the system is already in the collisionless regime without the need of going across a collisionally hydrodynamic regime. Thus, there is no second broad peak.

5.0 OPTICAL LATTICE AND HUBBARD MODEL

In this chapter, we will introduce the background of optical lattices. Optical lattice is one of the most important ingredients in ultracold quantum systems. In Sec. 5.1, we will give a general introduction of optical lattices. In Sec. 5.2, we will present the Hubbard model description of optical lattices, which is the most widely used theoretical model to study many-body physics of optical lattice systems. In Sec. 5.3, we will introduce the time-of-flight imaging method of measurement in optical lattice experiments. In Sec. 5.4, we will use mean field analysis to discuss the quantum phase transition in the Bose-Hubbard model.

5.1 FROM THREE DIMENSIONAL TO ZERO DIMENSIONAL

Optical lattices are very useful tools to simulate conventional condensed matter materials, by using laser beams to create periodic potential, and using ultracold fermionic atoms to simulate the electrons. In addition to simulate the electronic condensed matter systems, we can also load bosons or single-species fermions onto optical lattices, and we can control the hopping and interaction relatively easily. Optical lattices use off-resonance laser beams to generate a spatially varying potential for atoms via the AC Stark effect. To create a periodic lattice potential by laser beam, one can overlap two counter-propagating laser beams. By interference a standing wave with period $\lambda/2$ can be formed. As mentioned in Chapter 2, the atom is blue (red) detuned if the laser frequency ω_L is greater (smaller) than the resonance frequency ω_0. In the blue (red) detuned case, the atoms will be trapped at the node (anti-node) position of the standing wave. We consider the blue-detuned case and place the laser beams in one direction of the 3D space, i.e., $V(\mathbf{r}) = V_x \sin^2 kx$. The atoms can still move

freely in the yz plane, and in x direction it is confined to each lattice site. Such a system can be viewed as weakly coupled 2D planes, or quantum wells, and the inter-plane coupling can be tuned by changing the laser power V_x.

If we apply another perpendicular laser beam with a different polarization or a slightly different frequency to avoid interference with the first laser beam, the resulting potential $V(\mathbf{r}) = V_x \sin^2 kx + V_y \sin^2 ky$ imposes lattice confinements in both x and y directions and the atoms can move freely in z direction. The system can be viewed as weakly coupled 1D tubes. A recent experiment searching for a FFLO superconductive phase has been applied in such a quasi-one-dimensional system [33].

When adding the third perpendicular laser beam with a slightly different frequency, the system can be viewed as zero-dimensional weakly coupled points, i.e., a 3D optical lattice with lattice potential $V(\mathbf{r}) = V_x \sin^2 kx + V_y \sin^2 ky + V_z \sin^2 kz$. The lattice potential V_x, V_y and V_z can be tuned to form anisotropic lattices. Experiments studying the Bose-Hubbard model [8] and Fermi-Hubbard Model [26] have been carried on 3D isotropic optical lattices.

There are many other possibilities than the above cases. For example, by intersecting laser beams with some angles rather than perpendicular to each other, or adjusting the frequency and the power of laser beams, triangular [66], honeycomb lattices [67, 17], and unconventional bipartite square optical lattices [16, 15] can be formed in experiments. In a word, different types of optical lattices can be achieved in experiments by manipulating laser beams, which provides various platforms to study ultracold atoms in periodic lattice potentials.

5.2 THEORY OF THE HUBBARD MODEL

5.2.1 From Field theory to Hubbard Model

In this section, we will discuss the theoretical approach to obtain Hubbard model from a general second-quantized field theory. In current theoretical study on lattice systems, the Hubbard model is extremely important and is the most widely used model. In 1998, D.

Jaksch et al. suggest that the optical lattice system is almost the best candidate to realize Hubbard model [68].

The Hubbard model is a second-quantized model in the Wannier basis [69], where the tight-binding approximation is applied. For simplicity, here we only consider a simple cubic spin-independent optical lattice with N^3 sites. We use $\mathbf{j} = (j_i, j_2, j_3)$ to label the sites, where the position of sites $\mathbf{j}$ is given by $\mathbf{R_j} = a\mathbf{j}$ with lattice constant a.

As discussed before, the spatial lattice potential has the form $V_{ol}(\mathbf{r}) = \sum_\nu V_\nu \sin^2(k\nu)$. Here ν runs over x, y, and z, and k is the wave vector of the laser beams, where the lattice constant is given by $a = \pi/k$. The lattice potential V_{ol} can also be written as the sum of a series of local potential $V_{ol}(\mathbf{r}) = \sum_j V_{loc}(\mathbf{r} - \mathbf{R_j})$ where

$$V_{loc}(\mathbf{r}) = \begin{cases} \sum_\nu V_\nu \sin^2(k\nu), & \mathbf{r} \in \left[-\frac{\mathbf{a}}{2}, \frac{\mathbf{a}}{2}\right] \\ 0, & \text{elsewhere.} \end{cases} \tag{5.1}$$

Bloch's theorem states that the eigenstates of a lattice system with periodic potential can always be written in the form $\phi_\mathbf{k}(\mathbf{r}) = e^{i\mathbf{k}\cdot\mathbf{r}} u_\mathbf{k}(\mathbf{r})$, where $u_\mathbf{k}(\mathbf{r})$ is a periodic function with the same period of the lattice. We call $\phi_\mathbf{k}$'s Bloch states. In solid state physics we usually apply periodic boundary conditions to the system. The momenta are quantized as $\mathbf{k} = (N_x, N_y, N_z)2\pi/Na$ and confined in the first Brillouin zone. The first Brillouin zone corresponds to $N_x, N_y, N_z \in [0, N-1]$ with N_x, N_y, N_z integers. We can define the Wannier functions

$$W_\mathbf{j}(\mathbf{r}) \equiv W(\mathbf{r} - \mathbf{R_j}) = \frac{1}{\sqrt{N}} \sum_\mathbf{k} \phi_\mathbf{k}(\mathbf{r}) e^{-i\mathbf{k}\cdot\mathbf{R_j}}, \tag{5.2}$$

and it can be shown that Wannier functions, which are relatively localized around each lattice site $\mathbf{R_j}$, also form a complete and orthogonal basis in the lattice system. Wannier functions provide an alternative basis to describe the periodic lattice potential problems, which is very useful in tight-binding limit where the particles are highly localized at each lattice site.

In general, both Bloch functions and Wannier functions are difficult to obtain. A commonly used approximation is called the tight-binding approximation. In this approach, the Wannier functions can be found approximately by solving a local Schrödinger equation, and then the Bloch functions can be constructed as the inverse Fourier transform of Eq. (5.2)

$$\phi_\mathbf{k}(\mathbf{r}) = \frac{1}{\sqrt{N}} \sum_\mathbf{j} W_\mathbf{j}(\mathbf{r}) e^{i\mathbf{k}\cdot\mathbf{R_j}}. \tag{5.3}$$

In the tight-binding approximation, instead of using the full V_{ol} to solve the Schrödinger equation, we focus on the local potential V_{loc} Eq. (5.1) and solve the local Schrödinger equation

$$\left[\frac{\hbar^2\nabla^2}{2m} + V_{loc}(\mathbf{r}-\mathbf{R_j})\right]\varphi_{\mathbf{j}}(\mathbf{r}) = \varepsilon\varphi_{\mathbf{j}}(\mathbf{r}), \tag{5.4}$$

where $\varphi_{\mathbf{j}} \equiv \varphi(\mathbf{r}-\mathbf{R_j})$. Assuming the lattice potential is deep and particles are tightly bound at each site, the above approximation is valid. We can write the solutions to Eq. (5.4) as $\varphi_{n\mathbf{j}}(\mathbf{r})$, where n labels the nth eigenenergy ε_n. Because the states obtained from Eq. (5.4) are highly localized at each site, their overlap between different sites is very small and can be viewed as approximately zero, i.e., we have the orthogonal relationship $\int d^3\mathbf{r}\varphi^*_{n\mathbf{j}}(\mathbf{r})\varphi_{n'\mathbf{j}'}(\mathbf{r}) \approx \delta_{nn'}\delta_{\mathbf{jj}'}$. Therefore, $\varphi_{n\mathbf{j}}(\mathbf{r})$ can be used to approximate the Wannier function $W_{n\mathbf{j}}(\mathbf{r})$, and we will see in the following that the index n labeling the different local energy states becomes the band index.

With the above background knowledge on solid state physics, we can proceed to construct the Hubbard model. The Hamiltonian can be written as

$$\hat{H} = \hat{H}_K + \hat{H}_I, \tag{5.5}$$

where

$$\begin{aligned}
\hat{H}_K &= \sum_\sigma \int d^3\mathbf{r}\hat{\psi}^\dagger_\sigma(\mathbf{r})\left(\frac{\hbar^2\nabla^2}{2m} + V_{ol}(\mathbf{r}) - \mu_\sigma\right)\hat{\psi}_\sigma(\mathbf{r}) \\
\hat{H}_I &= \frac{1}{2}\sum_{\sigma\sigma'}\int d^3\mathbf{r}\int d^3\mathbf{r}'\hat{\psi}^\dagger_\sigma(\mathbf{r})\hat{\psi}^\dagger_{\sigma'}(\mathbf{r}')V_I(\mathbf{r}-\mathbf{r}')\hat{\psi}_{\sigma'}(\mathbf{r}')\hat{\psi}_\sigma(\mathbf{r})
\end{aligned} \tag{5.6}$$

are the single-particle kinetic energy and the inter-particle interaction parts. The field operators can be expanded in the Wannier basis as

$$\hat{\psi}_\sigma(\mathbf{r}) = \sum_{n\mathbf{j}\sigma} W_{n\mathbf{j}}(\mathbf{r})\hat{c}_{n\mathbf{j}\sigma} \approx \sum_{n\mathbf{j}\sigma}\varphi_{n\mathbf{j}}(\mathbf{r})\hat{c}_{n\mathbf{j}\sigma}, \tag{5.7}$$

where $\hat{c}_{n\mathbf{j}\sigma}$ is the annihilation operator of Wannier state at site $\mathbf{j}$ with spin σ. The Wannier function has no spin dependence since the lattice potential is spin-independent.

We first consider the kinetic energy part $\hat{H}_K$ in Eq. (5.6). The last term of $\hat{H}_K$ is easy to obtain by the orthogonality of Wannier functions as

$$\sum_{n\mathbf{j}\sigma} \mu_\sigma \hat{c}^\dagger_{n\mathbf{j}\sigma} \hat{c}_{n\mathbf{j}\sigma}. \tag{5.8}$$

Now consider the first two terms in $\hat{H}_K$ using Eq. (5.7), and we get

$$\sum_\sigma \sum_{nn'\mathbf{j}\mathbf{j}'} \hat{c}^\dagger_{n\mathbf{j}\sigma} \hat{c}_{n'\mathbf{j}'\sigma} \int d^3\mathbf{r} \varphi^*_{n\mathbf{j}}(\mathbf{r}) \left[\frac{\hbar^2 \nabla^2}{2m} + V_{ol}(\mathbf{r}) \right] \varphi_{n'\mathbf{j}'}(\mathbf{r}). \tag{5.9}$$

For simplicity, we only consider nearest neighbor hopping, which means regarding in the summation over $\mathbf{j}\mathbf{j}'$, only $|\mathbf{j}-\mathbf{j}'| = 0, 1$ terms are taken into account. The lattice potential V_{ol} can be written as the sum of local potential Eq. (5.1), and by approximation we only keep the local potential at sites $\mathbf{j}, \mathbf{j}'$. For $\mathbf{j} = \mathbf{j}'$, we only need to keep the $\mathbf{R_j}$ local potential and get the onsite term

$$\sum_{\sigma n\mathbf{j}} \varepsilon_n \hat{c}^\dagger_{n\mathbf{j}\sigma} \hat{c}_{n\mathbf{j}\sigma}. \tag{5.10}$$

For the hopping term between nearest sites, without loss of generality, we consider $\mathbf{j} = 0$ and $\mathbf{j}' = \mathbf{j} + \mathbf{e}_x$, where $\mathbf{e}_x$ is the unit vector in x direction. The hopping integral term between state n at $\mathbf{j} = (0,0,0)$ and state n' at $\mathbf{j}' = (1,0,0)$ in Eq. (5.9) is given by

$$t^{nn'} \equiv -\int d^3\mathbf{r} \varphi^*_n(\mathbf{r}) \left[\frac{\hbar^2 \nabla^2}{2m_a} + V_{ol}(\mathbf{r}) \right] \varphi_{n'}(\mathbf{r} - a\mathbf{e}_x), \tag{5.11}$$

which can be reduced to

$$\begin{aligned} t^{nn'} &= -\int d^3\mathbf{r} \varphi^*_n(\mathbf{r}) \left[\frac{\hbar^2 \nabla^2}{2m_a} + V_{loc}(\mathbf{r}) + V_{loc}(\mathbf{r} - a\mathbf{e}_x) \right] \varphi_{n'}(\mathbf{r} - a\mathbf{e}_x), \\ &= -\frac{1}{2} \int d^3\mathbf{r} \varphi^*_n(\mathbf{r}) \left[V_{loc}(\mathbf{r}) + V_{loc}(\mathbf{r} - a\mathbf{e}_x) \right] \varphi_{n'}(\mathbf{r} - a\mathbf{e}_x). \end{aligned} \tag{5.12}$$

To derive Eq. (5.12), we have used the orthogonal relation for φ's.

The interaction part $\hat{H}_I$ in Eq. (5.6) can be expanded in Wannier basis in a similar manner. By considering only the onsite interaction and using Eq. (5.7) we get

$$\begin{aligned} \hat{H}_I &= \frac{1}{2} \sum_{\mathbf{j}, n_1 n_2 n_3 n_4, \sigma\sigma'} U^{n_1 n_2 n_3 n_4} \hat{c}^\dagger_{n_1\sigma\mathbf{j}} \hat{c}^\dagger_{n_2\sigma'\mathbf{j}} \hat{c}_{n_3\sigma'\mathbf{j}} \hat{c}_{n_4\sigma\mathbf{j}}, \\ U^{n_1 n_2 n_3 n_4} &= \int d^3\mathbf{r} \int d^3\mathbf{r}' \varphi^*_{n_1}(\mathbf{r}) \varphi^*_{n_2}(\mathbf{r}') V_I(\mathbf{r} - \mathbf{r}') \varphi_{n_3}(\mathbf{r}') \varphi_{n_4}(\mathbf{r}). \end{aligned} \tag{5.13}$$

The local function φ in Eq. (5.4) can be solved numerically and be applied into Eq. (5.12) and Eq. (5.13). Then we get the hopping terms t and the interaction term U. Together with Eq. (5.8) and Eq. (5.10), the Hubbard model Eq. (5.5) is obtained.

As an example, the simplest Bose-Hubbard model only considers the single-species bosons with repulsive interaction loaded on the s band (the lowest energy band). By removing the spin label σ and all the n's (since we only consider the lowest energy band), we obtain the Bose-Hubbard model

$$\hat{H}_{BH} = -t\sum_{\langle \mathbf{ij}\rangle}(\hat{b}_{\mathbf{i}}^{\dagger}\hat{b}_{\mathbf{j}} + h.c.) - \mu\sum_{\mathbf{i}}\hat{n}_{\mathbf{i}} + \frac{U}{2}\sum_{\mathbf{i}}\hat{n}_{\mathbf{i}}(\hat{n}_{\mathbf{i}} - 1). \tag{5.14}$$

Here, $\hat{n}_{\mathbf{i}} = \hat{b}_{\mathbf{i}}^{\dagger}\hat{b}_{\mathbf{i}}$ is the number operator at site $\mathbf{i}$, and $t, U > 0$ are the hopping and onsite repulsive interaction. The $\langle \mathbf{ij}\rangle$ means the summation over nearest neighbors. The chemical potential μ here is the combination of Eq. (5.8) and Eq. (5.10), which tells the effective chemical potential with respect to the local s-orbital eigenenergy. In Sec. 5.4, we will use mean field theory to study this Bose-Hubbard model, and show the quantum phase transitions in this system.

5.2.2 Harmonic Approximation

The coefficients t, U obtained before in general need numerical evaluation. Nevertheless, in the tight-binding regime, we can use the harmonic approximation to estimate these coefficients analytically as follows. We consider the site at origin with $\mathbf{j} = 0$. If the lattice potential is very deep, the wave function will be highly localized around $\mathbf{r} = 0$, which means we only need to consider the lattice potential near $\mathbf{r} = 0$. Therefore, in Eq. (5.1), we are in the region that $k\nu \ll 1$, and the local lattice potential can be approximately described by the following harmonic oscillator potential form

$$V_{loc}(\mathbf{r}) \approx V'_{loc}(\mathbf{r}) = \sum_{\nu} V_\nu k^2\nu^2 = \frac{1}{2}m_a\omega_x^2x^2 + \frac{1}{2}m_a\omega_y^2y^2 + \frac{1}{2}m_a\omega_z^2z^2, \tag{5.15}$$

where $\omega_\nu = \sqrt{2V_\nu k^2/m_a}$. The local Hamiltonian Eq. (5.4) reduces to a harmonic oscillator problem with energy levels $\varepsilon_{\mathbf{n}} = \sum_\nu(n_\nu + \frac{1}{2})\hbar\omega_\nu$, where we have $\mathbf{n} = (n_x, n_y, n_z)$ with

n_x, n_y, n_z non-negative integers. The eigenstates are given by $\varphi_{\mathbf{n}}(\mathbf{r}) = \varphi_{n_x}(x)\varphi_{n_y}(y)\varphi_{n_z}(z)$, where $\varphi_{n_x}(x)$ is the wave function of a 1D harmonic oscillator

$$\varphi_{n_x} = \left(\frac{\alpha_x}{\sqrt{\pi}2^{n_x}n_x!}\right)^{\frac{1}{2}} \mathrm{H}_n(\alpha_x x)e^{-\frac{1}{2}\alpha_x^2 x^2}. \tag{5.16}$$

Here, H_{n_x} is n_xth-degree Hermite polynomials and $\alpha_x = \sqrt{m_a\omega_x/\hbar}$. We can also express α_x as $\alpha_x = (V_x/E_R)^{\frac{1}{4}}\, k$ where the recoil energy E_R is defined as $E_R = \hbar^2k^2/2m_a$. It is the kinetic energy of the atom after emitting a lattice photon with wave vector k, given that the atom is initially at rest.

We can then evaluate the hopping term between different sites analytically under harmonic approximation. First we consider hopping of s-band atoms, where the wave function reads $\varphi_{\mathbf{0}}(\mathbf{r}) = \varphi_0(x)\varphi_0(y)\varphi_0(z)$. Here $\varphi_0(\nu)$ is the lowest wave function of 1D harmonic oscillator

$$\varphi_0(\nu) = \left(\frac{\alpha_\nu}{\sqrt{\pi}}\right)^{\frac{1}{2}} e^{-\frac{1}{2}\alpha_\nu^2\nu^2}. \tag{5.17}$$

For two Gaussian wave functions as in Eq. (5.17) highly localized at 0 and $a\mathbf{e}_x$, the maximum overlap is at the center between them, i.e., $a\mathbf{e}_x/2$. Therefore, we can expand the potential V_{loc} around $a\mathbf{e}_x/2$, and then carry out the integral Eq. (5.12) analytically. The hopping between nearest neighbors of s band in x direction reduces to

$$t_s = V_x k^2 \int d^3r\varphi_0\left(x-\frac{a}{2}\right)\varphi_0(y)\varphi_0(z)x^2\varphi_0\left(x+\frac{a}{2}\right)\varphi_0(y)\varphi_0(z) = \frac{\hbar^2\alpha_x^2}{4m_a}e^{-\frac{1}{4}\alpha_x^2a^2}, \tag{5.18}$$

where we have used Eq. (5.17) for φ. Similarly, we can evaluate the hopping of atoms on p_x band in x direction as

$$t_p = V_x k^2 \int d^3r\varphi_1\left(x-\frac{a}{2}\right)\varphi_0(y)\varphi_0(z)x^2\varphi_1\left(x+\frac{a}{2}\right)\varphi_0(y)\varphi_0(z) = -\frac{1}{2}(\alpha_x^2a^2-6)t_s. \tag{5.19}$$

Here, $\varphi_1(x) = \left(\frac{\alpha_\nu}{\sqrt{\pi}}\right)^{\frac{1}{2}}\sqrt{2}\alpha x e^{-\frac{1}{2}\alpha_x^2x^2}$ is the wave function of the first excited state in the harmonic oscillator potential.

The interaction term Eq. (5.13) can be obtained similarly. For simplicity, we consider the contact interaction $V_I(\mathbf{r}-\mathbf{r}') = V\delta(\mathbf{r}-\mathbf{r}')$ in Eq. (5.13), and the interaction term for the s-band atoms reduces to

$$U = V\int d^3\mathbf{r}\varphi_0^4(x)\varphi_0^4(y)\varphi_0^4(z) = V\frac{\alpha_x\alpha_y\alpha_z}{(2\pi)^{3/2}}. \tag{5.20}$$

Harmonic approximation provides a good estimation for the Wannier functions in the tight-binding regime, which becomes better as we consider deeper lattice potential, as shown in Table I of Ref. [70].

5.3 TIME-OF-FLIGHT IMAGING

Time-of-flight imaging is a widely used measuring method in ultracold experiments with optical lattices. In this section, we will study the time-of-flight imaging from theoretical side. This method is very useful and provides a simple way to detect the momentum distribution of the state, which can be further interpreted to understand the state of the system.

Suppose we have an optical lattice system with atoms loaded, and we suddenly release the lattice at $t_0 = 0$. The atoms will then expand freely, and we can take snapshots of them at a certain time t to obtain the density distribution in space. We assume that during this free expansion the atoms are non-interacting. At time t, the average density at space position $\mathbf{r}$ is given by the expectation in Heisenberg picture

$$n(\mathbf{r}, t) = \langle \hat{\psi}^\dagger(\mathbf{r}, t)\hat{\psi}(\mathbf{r}, t)\rangle, \tag{5.21}$$

where $\hat{\psi}(\mathbf{r}, t)$ is the field operator at position $\mathbf{r}$ and time t, and $\langle ...\rangle$ means the expectation value with initial condition being the state at $t_0 = 0$, i.e., the state of the optical lattice system. The field operator $\hat{\psi}(\mathbf{r}, t)$ can be written as

$$\hat{\psi}(\mathbf{r}, t) = \int d^3\mathbf{r_1}\langle \mathbf{r}, t|\mathbf{r_1}, 0\rangle\hat{\psi}(\mathbf{r_1}). \tag{5.22}$$

Here, $|\mathbf{r}, t\rangle$ is the position basis at time t in Schrödinger picture, and $\langle \mathbf{r}, t|\mathbf{r_1}, 0\rangle$ is just the free single-particle propagator

$$G_0(\mathbf{r}, t; \mathbf{r_1}, 0) = \left(\frac{m_a}{i\hbar t}\right)^{3/2} e^{i\frac{m_a}{2\hbar t}(\mathbf{r}-\mathbf{r_1})^2}, \tag{5.23}$$

which can be obtained directly from the Schrödinger equation or a path integral approach. Then Eq. (5.21) reduces to

$$n(\mathbf{r}, t) = \left(\frac{m_a}{\hbar t}\right)^3 \int d^3\mathbf{r_1}d^3\mathbf{r_2}e^{i\frac{m_a}{2\hbar t}(\mathbf{r_1}-\mathbf{r_2})(2\mathbf{r}-\mathbf{r_1}-\mathbf{r_2})}\langle \hat{\psi}^\dagger(\mathbf{r_1})\hat{\psi}(\mathbf{r_2})\rangle, \tag{5.24}$$

where $\langle ... \rangle$ has the same meaning as before. We set the system at origin of coordinates and assume that the system size is much smaller than the measurement distance $\mathbf{r}$. Therefore, we can use the approximation $2\mathbf{r} - \mathbf{r_1} - \mathbf{r_2} \approx 2\mathbf{r}$, since the term $\langle \hat{\psi}^\dagger(\mathbf{r_1})\hat{\psi}(\mathbf{r_2})\rangle$ selects $\mathbf{r_1}, \mathbf{r_2}$ only within the system size. Using Fourier transform we reach the expression

$$n(\mathbf{r}, t) = \left(\frac{m_a}{\hbar t}\right)^3 n(\mathbf{k}), \tag{5.25}$$

where $n(\mathbf{k}) = \langle \hat{a}^\dagger_{\mathbf{k}} \hat{a}_{\mathbf{k}} \rangle$ with $\mathbf{k} = m_a \mathbf{r}/\hbar t$. Here, $\hat{a}_{\mathbf{k}}$ is the annihilation operator of the free particle of wave vector $\mathbf{k}$. Eq. (5.25) can also be understood in a semi-classical way. At time t after releasing the lattice, the atom density at distance $\mathbf{r}$ is proportional to the average number of atoms at velocity $\mathbf{r}/t$, with wave vector $\mathbf{k} = m_a \mathbf{r}/\hbar t$ correspondingly.

To map the above operator $\hat{a}_{\mathbf{k}}$ to lattice wave vector $\mathbf{p}$, we apply the following transformation for $\hat{a}_{\mathbf{k}}$ as

$$\hat{a}^\dagger_{\mathbf{k}} = \int d^3\mathbf{r} \sum_{\mathbf{p}\mathbf{j}m} e^{i\mathbf{p}\cdot\mathbf{R_j}} W^*_{m\mathbf{j}}(\mathbf{r}) e^{-i\mathbf{k}\cdot\mathbf{r}} \hat{a}^\dagger_{m\mathbf{p}}, \tag{5.26}$$

where we have used the Bloch basis, Wannier basis, and real space expansions subsequently. Here the summation over bands is labeled by m. For Wannier functions, we know that $W_{m\mathbf{j}}(\mathbf{r}) = W_m(\mathbf{r} - \mathbf{R_j})$, which means the Wannier functions in the same band are the same functions with different centers. Therefore, by adding the identity $e^{-i\mathbf{k}\cdot\mathbf{R_j}} e^{i\mathbf{k}\cdot\mathbf{R_j}}$ to each site of Eq. (5.26), it reduces to

$$\hat{a}^\dagger_{\mathbf{k}} = \sum_{\mathbf{p}\mathbf{j}m} e^{i\mathbf{p}\cdot\mathbf{R_j}} W^*_m(\mathbf{k}) e^{-i\mathbf{k}\cdot\mathbf{R_j}} \hat{a}^\dagger_{m\mathbf{p}}, \tag{5.27}$$

where $W_m(\mathbf{k})$ is the Fourier transformation of the Wannier function with band index m. Afterward, the summation over $\mathbf{j}$ in Eq. (5.27) yields a delta function $\delta_{\mathbf{p},\bar{\mathbf{k}}}$. Here $\bar{\mathbf{k}}$ is the wave vector in the first Brillouin zone corresponding to $\mathbf{k}$, i.e., $\mathbf{k} = \bar{\mathbf{k}} + \mathbf{G}$, where $\mathbf{G}$ is a reciprocal lattice vector that makes $\bar{\mathbf{k}}$ in the first Brillouin zone. Eq. (5.27) then reduces to

$$\hat{a}^\dagger_{\mathbf{k}} = \sum_m W^*_m(\mathbf{k}) \hat{a}^\dagger_{m\bar{\mathbf{k}}}, \tag{5.28}$$

which leads to the result

$$\langle \hat{a}^\dagger_{\mathbf{k}} \hat{a}_{\mathbf{k}} \rangle = \sum_m W^*_m(\mathbf{k}) W_m(\mathbf{k}) \langle \hat{a}^\dagger_{m\bar{\mathbf{k}}} \hat{a}_{m\bar{\mathbf{k}}} \rangle. \tag{5.29}$$

With Eq. (5.29) plugging into Eq. (5.25), we reach the final expression

$$n(\mathbf{r},t)=\left(\frac{m_a}{\hbar t}\right)^3\sum_m W_m^*(\mathbf{k})W_m(\mathbf{k})\langle\hat{a}^\dagger_{m\bar{\mathbf{k}}}\hat{a}_{m\bar{\mathbf{k}}}\rangle. \tag{5.30}$$

By measuring $n(\mathbf{r},t)$, we can extract information such as momentum distribution of the initial state (the optical lattice state) from Eq. (5.30). In the higher-orbital BEC problems as discussed in Chapter 8, time-of-flight imagining method can provide direct evidence of condensate at finite momentum.

5.4 BOSE HUBBARD MODEL

In this section, we will use mean field theory to study the simplest Bose-Hubbard model Eq. (5.14) obtained in Sec. 5.2. Bose-Hubbard model is a very simple but extremely important model in lattice problems [71]. We will show that by tuning the parameters, at $T=0$ a phase transition can happen in this model. Since the phase transition is at zero temperature, this Bose-Hubbard model provides the simplest example of the quantum phase transition.

We consider single-species bosonic atoms loaded in a 3D cubic isotropic optical lattice system. Recall the Bose-Hubbard model obtained in Sec. 5.2

$$\hat{H}_{BH}=-t\sum_{\langle\mathbf{ij}\rangle}(\hat{b}^\dagger_{\mathbf{i}}\hat{b}_{\mathbf{j}}+h.c.)-\mu\sum_{\mathbf{i}}\hat{n}_{\mathbf{i}}+\frac{U}{2}\sum_{\mathbf{i}}\hat{n}_{\mathbf{i}}(\hat{n}_{\mathbf{i}}-1). \tag{5.31}$$

First we consider the two limiting cases. When $t/U\to 0$, the system is dominated by the onsite repulsive interaction. At integer filling, e.g., one particle per site, the particles are localized since a particle moving from one site to another will cost a repulsive energy U. It is an insulating state called Mott insulator, which is also the eigenstate of $\hat{n}_{\mathbf{i}}$. On the other hand, when $t/U\gg 1$, the system reduces to a weakly repulsive bosonic gas, which we know has a condensate at low T. In this case, the local particle number is not a good quantum number and the system is not insulator. Therefore, for intermediate values of t/U, there should be some phase transitions between the above two limiting cases.

To apply mean field analysis, we write $\hat{b}_i$ as

$$\hat{b}_i = \hat{b}_i - \langle \hat{b}_i \rangle + \langle \hat{b}_i \rangle, \tag{5.32}$$

where $\langle ... \rangle$ means the ground state expectation value. In the mean field approximation, we assume that $\langle \hat{b}_i \rangle$ is independent of i and we can write it as

$$\langle \hat{b}_i \rangle = \phi, \tag{5.33}$$

where ϕ serves as the order parameter. By plugging Eq. (5.32) into Eq. (5.31) and ignoring second order terms in $\hat{b}_i - \langle \hat{b}_i \rangle$, different sites are decoupled and identical, which yields the mean field Hamiltonian of one site

$$\hat{H}_{MF} = -Zt(\hat{b}^\dagger \phi + \hat{b}\phi^*) - \mu\hat{n} + \frac{U}{2}\hat{n}(\hat{n}-1) - Zt\phi^2, \tag{5.34}$$

where the previous $\hat{b}_i$ and $\hat{n}_i$ are rewritten as $\hat{b}$ and $\hat{n}$ since they are independent of i. Here, Z is the number of neighbors of one site. In 3D cubic lattice case $Z = 6$. We now use the Fock basis $|m\rangle$, where m is the occupation number of the state. A cutoff of m must be set, and for $m \gg \mu/U$, the state $|m\rangle$ has very small contribution, which can be checked by increasing m and observe how the result changes. We also set ϕ as real, which means $\phi^* = \phi$ in Eq. (5.34).

Eq. (5.33) and Eq. (5.34) can be solved self-consistently. In Fig. 13(a) and (b), we show the order parameter $\phi = \langle \hat{b} \rangle$, and the occupation number $\langle \hat{b}^\dagger \hat{b} \rangle$, with the cutoff $M = 10$. In Fig. 13(c) and (d), we show the boundaries where ϕ changes from zero to non-zero value, and where the particle number per site changes from integer to non-integer value. We can see that when $\phi = 0$, the particle number per site is integer, which indicates the Mott insulator nature of the system. When $\phi \neq 0$, the particle number per site is fractional.

Mean field theory provides a qualitative study of the quantum phase transition in the Bose-Hubbard model, which presents the existence of the two distinguished phases and a fair estimation of the phase boundary. Numerical studies on this model have been carried on and show more precise results. For example, a recent quantum Monte Carlo study of the 3D Bose-Hubbard model in a simple cubic lattice found that when the average filling factor is $\tilde{n} = 1$, the phase transition is at $(U/t)_c = 29.34$ [72, 70].

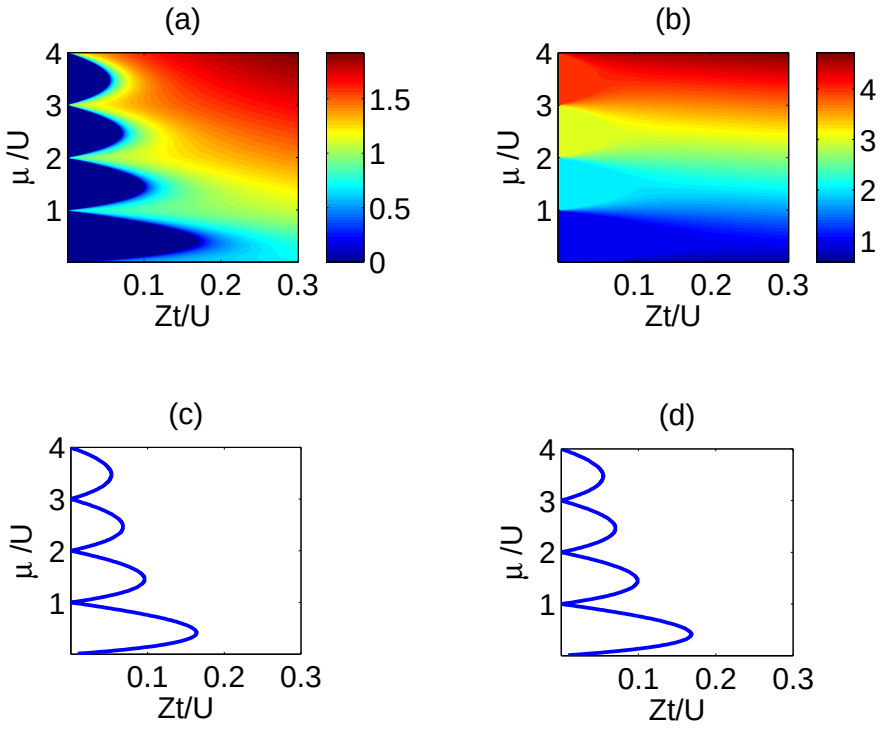

Figure 13: Mean field result of Bose-Hubbard model. (a) The phase diagram showing the value of the order parameter $\langle \hat{b} \rangle = \phi$ with varying chemical potential and hopping. (b) The corresponding particle number per site. (c) The contour showing the transition where ϕ changes from zero to non-zero value. (d) The contour showing the transition where the particle number per site changes from integer to non-integer value.

6.0 MULTI-BAND FERMIONIC SUPERCONDUCTIVITY

In this chapter, we will study a novel fermionic superconductivity for fermions in optical lattices, where the pairing of two-species fermions with mismatched Fermi surfaces on s- and p-orbital bands is studied [35]. Pairing with mismatched Fermi surfaces has long fascinated researchers in the fields of heavy fermion and organic superconductors [73, 74, 75], color superconductivity in quark matter [76], and, most recently, ultracold Fermi gases with spin imbalance [23, 77, 78, 79]. In a classic two-component model for superconductivity, the mismatch arises from the spin polarization of fermions in the same energy band. Its effect was predicted to produce intriguing, unconventional superfluids such as Fulde-Ferrell-Larkin-Ovchinnikov (FFLO) phase [31, 32], deformed Fermi surface [80, 81], and breached pair phases [82, 83]. The limiting case of large spin imbalance was also studied to explore the formation of Fermi polarons [84]. In parallel, the behavior of particles in the higher orbital bands of optical lattices, due to large filling factors, thermal excitations or strong interactions, is widely studied for novel orbital orderings of both bosons [12, 11, 13] and fermions [85, 86] with repulsive interactions. Recently, interband pairing of unpolarized fermions was shown theoretically to give rise to Cooper pair density waves [87].

We will focus on a fermion pairing phase resulting from the interplay of Fermi surface mismatch and p-orbital band physics. In such a phase, the pair condensate wave function is spatially modulated and has a p-wave symmetry. This phase arises in an attractive two-component Fermi gas on anisotropic optical lattices under a previously unexplored condition of spin imbalance. Namely the majority ($\uparrow$) spin and the minority ($\downarrow$) spin occupy up to Fermi levels lying in the p_x and s bands, respectively. We show that pairings take place near the respective Fermi surfaces of the spin $\uparrow$ fermions in p_x band and $\downarrow$ fermions in s band. This induces a modulated p-orbital pair condensate that differs from the usual p-wave

superfluids such as ^{3}He. The state requires only an on-site isotropic contact interaction and the pair is a spin singlet, while the ^{3}He p-wave superconductivity has to involve anisotropic interaction and spin triplet. The modulation wave vector of the order parameter is $Q \approx k_{F\uparrow} + k_{F\downarrow}$, where $k_{F\uparrow}$, $k_{F\downarrow}$ are Fermi momenta for spin $\uparrow$ and $\downarrow$ species, respectively. This $2k_F$ momentum dependence is an unprecedented signature in superfluids other than the spin- and charge- density waves. In the strongly attractive limit, tightly bound pairs condense at finite momentum Q, which realizes an unconventional Bose-Einstein condensate beyond Feynman's no-node theorem [12, 11, 88, 13, 89].

6.1 FULDE-FERRELL-LARKIN-OVCHINNIKOV SUPERCONDUCTIVITY

In this section, we will discuss the FFLO superconductivity, which can help better understand the multi-band fermionic superconductivity afterward. Consider a two-component fermionic system where we label the two species as spin $\uparrow$ and $\downarrow$. In the usual BCS pairing mechanism, the spin $\uparrow$ and $\downarrow$ components have the same populations as shown in Fig. 14(a). In the grand canonic ensemble, it means that they have the same chemical potential $\mu_\uparrow = \mu_\downarrow$. As a result, the two Fermi spheres are identical in momentum space. With attractive interaction, a $\mathbf{k}\uparrow$ fermion can be paired with a $-\mathbf{k}\downarrow$ one. All the fermions near the Fermi surface can be paired in this manner, and all the pairs have the same center-of-mass momentum (CMM), which is zero.

In contrast, in the case of FFLO superconductivity, the two species do not have the same population, i.e., $\mu_\uparrow \neq \mu_\downarrow$, and the Fermi surfaces mismatch (Zeeman splitting) occur as shown in Fig. 14(b). Such Fermi surfaces can be realized by a ultracold fermionic gas with two species of different particle numbers. In this case, there is no way to pair the fermions such that all the Cooper pairs have the same CMM, and the superconductivity is greatly suppressed. However, if the interaction is strong enough and exceeds the Chandrasekhar-Clogston limit [90, 91], the pairing can still happen via the usual BCS scheme and the induced Cooper pairs have finite CMM. A recent theoretical study on FFLO phase in cold atom context shows that in a 3D isotropic case, the FFLO phase only occupies a very small

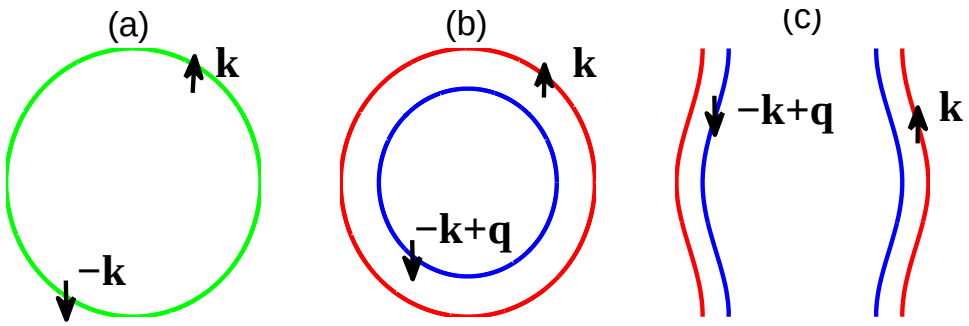

Figure 14: (a) The Fermi surfaces and pairing in BCS case where $\mu_\uparrow = \mu_\downarrow$, and the Fermi surfaces are the same for the two species. Green circle indicates the matched Fermi surfaces and the arrows denote the paired fermions $\mathbf{k}\uparrow$ and $\mathbf{k}\downarrow$. (b) The Fermi surfaces in isotropic 3D FFLO case where $\mu_\uparrow \neq \mu_\downarrow$, and the Fermi surfaces are mismatched. Red (Blue) circle: the Fermi surface for spin $\uparrow$ ($\downarrow$) fermions. There is no way to make all the pairs have the same CMM. (c) The Fermi surfaces and pairing in quasi-one-dimensional FFLO case where $\mu_\uparrow \neq \mu_\downarrow$. By pairing the $\mathbf{k}\uparrow$ fermion with $-\mathbf{k}+\mathbf{q}\downarrow$ fermion, all the pairs can have roughly the same CMM.

portion in the phase diagram, which is practically undetectable in experiments [77]. Until now, people have not found concrete experimental signatures of FFLO phases in materials yet.

An important theoretical breakthrough regarding FFLO phases in ultracold atoms is the proposal of realizing FFLO phase in a quasi-one-dimensional system [79], which can be implemented in experiments by optical lattices as discussed in Chapter 5. The quasi-one-dimensional system has such advantages that it has nested Fermi surfaces to maximize the pairing, and meanwhile it is not a 1D system where the true long range order is absent. As shown in Fig. 14(c), by pairing fermions of momentum $\mathbf{k}\uparrow$ with $-\mathbf{k}+\mathbf{q}\downarrow$, all the fermionic pairs have roughly the same CMM as $\mathbf{q}$. An experiment searching for FFLO superconductivity in such quasi-one-dimensional systems has been reported recently [33].

Since the Cooper pairs in FFLO superconductivity have non-zero CMM, we expect the

order parameter to have momentum dependence. Two commonly used ansatz of the FFLO order parameters have the form $\Delta e^{-i\mathbf{Q}\cdot\mathbf{x}}$ and $\Delta\cos\mathbf{Q}\cdot\mathbf{x}$, where the former is the FF order parameter proposed by Fulde and Ferrell [31], and the latter is the LO order parameter proposed by Larkin and Ovchinnikov [32]. In general, the LO order parameter has lower energy than the FF one. The reason is that the cosine form of LO order parameter can be viewed as a combination of FF order parameters with $\pm\mathbf{Q}$, which can pair the Fermi surfaces on both sides. In the quasi-one-dimensional system discussed before, the Cooper pair is composed by spin $\uparrow$ and $\downarrow$ fermions near their Fermi surfaces, and therefore we should have $\mathbf{Q}\approx k_{F\uparrow}-k_{F\downarrow}$ for the order parameter. Notice that, with proper filling and boundary conditions, domain wall configuration of FFLO phases is also used as the ansatz to study the phase diagram [79].

In the following sections, we will use these FF and LO ansatz for the order parameters to study multi-band superconductivity, and explicitly show that the cosine form has lower energy than the exponential form by mean field theory.

6.2 QUASI-ONE-DIMENSIONAL OPTICAL LATTICE SYSTEM AND THEORETICAL MODEL

The system under consideration is at zero temperature and consists of two-component fermions in a 3D cubic optical lattice with lattice constant a, described by the Hamiltonian

$$\begin{aligned}\hat{H} &= \sum_{\sigma}\int d^3\mathbf{x}\hat{\psi}^{\dagger}_{\sigma}(\mathbf{x})[-\frac{\hbar^2}{2m}\nabla^2+V(\mathbf{x})-\mu_{\sigma}]\hat{\psi}_{\sigma}(\mathbf{x})\\ &\quad +g\int d^3\mathbf{x}\hat{\psi}^{\dagger}_{\uparrow}(\mathbf{x})\hat{\psi}^{\dagger}_{\downarrow}(\mathbf{x})\hat{\psi}_{\downarrow}(\mathbf{x})\hat{\psi}_{\uparrow}(\mathbf{x}).\end{aligned} \tag{6.1}$$

Here $\hat{\psi}_{\sigma}(\mathbf{x})$ is the fermionic field operator at $\mathbf{x}$ with spin $\sigma=\uparrow,\downarrow$, $V(\mathbf{x})$ is the lattice potential, μ_{σ} is the chemical potential for spin σ fermions, and $g<0$ is the contact attraction which can be tuned by the Feshbach resonance. In particular, we consider the case where the

lattice potential in the x (parallel) direction is much weaker than the other two (transverse) directions, so the system behaves quasi-one-dimensionally.

As shown in Chapter 5, we expand $\hat{\psi}_\sigma(\mathbf{x}) = \sum_{n\mathbf{r}} \phi_n(\mathbf{x}-\mathbf{r})\hat{c}_{n\mathbf{r}}$, where $\phi_n(\mathbf{x}-\mathbf{r})$ is the nth band Wannier function at lattice site $\mathbf{r}$ with $\hat{c}_{n\mathbf{r}}$ the annihilation operator in Wannier basis. As a result, we obtain the usual attractive Hubbard model with nearest-neighbor hopping between ith site with orbital band α and jth site with orbital band β

$$t_{\alpha\beta} = -\int d^3\mathbf{x}\phi^*_\alpha(\mathbf{x}-\mathbf{r}_i)\left[-\frac{\hbar^2\nabla^2}{2m} + V(\mathbf{x})\right]\phi_\beta(\mathbf{x}-\mathbf{r}_j) \tag{6.2}$$

and on-site attraction between orbitals

$$U_{\alpha\beta\gamma\eta} = g\int d^3\mathbf{x}\phi^*_\alpha(\mathbf{x}-\mathbf{r}_i)\phi^*_\beta(\mathbf{x}-\mathbf{r}_i)\phi_\gamma(\mathbf{x}-\mathbf{r}_i)\phi_\eta(\mathbf{x}-\mathbf{r}_i). \tag{6.3}$$

The lowest two energy bands are the s and p_x band (the p_y and p_z band are much higher in energy because of tighter confinement in the transverse directions). For brevity the p_x band is simply called p band in the following. By filling fermions with spin $\uparrow$ to the p band and spin $\downarrow$ to the s band, the Hamiltonian becomes

$$\begin{aligned}\hat{H}_{sp} &= -\sum_{\langle\mathbf{r},\mathbf{r}'\rangle}(t^{\parallel}_s\hat{S}^\dagger_{\mathbf{r}}\hat{S}_{\mathbf{r}'} - t^{\parallel}_p\hat{P}^\dagger_{\mathbf{r}}\hat{P}_{\mathbf{r}'} + h.c.) - \mu_s\sum_{\mathbf{r}}\hat{n}^s_{\mathbf{r}} \\ &\quad -\sum_{\langle\mathbf{r},\mathbf{r}''\rangle}(t^{\perp}_s\hat{S}^\dagger_{\mathbf{r}}\hat{S}_{\mathbf{r}''} + t^{\perp}_p\hat{P}^\dagger_{\mathbf{r}}\hat{P}_{\mathbf{r}''} + h.c.) - \mu_p\sum_{\mathbf{r}}\hat{n}^p_{\mathbf{r}} \\ &\quad +\omega_b\sum_{\mathbf{r}}\hat{n}^p_{\mathbf{r}} + U_{sp}\sum_{\mathbf{r}}\hat{n}^s_{\mathbf{r}}\hat{n}^p_{\mathbf{r}}.\end{aligned} \tag{6.4}$$

Here, $\langle\mathbf{r},\mathbf{r}'\rangle$ and $\langle\mathbf{r},\mathbf{r}''\rangle$ denote the nearest neighboring lattice sites in parallel and transverse directions. $t^{\parallel}_s$ and $t^{\parallel}_p$ are the hopping amplitudes along the parallel direction for the s- and p-band fermions respectively, while $t^{\perp}_s = t^{\perp}_p = t^{\perp}$ are the hopping amplitudes in transverse directions. $\hat{S}_{\mathbf{r}}$ ($\hat{P}_{\mathbf{r}}$) is the annihilation operator at lattice site $\mathbf{r}$ for s-band $\downarrow$ (p-band $\uparrow$) fermions. $\hat{n}^s_{\mathbf{r}} = \hat{S}^\dagger_{\mathbf{r}}\hat{S}_{\mathbf{r}}, \hat{n}^p_{\mathbf{r}} = \hat{P}^\dagger_{\mathbf{r}}\hat{P}_{\mathbf{r}}$ are the number operators, and μ_s, μ_p are the corresponding chemical potentials. U_{sp} is the attractive on-site interaction between s- and p-band fermions and can be tuned by changing the scattering length using Feshbach resonance. ω_b is related to the band gap. In the tight binding region we assume $\omega_b \gg |U_{sp}|$, and consequently the s-band fully filled spin $\uparrow$ fermions are dynamically inert and not included in the $\hat{H}_{sp}$.

6.3 DMRG STUDY IN ONE DIMENSIONAL SYSTEM

First we consider the pairing problem in the simplest case of 1D ($t^{\perp} = 0$), which is schematically shown in Fig. 15(a). The two relevant Fermi momenta are $k_{F\downarrow}$ (for s-band $\downarrow$ fermions) and $k_{F\uparrow}$ (for p-band $\uparrow$ fermions). From a weak coupling point of view, to pair fermions of opposite spin near their respective Fermi surfaces, the Cooper pairs have to carry finite CMM due to Fermi surface mismatch. Furthermore, in order for all Cooper pairs to have roughly the same CMM, the only choice is to pair fermions of opposite chirality. Note that the dispersion of p band is inverted with respect to the s band, so pairing occurs between fermions with momenta of the same sign but opposite group velocities. These elementary considerations show that the CMM of the pair should be approximately the sum of two Fermi momenta,

$$Q \approx k_{F\uparrow} + k_{F\downarrow} \,. \tag{6.5}$$

This result differs from that of the usual 1D spin imbalanced fermions within the same band, where the FFLO pair momentum is the difference, $Q \approx |k_{F\uparrow} - k_{F\downarrow}|$, as found in a two-leg-ladder system [92].

Mean-field theory and weak coupling consideration can provide only a qualitative picture for 1D problems. To unambiguously identify the nature of the ground state, we use density matrix renormalization group (DMRG) [93] to compute the pair correlation function. In the numerical calculations, we used parameters $t_s^{\parallel} = 1$ as the unit of energy, $t_p^{\parallel} = 8$, $\mu_s = 1.7$, $\mu_p - \omega_b = -11$, in which the ratio between t_s and t_p is chosen according to typical tight-binding bandwidth ratio. U_{sp} is tunable with Feshbach resonance. We have tried various parameters in the DMRG and mean field calculations for 1D and quasi-one-dimensional cases respectively, and consistently found the p-orbital pair condensate. In the following calculation we will focus on $U_{sp} = -9$. The truncation error is controlled in the order of 10^{-7} or less. Eq. (6.5) predicts $Q \approx k_{F\uparrow} + k_{F\downarrow} = 0.435\pi/a$. Fig. 15(b) shows the pairing correlation function in real space $C_{ij} = \langle \hat{S}_i^{\dagger} \hat{P}_i^{\dagger} \hat{P}_j \hat{S}_j \rangle$ as a function of $x = |i - j|$ for a chain of $N = 60$ sites with open boundary condition, where the indices i and j are real space positions. Since the system only has algebraic order, $C(x)$ decays with x according to a power law. On top of this, however, there is also an obvious oscillation. A curve fit with

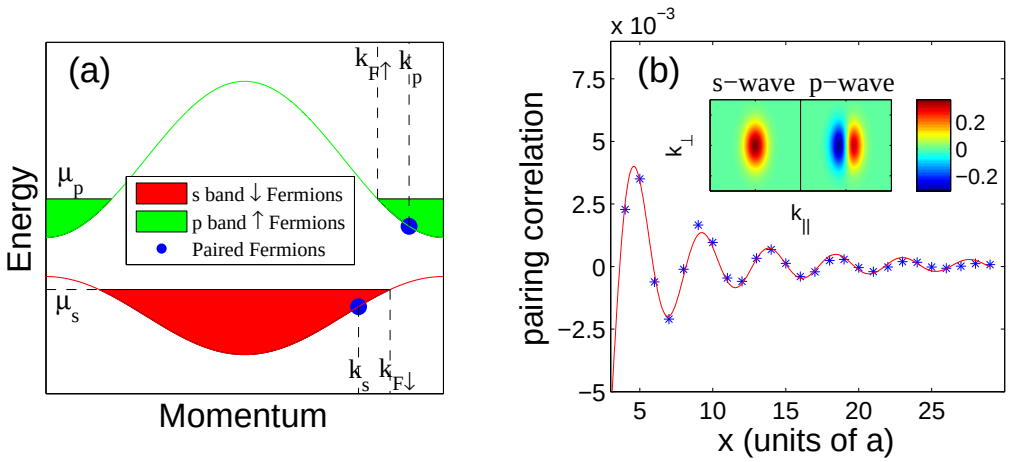

Figure 15: (a) A schematic illustration showing the pairing between s- and p-band fermions. The s band is also fully occupied with $\uparrow$ fermions (not shown). (b) The spatial variation of the pairing correlation $C(x)$ for $N_s = 49$, $N_p = 15$ according to DMRG. The blue scatters are the DMRG result and the solid line is the fitting using function $a\cos(qx + b)/x^\eta + c$. The inset in (b) shows the s- and p-wave Wannier functions in momentum space, which are elongated in the transverse direction (in real space they are compressed in transverse direction). The s-wave Wannier function has even parity while the p-wave Wannier function has odd parity.

formula $C(x) = a\cos(qx + b)/x^\eta + c$, shown in Fig. 15(b), yields a period of $q = 0.438\pi/a$, which is in good agreement with the wave number given by Eq. (6.5) before. We also get $\eta = 1.62$ from the fit. The Fourier transform of the pair correlation function

$$C_q = \frac{1}{N}\sum_{i,j} e^{iq(i-j)} C_{ij} \tag{6.6}$$

is peaked at $q = 0.426\pi/a$ (to be plotted in Sec. 6.6). These features of the pair correlation function are the signature of the existence of the $2k_F$ CMM pairing in our system [94, 95].

6.4 MEAN FIELD THEORY IN QUASI-ONE-DIMENSIONAL SYSTEM

Now we move on to the quasi-one-dimensional system where a weak transverse hopping $t^{\perp} \ll t^{\parallel}$ is added. We carry out a mean-field analysis of Hamiltonian $\hat{H}_{sp}$ by introducing the s-p pairing order parameter

$$\Delta_{\mathbf{r}} = U_{sp}\langle \hat{S}_{\mathbf{r}}\hat{P}_{\mathbf{r}}\rangle, \tag{6.7}$$

where $\langle ...\rangle$ means the ground-state expectation value. Two different trial ground states are investigated, the exponential wave $\Delta_{\mathbf{r}} = \Delta e^{i\mathbf{Q}\cdot\mathbf{r}}$, which is analogous to the FF phase and the cosine wave $\Delta_{\mathbf{r}} = \Delta\cos\mathbf{Q}\cdot\mathbf{r}$, which is analogous to the LO phase. $\mathbf{Q}$ and Δ are determined self-consistently by minimization of ground-state energy $\langle\hat{H}_{sp}\rangle$. Transverse hopping introduces a small Fermi surface curvature and spoils the perfect nesting condition as in the pure 1D problem above. However, the curvature is small for weak $t^{\perp}$. Thus, we expect $\mathbf{Q}$ pointing almost along the parallel direction, $\mathbf{Q} = Q(1,0,0)$, in order to maximize the phase space of pairing.

The mean-field Hamiltonian for the exponential wave can be diagonalized in momentum space by standard procedure as follows. We rewrite the interaction term in Eq. (6.4) as

$$U_{sp}\sum_{\mathbf{r}}\hat{n}^s_{\mathbf{r}}\hat{n}^p_{\mathbf{r}} = U_{sp}\sum_{\mathbf{r}}\left[\left(\hat{P}^{\dagger}_{\mathbf{r}}\hat{S}^{\dagger}_{\mathbf{r}} - \langle\hat{P}^{\dagger}_{\mathbf{r}}\hat{S}^{\dagger}_{\mathbf{r}}\rangle\right) + \langle\hat{P}^{\dagger}_{\mathbf{r}}\hat{S}^{\dagger}_{\mathbf{r}}\rangle\right]\left[\left(\hat{S}_{\mathbf{r}}\hat{P}_{\mathbf{r}} - \langle\hat{S}_{\mathbf{r}}\hat{P}_{\mathbf{r}}\rangle\right) + \langle\hat{S}_{\mathbf{r}}\hat{P}_{\mathbf{r}}\rangle\right]. \tag{6.8}$$

By assuming that $\hat{P}^{\dagger}_{\mathbf{r}}\hat{S}^{\dagger}_{\mathbf{r}} - \langle\hat{P}^{\dagger}_{\mathbf{r}}\hat{S}^{\dagger}_{\mathbf{r}}\rangle$ and $\hat{S}_{\mathbf{r}}\hat{P}_{\mathbf{r}} - \langle\hat{S}_{\mathbf{r}}\hat{P}_{\mathbf{r}}\rangle$ are small (mean field approximation) and ignoring the product of them, we obtain

$$U_{sp}\sum_{\mathbf{r}}\hat{n}^s_{\mathbf{r}}\hat{n}^p_{\mathbf{r}} \sim -\sum_{\mathbf{r}}\hat{P}^{\dagger}_{\mathbf{r}}\hat{S}^{\dagger}_{\mathbf{r}}\Delta_r + h.c. + \frac{|\Delta_r|^2}{U_{sp}}. \tag{6.9}$$

With the exponential ansatz $\Delta_{\mathbf{r}} = \Delta e^{i\mathbf{Q}\cdot\mathbf{r}}$, we can rewrite Eq. (6.4) and Eq. (6.9) in momentum space by Fourier transform. It leads to

$$\hat{H}_{sp} = \sum_{\mathbf{k}}(\xi^s_{\mathbf{k}}\hat{S}^{\dagger}_{\mathbf{k}}\hat{S}_{\mathbf{k}} + \xi^p_{\mathbf{k}}\hat{P}^{\dagger}_{\mathbf{k}}\hat{P}_{\mathbf{k}}) - \Delta\sum_{\mathbf{k}}(\hat{P}^{\dagger}_{\mathbf{Q}-\mathbf{k}}\hat{S}^{\dagger}_{\mathbf{k}} + h.c.) - \frac{N^3\Delta^2}{U_{sp}}. \tag{6.10}$$

Here we have the dispersion

$$\begin{aligned}
\xi^s_{\mathbf{k}} &= -2t^{\parallel}_s\cos k_x a - 2t^{\perp}\cos k_y a - 2t^{\perp}\cos k_z a - \mu_s, \\
\xi^p_{\mathbf{k}} &= 2t^{\parallel}_p\cos k_x a - 2t^{\perp}\cos k_y a - 2t^{\perp}\cos k_z a - \mu_p + \omega_b,
\end{aligned} \tag{6.11}$$

and $\hat{S}_{\mathbf{k}}$ ($\hat{P}_{\mathbf{k}}$) is the momentum space annihilation operator at lattice momentum $\mathbf{k}$ for s-band $\downarrow$ (p-band $\uparrow$) fermion, which is the Fourier transform of $\hat{S}_{\mathbf{r}}$ ($\hat{P}_{\mathbf{r}}$). N^3 is the total number of sites.

By introducing Nambu Spinor $\hat{\Psi}^{\dagger}_{\mathbf{k}} = (\hat{S}^{\dagger}_{\mathbf{k}}, \hat{P}_{\mathbf{Q}-\mathbf{k}})$, we can rewrite the Hamiltonian as

$$\hat{H}_{sp} = \sum_{\mathbf{k}} \hat{\Psi}^{\dagger}_{\mathbf{k}} \mathcal{H}_{\mathbf{k}} \hat{\Psi}_{\mathbf{k}} + \sum_{\mathbf{k}} \xi^{p}_{\mathbf{k}} - \frac{N^3\Delta^2}{U_{sp}} \tag{6.12}$$

where

$$\mathcal{H}_{\mathbf{k}} = \begin{pmatrix} \xi^{s}_{\mathbf{k}} & -\Delta \\ -\Delta & -\xi^{p}_{\mathbf{Q}-\mathbf{k}} \end{pmatrix}. \tag{6.13}$$

Eq. (6.12) is in quadratic form and can be diagonalized. At $T = 0$, we get the ground state energy

$$\langle \hat{H}_{sp} \rangle = \sum_{\mathbf{k},\gamma=\pm} \Theta(-\lambda^{(\gamma)}_{\mathbf{k}}) \lambda^{(\gamma)}_{\mathbf{k}} + \sum_{\mathbf{k}} \xi^{p}_{\mathbf{k}} - \frac{N^3\Delta^2}{U_{sp}}. \tag{6.14}$$

Here Θ is a step function, and

$$\lambda^{(\pm)}_{\mathbf{k}} = \frac{1}{2}[\xi^{s}_{\mathbf{k}} - \xi^{p}_{\mathbf{Q}-\mathbf{k}} \pm \sqrt{4\Delta^2 + (\xi^{s}_{\mathbf{k}} + \xi^{p}_{\mathbf{Q}-\mathbf{k}})^2}] \tag{6.15}$$

is the eigenenergy of the Bogoliubov quasiparticles. As evident from these formulas, the pairing occurs between an s-band fermion of momentum $\mathbf{k}$ and a p-band fermion of momentum $\mathbf{Q} - \mathbf{k}$. The order parameter Δ can be solved self-consistently from Eq. (6.7), yielding

$$1 = \frac{U_{sp}}{N^3} \sum_{\mathbf{k}} \frac{\Theta(-\lambda^{(+)}_{\mathbf{k}}) - \Theta(-\lambda^{(-)}_{\mathbf{k}})}{\sqrt{4\Delta^2 + (\xi^{s}_{\mathbf{k}} + \xi^{p}_{\mathbf{Q}-\mathbf{k}})^2}}. \tag{6.16}$$

The cosine wave ansatz $\Delta_{\mathbf{r}} = \Delta \cos \mathbf{Q} \cdot \mathbf{r}$ is spatially inhomogeneous at each lattice site, and we need to to numerically diagonalize the full Hamiltonian Eq. (6.4) for a finite size lattice. We introduce a vector of dimension $2N$

$$\hat{\alpha}^{\dagger}_{k_y k_z} = (\hat{S}^{\dagger}_{k^1_x k_y k_z} ... \hat{S}^{\dagger}_{k^N_x k_y k_z}, \hat{P}_{k^1_x, -k_y, -k_z} ... \hat{P}_{k^N_x, -k_y, -k_z}), \tag{6.17}$$

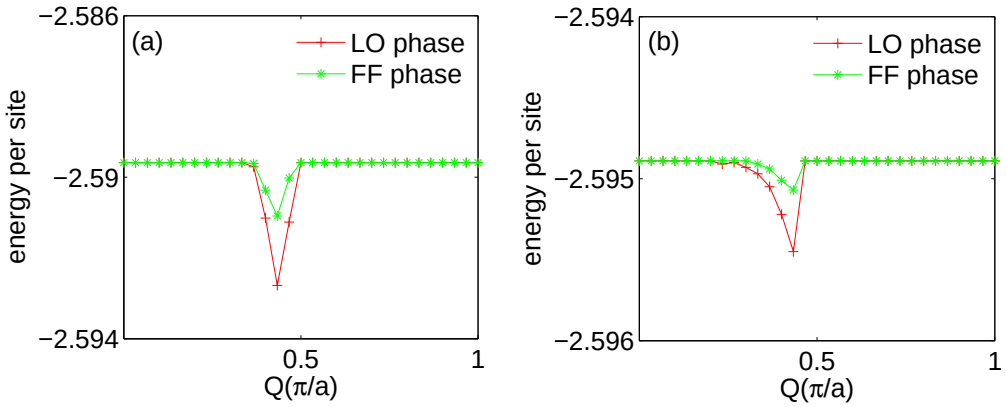

Figure 16: The energy per site of the FF phase (green) and the LO phase (red) as function of the pair wave vector Q for transverse hopping (a) $t^{\perp} = 0.05$ and (b) $t^{\perp} = 0.1$. For each Q, the Δ is determined self-consistently. Energy at $-Q$ is the same as that at Q.

where $k_x^n = 2\pi n/Na$ is the discrete momentum in the x direction. The components of α obey anticommutation relation $\{\hat{\alpha}^{\dagger(m_1)}_{k_y k_z}, \hat{\alpha}^{(m_2)}_{k_y k_z}\} = \delta_{m_1 m_2}$, where m_1, m_2 labels the corresponding operator component of α. The Hamiltonian takes the compact form

$$\hat{H}_{sp} = \sum_{k_y k_z} \hat{\alpha}^{\dagger}_{k_y k_z} \mathcal{H}_{k_y k_z} \hat{\alpha}_{k_y k_z} + \sum_{\mathbf{k}} \xi^p_{\mathbf{k}} - \frac{(1+\delta_{Q,-Q})N^3\Delta^2}{2U_{sp}}. \tag{6.18}$$

Since $\mathcal{H}_{k_y k_z}$ is real and symmetric, it can be diagonalized by an orthogonal transformation $\hat{\alpha}_{k_y k_z} = \mathcal{D}_{k_y k_z} \hat{\beta}_{k_y k_z}$ to yield $2N$ eigenvalues $E^l_{k_y k_z}$. Here $\mathcal{D}_{k_y k_z}$ is an orthogonal matrix that makes $\mathcal{D}^{-1}_{k_y k_z} \mathcal{H}_{k_y k_z} \mathcal{D}_{k_y k_z}$ diagonalized. The new operators $\hat{\beta}_{k_y k_z}$ automatically obey the fermionic anticommutation relationship $\{\hat{\beta}^{\dagger(m_1)}_{k_y k_z}, \hat{\beta}^{(m_2)}_{k_y k_z}\} = \delta_{m_1 m_2}$. We get the ground state energy,

$$\begin{aligned} \langle \hat{H}_{sp} \rangle &= \sum_{k_y, k_z} \sum_{l=1}^{2N} E^l_{k_y k_z} \Theta(-E^l_{k_y k_z}) + \sum_{\mathbf{k}} \xi^p_{\mathbf{k}} \\ &\quad - \frac{N^3\Delta^2}{2U_{sp}}(1+\delta_{-Q,Q}), \end{aligned} \tag{6.19}$$

and the gap equation,

$$\Delta = \frac{2U_{sp}}{N^3(1+\delta_{-Q,Q})} \sum_{\mathbf{k}} \sum_{l} \mathcal{D}^{m_1,l}_{k_y k_z} \mathcal{D}^{m_1',l}_{k_y k_z} \Theta(E^l_{k_y k_z}). \tag{6.20}$$

Here, l labels the eigenenergy, and m_1, m_1' labels the matrix elements corresponding to the original S, P operators in the gap equation.

The parameters used in the mean-field calculations are the same as in the 1D case with small $t^\perp$'s added, and we still expect that the order parameter has the momentum around $0.435\pi/a$ as before. In our calculation, we test all the possible Q's, and for each Q we self-consistently solve for Δ and get the energy. Afterward, we compare the energies for all the Q's, and the minimum one is the true ground state. We choose $N = 60$ the same as before, which means the quasi-one-dimensional optical lattice has $N^3 = 60^3$ lattice sites. In the case $t^\perp = 0.05$, the ground state is the cosine wave phase with $Q = 0.433\pi/a$ and $\Delta = 0.822$. The ground state energy per site is -2.5927, lower than the noninteracting value -2.5896. When $t^\perp = 0.1$, the ground state is also the cosine wave phase with $Q = 0.433\pi/a$ and $\Delta = 0.542$. The ground state energy per site is -2.5955, lower than the noninteracting value -2.5949. Fig. 16 shows the calculated energy for different Q's (Q has discretized values on a finite size lattice) and transverse hoppings, and we can see that the LO phase has lower energy than FF phase. These results confirm that (i) the cosine wave state has lower energy than the exponential wave state, (ii) the order parameter has the momentum close to the prediction of Eq. (6.5), and (iii) larger transverse hopping tends to destroy the p-orbital pair condensate, which is indicated by the fact that the energy gain for larger transverse hopping is smaller than for smaller transverse hopping.

An interesting feature of the p-orbital pair condensate in quasi-one-dimensional is the possible existence of Fermi surfaces with gapless energy spectrum. We monitor the fermion occupation numbers, i.e. $\langle \hat{S}^\dagger_{\mathbf{k}} \hat{S}_{\mathbf{k}} \rangle$ and $\langle \hat{P}^\dagger_{\mathbf{k}} \hat{P}_{\mathbf{k}} \rangle$ for increasing transverse hopping. The results are shown in Fig. 17. For the small $t^\perp$, they take the usual BCS form and vary continuously from 1 (red) to 0 (blue) across the bare free Fermi surfaces (the black dashed curves), as shown in Figs. 17(a) and (c) for $t^\perp = 0.05$. One can see that the color near Fermi surfaces changes from red to blue continuously in both Figs. 17(a) and (c). For larger transverse hopping, sharp Fermi surfaces characterized by a sudden jump in $\langle \hat{S}^\dagger_{\mathbf{k}} \hat{S}_{\mathbf{k}} \rangle$ and $\langle \hat{P}^\dagger_{\mathbf{k}} \hat{P}_{\mathbf{k}} \rangle$ appear.

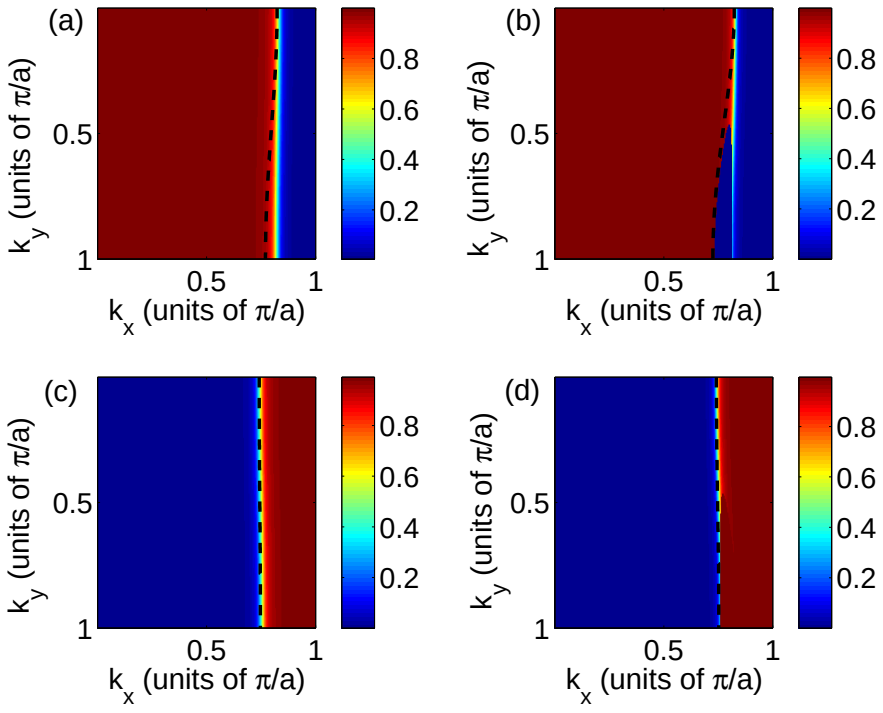

Figure 17: The occupation of s and p band within the paired state for different transverse hopping $t_\perp$. Only the first quadrant of the Brillouin zone in the $k_x - k_y$ plane is shown, $k_z = \pi/a$. The black dashed lines indicate the "bare" Fermi surfaces for corresponding noninteracting fermions ($U_{sp} = 0$). (a) $\langle \hat{S}^\dagger_{\mathbf{k}} \hat{S}_{\mathbf{k}} \rangle$ for $t^\perp = 0.05$; (b) $\langle \hat{S}^\dagger_{\mathbf{k}} \hat{S}_{\mathbf{k}} \rangle$ for $t^\perp = 0.1$; (c) $\langle \hat{P}^\dagger_{\mathbf{k}} \hat{P}_{\mathbf{k}} \rangle$ for $t^\perp = 0.05$; (d) $\langle \hat{P}^\dagger_{\mathbf{k}} \hat{P}_{\mathbf{k}} \rangle$ for $t^\perp = 0.1$.

This is clearly shown in Figs. 17(b) and (d) for $t^\perp = 0.1$ as the occupation number changes discontinuously from 1 (red) to 0 (blue). One can see that the color near Fermi surfaces changes from red to blue suddenly for k_y roughly in between 0.5 and 1 in both Figs. 17(b) and (d). It can be understood qualitatively as follows. As $t^\perp$ increases, the original Fermi surfaces acquire a larger curvature in the transverse directions and the pairing condition in Eq. (6.5) cannot be satisfied everywhere anymore. Therefore in some regions fermions are not paired and Fermi surfaces survive. One should also note that the calculation is based on the assumption that $t^\perp \ll t^\parallel$, which predicts that $\mathbf{Q}$ is in the parallel direction. This prediction should fail as $t^\perp$ increases beyond certain critical values.

6.5 PHASE DIAGRAM

Now, we systematically explore the phases of our system for general band filling and spin imbalance. Since we have s- and p- bands with different bandwidths, we introduce two dimensionless quantities for the chemical potentials μ_s and μ_p

$$\begin{aligned} \tilde{\mu}_s &= \frac{\mu_s}{2t_s} = \frac{\mu_s}{2}, \\ \tilde{\mu}_p &= \frac{\mu_p - \omega_b}{2t_p} = \frac{\mu_p - \omega_b}{16}. \end{aligned} \tag{6.21}$$

Thus, for a non-interacting system, $-1 < \tilde{\mu}_s, \tilde{\mu}_p < 1$ control the filling for the s and p-band fermions respectively. We then define the quantities

$$\begin{aligned} \mu &= \frac{\tilde{\mu}_s + \tilde{\mu}_p}{2}, \\ h &= \frac{\tilde{\mu}_s - \tilde{\mu}_p}{2}, \end{aligned} \tag{6.22}$$

as the parameters controlling the average filling and polarization in the phase diagram. The phase at $-\mu, -h$ is the same as the state at μ, h, since the transformation $\mu, h \to -\mu, -h$ gives $\mu_s, \mu_p \to -\mu_s, -\mu_p$, and the mean-field Hamiltonian with μ_s, μ_p is identical to Hamiltonian with $-\mu_s, -\mu_p$ via a particle-hole transformation up to a constant.

We have four possible phases in such a system as shown in Fig. 18. As before, we ignored the inert fully filled s band of spin $\uparrow$ fermions. We consider the p band of spin $\uparrow$ fermions and s band of spin $\downarrow$ fermions. When one of these two bands is empty and the other is filled, the pairing does not happen and we call it normal phase I (N1) as in Fig. 18(a). When one of these two bands is fully filled and the other is partially filled, the pairing also does not happen since the fully filled band is inert. We call it normal phase II (N2) as in Fig. 18(b). When both of them are partially filled, fermions near Fermi surfaces from the two bands will be paired and the system is in superfluid phases as shown in Figs. 18(c) and 18(d). In the superfluid regime, when h is small, the pairing momentum prefers $Q = \pi/a$ and we call it commensurate p-orbital pair condensate (CpPC). It is a special case of the p-orbital pair condensate, where the occupation numbers of s-band spin $\downarrow$ fermions and p-band spin $\uparrow$ fermions are the same. It is similar to the conventional unpolarized pairing (BCS), where the

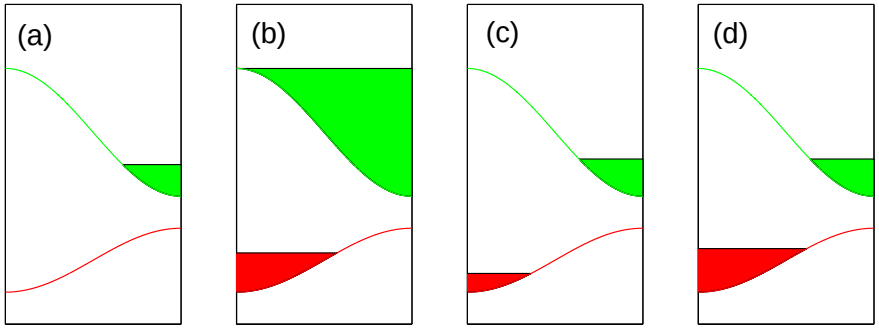

Figure 18: Band occupation for the four possible phases in the system. The band colored in red represents the s band occupied by spin $\downarrow$ fermions and the band colored in green represents the p band occupied by $\uparrow$ fermions. The spin $\uparrow$ fermions in the s band are not shown since they are inert. (a) Normal phase I (N1) with one band empty and the other partially filled. Here we only show the case with s band empty. We can also have the case with p band empty, which is not shown. (b) Normal phase II (N2) with one band fully filled and the other partially filled. Here we only show the case with p band full. We can also have the case with s band full, which is not shown. (c) Commensurate p-orbital pair condensate (CpPC) with both bands partially filled. The occupation numbers are the same. (d) Incommensurate p-orbital pair condensate (IpPC) with both bands partially filled. The occupation numbers are different.

spin $\uparrow$ fermions and spin $\downarrow$ fermions have the same population. However, in BCS pairing the CMM of the pair has the property $Q = 0$, while here $Q = \pi/a$. To understand the momentum π/a preference, note that in conventional BCS case, the two species of fermions have the same energy spectrum and the pairing is between two fermions with opposite momenta, which leads to the CMM of pair $Q = 0$. Here, the structure of energy spectrum of p band is different from s band. The equal occupation numbers mean $k_{F\uparrow} = \pi/a - k_{F\downarrow}$, which gives rise to $Q = k_{F\uparrow} + k_{F\downarrow} = \pi/a$, as shown in Fig. 18(c). At last, when h is large, the pairing momentum stays at a general $Q \approx k_{F\uparrow} + k_{F\downarrow}$ and the occupation number for the two species of fermions differ. We call it incommensurate p-orbital pair condensate (IpPC) as shown in

Fig. 18(d).

To determine the phases, we minimize the energy as a function of the pairing amplitude Δ and pairing momentum Q by mean-field analysis using the cosine wave function as outlined in the previous section. When the minimum is realized at $\Delta = 0$, it is normal phase. When Δ is finite, there are two possibilities. When $Q = \pi/a$, it is CpPC. When $Q \neq \pi/a$, it is IpPC. For the transition between superfluid and normal phase, and the transition between CpPC and IpPC, the behaviors of energy show that the phase transitions are first order in a lattice system. Between the superfluid and normal phases, near the phase transition, Δ changes suddenly from 0 to finite, and the energy shows two local minima at $\Delta = 0$ and $\Delta \neq 0$. Between CpPC and IpPC, the pairing momentum changes from $Q = \pi/a$ to $Q \neq \pi/a$ discontinuously, and the energy as a function of Q also has two local minima at $Q = \pi/a$ and $Q \neq \pi/a$. Thus, they are first-order phase transitions according to our mean field analysis. Therefore, we can determine the phase boundaries between normal phase and superfluid phase by monitoring Δ changing from zero to finite. We can also monitor Q changing from $Q = \pi/a$ to $Q \neq \pi/a$ to determine the phase boundaries between CpPC and IpPC.

In Fig. 19, we present a phase diagram for $t^{\perp} = 0.05$. An illustrative physical understanding about this phase diagram is as follows. In Fig. 19, when chemical potential difference h is small and the two bands are still partially filled to ensure the pairing, the system tends to stay in CpPC where $Q = \pi/a$. It is similar to the conventional BCS superfluid case. As h becomes larger, as long as the average filling μ is not too large or small and the two bands are still both partially filled, the pairing persists despite the spin imbalance and the system is in IpPC. If μ gets more and more negative, the average filling becomes smaller and smaller, and at certain μ, h, p band of spin $\uparrow$ fermions will be empty and the system will become N1 without pairing. Similarly, when μ is large and positive, the average filling is very high and at certain μ, h, the s band of spin $\downarrow$ fermions will be fully occupied, and the system becomes N2 without pairing. The almost straight phase boundaries in Fig. 19 between IpPC and normal phases indicate that these phase transitions are due to the change of band occupation as empty $\leftrightarrow$ partially filled $\leftrightarrow$ fully filled. In Fig. 19, the phase boundary between IpPC and N1 corresponds to the critical condition that the s band of spin $\downarrow$ fermions is partially filled while the p band of spin $\uparrow$ fermion becomes empty, and the almost straight

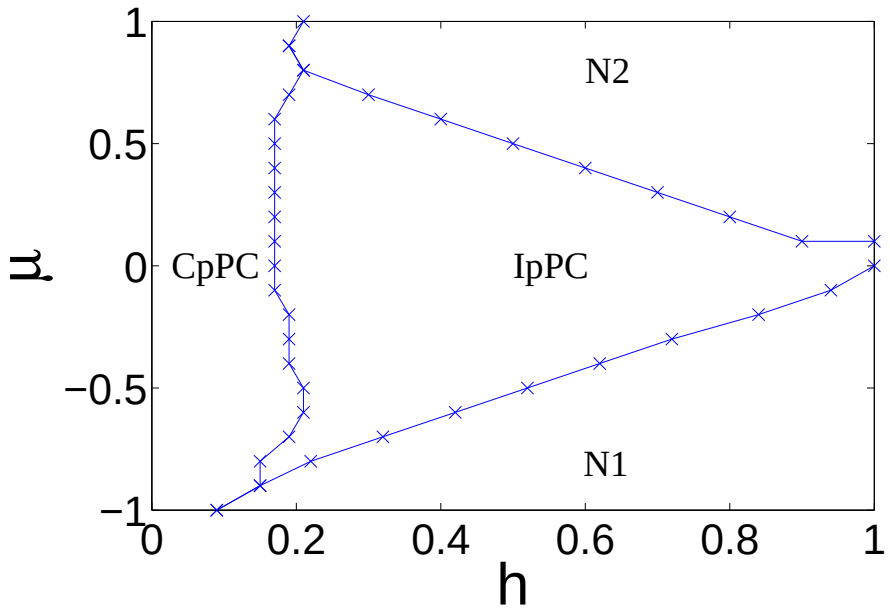

Figure 19: The phase diagram of the p-orbital pair condensate for $t^{\perp} = 0.05$. μ and h are defined in the main text. The crosses show the data points for the phase boundary obtained from the numerical procedure, and by connecting them we get the phase boundaries. CpPC: the s band of spin $\downarrow$ fermions and the p band of spin $\uparrow$ fermions have the same occupation numbers. IpPC: the s band of spin $\downarrow$ fermions and the p band of spin $\uparrow$ fermions have different occupation numbers. N1 with the p band of spin $\uparrow$ fermions empty and the s band of spin $\downarrow$ fermions partially filled. N2 with the p band of spin $\uparrow$ fermions partially filled and the s band of spin $\downarrow$ fermions fully filled.

phase boundary corresponds to the condition that $\tilde{\mu}_p = \mu - h = -1$ (but, as before, this is only an approximate argument due to the presence of interaction). Similarly, the almost straight phase boundary between IpPC and N2 corresponds to the condition that the s band of spin $\downarrow$ fermions becomes fully filled, while the p band of spin $\uparrow$ fermions is partially filled, or $\tilde{\mu}_s = \mu + h = 1$. All the phase transition lines in Fig. 19 are mean field results, and these straight lines are expected to be corrected by quantum critical fluctuations. The phase diagram shows that the p-orbital pair condensate happens in large parameter regimes and

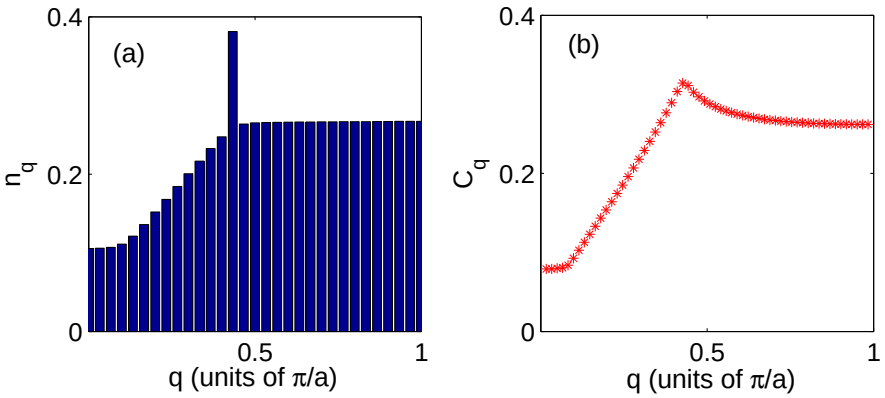

Figure 20: (a) The momentum distribution function n_q of projected molecules for a quasi-one-dimensional system with $t^{\perp} = 0.05$ (all other parameters are same as before) according to mean field theory. Here, $q = q_x$, $q_y = q_z = 0$. (b) Pair correlation function C_q for a 1D chain of $N = 60$ sites obtained by DMRG. The peak is located at $0.433\pi/a$ in both figures, which corresponds to the value $k_{F\uparrow} + k_{F\downarrow} = (N_s + N - N_p)\pi/Na$ for $N_s = 49$ and $N_p = 15$. The time-of-flight experiment is predicted to show the momentum peak at $0.433\pi/a$ in this case.

is closely related to the band and orbital properties in the optical lattice systems.

6.6 TIME-OF-FLIGHT EXPERIMENTS

The p-orbital pair condensate phase can inspire important experimental signatures for finite momentum condensation of bosonic molecules in higher orbital bands. By fast sweeping the magnetic field (and thus the interaction) from the BCS region to the deep BEC region across a Feshbach resonance [41, 42, 43, 44] as mentioned in Sec. 3.2, the BCS pairs are projected onto Feshbach molecules, which can be further probed for example by time-of-flight images [12]. The bosons produced effectively reside in p band and are stable, since by Pauli blocking the filled s-band fermions will prevent the the p-wave bosons from decaying [12]. Here, we use

a simple model [43, 44] to evaluate the momentum distribution of molecules after projection

$$n_{\mathbf{q}} = \sum_{\mathbf{k},\mathbf{k}'} f^*_{\mathbf{k}} f_{\mathbf{k}'} \langle \hat{S}^\dagger_{\mathbf{k}+\mathbf{q}/2} \hat{P}^\dagger_{-\mathbf{k}+\mathbf{q}/2} \hat{P}_{-\mathbf{k}'+\mathbf{q}/2} \hat{S}_{\mathbf{k}'+\mathbf{q}/2} \rangle, \tag{6.23}$$

where $f_{\mathbf{k}}$ is the molecular wave function, and the correlation function can be evaluated within mean field theory [44]. For fast sweeps, the molecular size is small compared to lattice constant, and the molecular wave function can be approximated by a delta function in real space (a constant $\sqrt{1/N}$ in momentum space). By this assumption, n_q is the same quantity as C_q in Eq. (6.6). Fig. 20(a) shows the n_q of p-wave Feshbach molecules and a peak is located at $0.433\pi/a$. Fig. 20(b) shows C_q from Eq. (6.6), based on the DMRG results shown in Fig. 15(b). The time-of-flight experiment is predicted to distribute peaks corresponding to that in Fig. 20. Note that for the 1D problem (Fig. 20(b)), the delta-function peak is replaced by a cusp characteristic of power law due to the lack of long range order, and there is no singularity in C_q.

7.0 ORBITAL DENSITY WAVES AND LIQUID CRYSTAL PHASES

In this chapter, we will study the interacting single-species p-orbital fermionic atoms in 2D square optical lattices with both attractive and repulsive interactions [36]. We find that the quasi-one-dimensional feature of the Fermi surfaces of the double degenerate p_x and p_y orbital bands gives rise to the following interesting orderings. For attractive interactions, it induces charge density wave (CDW) ordering in a wide filling regime where the superfluidity is greatly suppressed. For repulsive interactions, orbital density wave (ODW) ordering is induced. Both CDW and ODW show stripe or checkerboard patterns in space, depending on the filling. We further show that our system is a simple, clean, and highly tunable system to realize possible nematic and smectic liquid crystal phases, which is a topic of great current interest in correlated condensed matter physics [96, 97, 98, 99]. In this chapter, we will call the single-species fermions spinless fermions, as the commonly used terminology in cold atom context.

7.1 SYSTEM AND MODEL

Consider a system of spinless fermions with atomic mass m_a filled up to degenerate p_x and p_y orbital bands in a 2D square lattice. Such a system can be realized by considering an anisotropic 3D optical lattice with lattice potential $V_{\text{op}} = \sum_{\nu=x,y,z} V_\nu \sin^2(k_L r_\nu)$, where k_L is the wave vector of the laser beams and the lattice constant is $a = \pi/k_L$. By setting $V_z \gg V_x = V_y$, we realize dynamically decoupled 2D square lattice layers in xy plane, each being a 2D system. The 2D system is then filled with spinless fermions such that the lowest s band is fully occupied and two degenerate p_x and p_y orbital bands are partially filled.

In general, the band gap between s and p bands is much larger than the interaction, and the s-band fermions are dynamically inert. By expanding the fermionic field operators in Wannier basis and using tight-binding approximation, we obtain the p-band Fermi Hubbard model

$$\hat{H} = \sum_{\mathbf{r}\alpha\beta} t_{\alpha\beta}(\hat{C}^{\dagger}_{\alpha,\mathbf{r}+\mathbf{e}_\beta}\hat{C}_{\alpha,\mathbf{r}} + h.c.) - \mu\sum_{\mathbf{r}\alpha}\hat{n}_{\alpha,\mathbf{r}} + g\sum_{\mathbf{r}}\hat{n}_{x,\mathbf{r}}\hat{n}_{y,\mathbf{r}} \tag{7.1}$$

to describe the system with chemical potential μ. Eq. (7.1) only contains nearest-neighbor hopping and onsite interaction, since in typical ultracold atom experiments next-nearest-neighbor hopping and nearest-neighbor interaction are negligible. In Eq. (7.1), $\hat{C}_{\alpha,\mathbf{r}}$ is the annihilation operator of Wannier state p_α at site $\mathbf{r}$, and $\hat{n}_{\alpha,\mathbf{r}} = \hat{C}^{\dagger}_{\alpha,\mathbf{r}}\hat{C}_{\alpha,\mathbf{r}}$ is the number operator for p_α orbital state at site $\mathbf{r}$. The subscripts α and β run over x and y. The hopping term $t_{\alpha\beta}$ is given by $t_{\alpha\beta} = \left[t_\parallel\delta_{\alpha\beta} - t_\perp(1-\delta_{\alpha\beta})\right]$, where the parallel (transverse) hopping $t_\parallel$ ($t_\perp$) means the hopping of p_α orbital fermions at site $\mathbf{r}$ to the nearest neighbor $\mathbf{r}+\mathbf{e}_\beta$, with $\beta = \alpha$ ($\beta \neq \alpha$). Here, $\mathbf{e}_\alpha$ is the lattice unit vector in α direction. The last term is the onsite interaction between p_x and p_y orbital fermions induced by p-wave scattering, with g the coupling constant. In the harmonic approximation, a standard tight-binding calculation gives the transverse hopping $t_\perp = e^{-(\eta/2)^2}V_x/2$, and the parallel hopping $t_\parallel = |\eta^2/2 - 1|t_\perp$. The parameter $\eta = \alpha_x a$ is typically a large number ($\gg 1$) and therefore $t_\parallel \gg t_\perp$. Here, $\alpha_\nu = (V_\nu/E_R)^{1/4}k_L$, where we define a physical constant $E_R = \hbar^2k_L^2/2m$ named the recoil energy. The onsite interaction is given by $g = g_p\alpha_x^2\alpha_z(22\alpha_x^2+\alpha_z^2)/32(2\pi)^{3/2}$ in the pseudopotential approach with coupling constant g_p [85].

7.2 FERMI SURFACE INSTABILITIES

It is well known that nesting Fermi surfaces are crucial to realize some spontaneously translational-symmetry breaking phases [100], e.g., CDW, spin density wave (SDW), and FFLO. Here, nesting Fermi surfaces mean that for the fermionic pairs (particle-particle pair in the superconductive channel, and particle-hole pair in the density channel), there is a way to pair all the fermions near Fermi surfaces while keeping all the pairs have roughly the same center-of-mass momentum [100]. For the lowest s band in a 2D square lattice, the

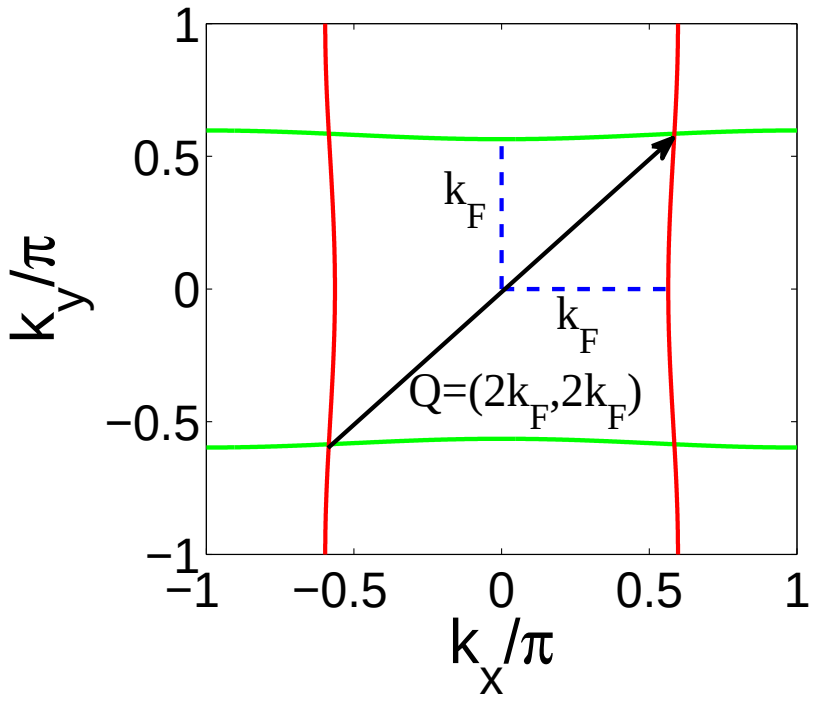

Figure 21: A schematic diagram illustrating how the $(2k_F, 2k_F)$ momentum of density fluctuation satisfies the nesting Fermi surface condition. Red (Green) solid curve: Fermi surfaces of p_x (p_y) orbital band. Blue dashed line: Fermi momenta of p_x and p_y orbital bands. Black solid arrow: the $(2k_F, 2k_F)$ momentum of density fluctuation simultaneously satisfying the nesting Fermi surface condition for both p_x and p_y orbital bands.

nesting Fermi surfaces for particle-hole pairs only occur at half filling assuming only nearest-neighbor hopping. In contrast, in our system the nesting of quasi-one-dimensional p_x and p_y Fermi surfaces as shown in Fig. 21 is independent of filling for a wide range of μ, as long as $t_\perp \ll t_\parallel$. In Fig. 21, p_x and p_y Fermi surfaces are perpendicular to each other, which greatly suppresses the Cooper instability from particle-particle channel scattering. The reason is that in order to induce Cooper instability, all the fermion pairs need to have almost the same CMM, which is impossible here with each particle-particle pair composed by one p_x and one p_y orbital fermions, given only onsite interaction in Eq. (7.1). In contrast, each p_x (p_y) particle-hole pair is composed by one particle and one hole within the p_x (p_y) orbital

band, which benefits from the nesting Fermi surface condition. To simultaneously satisfy the nesting Fermi surface condition for both p_x and p_y orbital bands in the density channel, the momentum of density fluctuation should be

$$\mathbf{Q_{1,2}} \approx (2k_F, \pm 2k_F), \tag{7.2}$$

as shown by the black arrow in Fig. 21, where k_F is Fermi momentum for each band.

To illustrate the above statement quantitatively, we study different instabilities in our system by random phase approximation (RPA) as follows. RPA is the summation of all the ring diagrams as a many-body approach, which is used to calculate the linear response to an external potential [52, 60], and it yields the same result as the response of a free particle system to the self-consistent field as a single-particle approach [101].

First we discuss the validity of RPA. Our system can be viewed as two sets of non-interacting 1D spinless Fermi chains perpendicular to each other, as one set in x-direction and the other in y-direction. The x-chains (y-chains) are weakly coupled by small transverse interchain hopping in the y (x) direction, and show quasi-one-dimensional Fermi surfaces (Fig. 21). The inter-orbital interaction between p_x and p_y fermions is then turned on, which couples the motion of particles in the x-direction and that in the y-direction.

In general, weakly coupled 1D Fermi chains with intrachain interaction cannot be studied by RPA [102] because of the Luttinger liquid behavior in such quasi-one-dimensional systems. The well defined (fermionic) single-particle excitations, which are required by RPA, are absent in Luttinger liquids.

To understand the difference between Luttinger liquid (1D) and Fermi liquid (2D and 3D), we consider the scattering process between two particles in different dimensions. An elastic scattering process in 1D between two particles with equal mass cannot change the momentum distribution of the two identical particles, because the particles are confined in one direction. This unique feature makes the excitations in 1D systems be collective, i.e., single-particle fermionic excitations are not well defined, and Landau's Fermi liquid description cannot apply [103]. In contrast, in a 2D or 3D system, the direction of the particles can be changed during the scattering, which leads to the change of the momentum distribution of the two particles. Single-particle fermionic excitations are well-defined in

this case, where the Landau Fermi-liquid theory can apply. RPA requires the validity of Landau's Fermi liquid description, or in other words, the well-defined single-particle fermionic excitations must present in the system. Therefore, RPA is valid in 2D or 3D, but not in 1D.

The key ingredient in our system is the existence of the inter-orbital interaction that couples p_x and p_y fermions, which is a 2D scattering process. The momentum distribution of the two scattering particles can be changed by such scattering process in our system. As a result, although our system appears to be composed of 1D chains of weak interchain tunneling, its dynamics is fundamentally 2D. As mentioned above, at high temperature, a 2D system is in a Fermi liquid phase with well defined single-particle fermionic excitations, where RPA is valid.

Notice that, the interspecies interaction also induces higher order effective intraspecies interactions. The induced intraspecies interaction is dynamically 1D, but they are much weaker since they are higher order processes. With the effect of the intraspecies interaction on the interspecies interaction neglected, for such a 2D system with one single dominant interspecies interaction, RPA is well justified [104].

For the density channel, we define the density operator $\hat{\rho}_{\alpha,q} = \sum_k \hat{C}^\dagger_{\alpha,k+q}\hat{C}_{\alpha,k}$ in momentum-Matsubara frequency space for p_α orbital band where $\alpha = x, y$. The 2+1 momenta k and q are defined as $k \equiv (\mathbf{k}, i\omega_m)$ and $q \equiv (\mathbf{q}, i\omega_n)$, where $\omega_m = (2m+1)\pi T$ and $\omega_n = 2n\pi T$ are fermionic and bosonic Matsubara frequencies. The density-density correlation function in our system without interaction has the form

$$\Pi^0_{\alpha\beta}(q) = \frac{T}{N^2}\langle\hat{\rho}_{\alpha,q}\hat{\rho}_{\beta,-q}\rangle^0 = -\frac{\delta_{\alpha\beta}}{N^2}\sum_{\mathbf{k}}\frac{n_F(\xi_{\alpha,\mathbf{k}}) - n_F(\xi_{\alpha,\mathbf{k}+\mathbf{q}})}{i\omega_n - \xi_{\alpha,\mathbf{k}+\mathbf{q}} + \xi_{\alpha,\mathbf{k}}}, \tag{7.3}$$

where $\langle ... \rangle^0$ means thermal average without interaction. The spectrum of p_x orbital fermions is $\xi_{x,\mathbf{k}} = 2t_\parallel \cos k_x - 2t_\perp \cos k_y - \mu$, and $\xi_{y,\mathbf{k}}$ has a similar form. The Fermi distribution function n_F is given by $n_F(\xi_k) = 1/(e^{\xi_k/T}+1)$. At $\mathbf{q} = \mathbf{Q} = (2k_F, \pm 2k_F)$, $t_\perp \to 0$ (perfect nesting) and $i\omega_n = 0$ (static limit), Eq. (7.3) reduces to

$$\chi^0 \equiv \Pi^0_{xx} = \Pi^0_{yy} \sim D(E_F)\ln\left(\frac{\omega_D}{k_B T}\right) \tag{7.4}$$

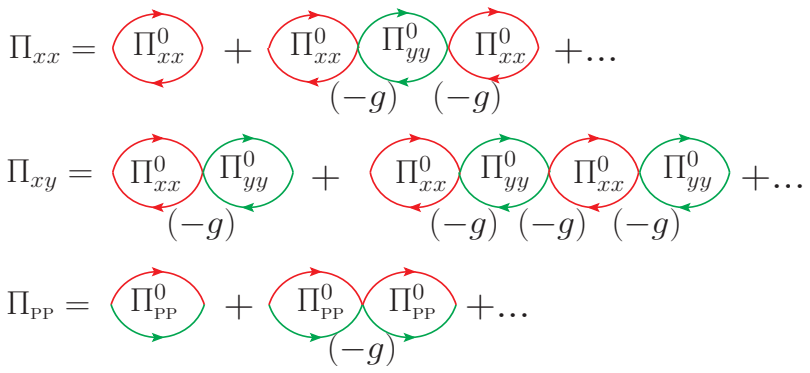

Figure 22: Feynman diagrams of density-density correlation functions of the same orbital band Π_{xx} and different orbital bands Π_{xy}, and the pair-pair correlation function $\Pi_{\rm PP}$. Red and green lines are the propagators of free p_x and p_y fermions.

in the continuous limit. In Eq. (7.4), $D(E_F)$ is the density of states at Fermi surface, which is approximately a constant for the whole Fermi surface in our p-band model, and ω_D is some energy cutoff.

When the interaction is turned on, the density-density correlation function $\Pi_{\alpha\beta}(q) = \frac{T}{N^2}\langle\hat{\rho}_{\alpha,q}\hat{\rho}_{\beta,-q}\rangle$ can be evaluated by RPA as shown in Fig. 22, where $\langle ...\rangle$ means thermal average with interaction. Here we assume the interaction g is the small parameter for the expansion. The reason for summarizing only the ring diagrams to infinite order in RPA is that these ring diagrams are most divergent to all orders. For Coulomb interaction, the justification of RPA is due to the $1/|\mathbf{q}|^2$ form of interaction in momentum space [52]. Here RPA is justified because each ring in Fig. 22 is a pair of Fermi propagators with divergence at $\mathbf{Q}$. Meanwhile, there are less such divergent pairs of Fermi propagators at $\mathbf{Q}$ in other types of diagrams. Therefore, RPA captures the most dominant (divergent) terms in our system.

We then evaluate the following correlation functions

$$\Pi_{\pm} = \frac{T}{N^2}\langle\hat{\rho}_{\pm}(q)\hat{\rho}_{\pm}(-q)\rangle, \tag{7.5}$$

where $\hat{\rho}_{\pm}(q) = \hat{\rho}_{x,q} \pm \hat{\rho}_{y,q}$ are the total density and density difference between p_x and p_y fermions, i.e., the CDW and ODW instability channels. Given that $t_\perp \to 0$, $\mathbf{q} = \mathbf{Q} = (2k_F, \pm 2k_F)$, and $i\omega_n = 0$, Eq. (7.5) reduces to

$$\Pi_{\pm} = \frac{2\chi^0}{1 \pm g\chi^0}. \tag{7.6}$$

Since $\chi^0 \sim D\ln\left(\frac{\omega_D}{T}\right)$, any arbitrarily small attractive (repulsive) interaction $g < 0$ ($g > 0$) can induce divergence of Π_+ (Π_-) at sufficiently low temperature. Such divergence indicates phase transition to the corresponding symmetry breaking phase.

In experiments, a small but finite $t_\perp$ is inevitable, which makes the Fermi surface nesting not perfect. Density waves do not exist even at $T = 0$ if the interaction is too small, since χ_0 is not guaranteed to diverge for non-perfect nesting even at $T = 0$. However, for a non-perfect nesting, the same density wave ordering is generally expected to exist if the interaction strength exceeds a certain critical value, i.e., if we increase g in Eq. (7.6). For example, even if the Fermi surfaces between spin up and down fermions are Zeeman split in the presence of a field, it is well known that the BCS superfluidity or superconductivity persists up to a critical Zeeman splitting for a given interaction strength. The latter is known as Chandrasekhar-Clogston limit [90, 91]. Increasing $|g|$ is experimentally feasible due to the high tunability of the interaction in optical lattices, e.g., by increasing the lattice potential.

Fig. 23 shows the phase transition temperatures from CDW instability evaluated by RPA with small transverse hoppings $t_\perp = 0, 0.04$, and 0.08. We set the system size to be $N^2 = 300^2$. The parallel hopping is set to be $t_\parallel = 1$ as the energy unit, and we choose the interaction strength $g = -2$. Here we choose a finite g which is not small, in order to obtain a relatively large phase transition temperature. It can be seen that although a small $t_\perp = 0.04$ weakens the (stripe) density wave ordering, at a finite interaction $g = -2$ the (stripe) density wave still occurs. However, a stronger $t_\perp = 0.08$ destroys the (stripe) density waves over a certain range of the effective chemical potential μ'. Here the effective chemical potential μ' includes the Hartree term correction to the original chemical potential μ, which can be solved numerically.

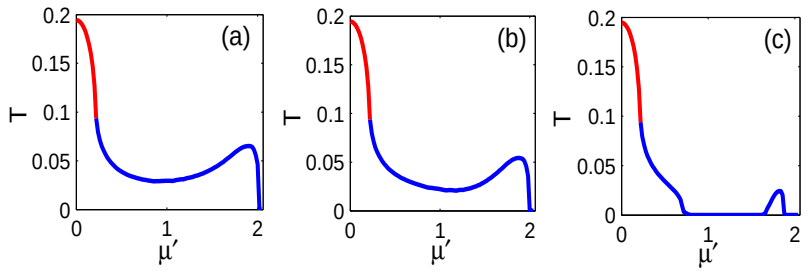

Figure 23: Phase transition temperature for CDW instability at $g = -2$ from RPA calculation. (a) $t_\perp = 0$. (b) $t_\perp = 0.04$. (c) $t_\perp = 0.08$. Red line: instability towards checkerboard density wave ordering. Blue line: instability towards stripe density wave ordering. The transition temperature towards checkerboard density wave ordering with the effective chemical potential (including Hartree term) μ' near 0 is much higher than that towards stripe density wave ordering with μ' away from 0, which indicates that the former is more experimentally feasible than the latter. This feature comes from the Umklapp process at half filling. Besides, the phase transition temperature towards checkerboard density wave ordering does not show any noticeable change as $t_\perp$ increases from 0 to 0.08, which suggests the checkerboard density wave ordering is not affected by $t_\perp$.

The particle-particle (Cooper) channel can be studied in a similar way by evaluating the correlation function of the pair operator $\hat{\Delta}_q = \sum_k \hat{C}_{x,-k+q}\hat{C}_{y,k}$. The pair-pair correlation function in our system without interaction reads

$$\Pi^0_{\text{PP}}(q) = \frac{T}{N^2}\langle\hat{\Delta}^\dagger_q\hat{\Delta}_q\rangle^0 = -\frac{1}{N^2}\sum_{\mathbf{k}}\frac{1-n_F(\xi_{x,-\mathbf{k}+\mathbf{q}})-n_F(\xi_{y,\mathbf{k}})}{i\omega_n-\xi_{x,-\mathbf{k}+\mathbf{q}}-\xi_{y,\mathbf{k}}}. \tag{7.7}$$

Recall that for the density-density correlation function without interaction, by choosing $\mathbf{q} = \mathbf{Q} = (2k_F, \pm 2k_F)$, Eq. (7.3) has logarithmic divergence as shown in Eq. (7.4). In contrast, no logarithmic divergence is found in Eq. (7.7) at any value of $\mathbf{q}$. Therefore, the pair-pair correlation with interaction

$$\Pi_{\text{PP}} = \frac{T}{N^2}\langle\hat{\Delta}^\dagger_q\hat{\Delta}_q\rangle = \frac{\Pi^0_{\text{PP}}(q)}{1+g\Pi^0_{\text{PP}}(q)} \tag{7.8}$$

evaluated by RPA as shown in Fig. 22 will not diverge at any temperature, different from the density-density correlation functions in Eq. (7.6). This means that the instability of the particle-particle channel is greatly suppressed, and there is no phase transition towards superconductivity.

7.3 MEAN FIELD THEORY AT $T = 0$

The above consideration only shows that phase transitions towards density waves can happen in our system. In order to find ground state properties, i.e., the order parameter, we apply a real space mean field analysis at $T = 0$ for both $g > 0$ and $g < 0$. The interaction part of the Hamiltonian Eq. (7.1) can be decoupled in the density channel such that

$$\sum_{\mathbf{r}} \hat{n}_{x,\mathbf{r}} \hat{n}_{y,\mathbf{r}} \approx \sum_{\mathbf{r}} (\hat{n}_{x,\mathbf{r}} M_{y,\mathbf{r}} + \hat{n}_{y,\mathbf{r}} M_{x,\mathbf{r}} - M_{x,\mathbf{r}} M_{y,\mathbf{r}}), \tag{7.9}$$

where $\langle \hat{n}_{\alpha,\mathbf{r}} \rangle = M_{\alpha,\mathbf{r}}$ is the self-consistent condition and $\langle ... \rangle$ means the expectation value of the ground state at $T = 0$. Terms of order $(\hat{n}_{x,\mathbf{r}} - \langle \hat{n}_{x,\mathbf{r}} \rangle)(\hat{n}_{y,\mathbf{r}} - \langle \hat{n}_{y,\mathbf{r}} \rangle)$ have been neglected. Eq. (7.1) reduces to

$$\hat{H}_{\text{MF}} = \sum_{\mathbf{r}\alpha\beta} t_{\alpha\beta} (\hat{C}^{\dagger}_{\alpha,\mathbf{r}+\mathbf{e}_\beta} \hat{C}_{\alpha,\mathbf{r}} + h.c.) - \mu \sum_{\mathbf{r}\alpha} \hat{n}_{\alpha,\mathbf{r}} + g \sum_{\mathbf{r}} (\hat{n}_{x,\mathbf{r}} M_{y,\mathbf{r}} + \hat{n}_{y,\mathbf{r}} M_{x,\mathbf{r}} - M_{x,\mathbf{r}} M_{y,\mathbf{r}}), \tag{7.10}$$

which is in quadratic form and can be solved self-consistently. We set the parameters the same as before in Sec. 7.2, with $t_\perp = 0$ to simplify the calculation. For attractive interaction $g = -2$, we find CDW ordering where the densities of p_x and p_y fermions are the same. When $\mu = 0$, the total density of the ground state exhibits a stripe pattern in real space as shown in Fig. 24(a), and the energy per site is -2.0295, lower than that of the homogeneous-density state -2.0282. Although the energy gain is not large, we have repeated the calculation several times with randomized initial condition, and consistently found the stripe pattern and the same ground state energy. When $\mu = -1$, the total density exhibits a checkerboard pattern as shown in Fig. 24(b), and the system is at half filling at this μ. In this case, the

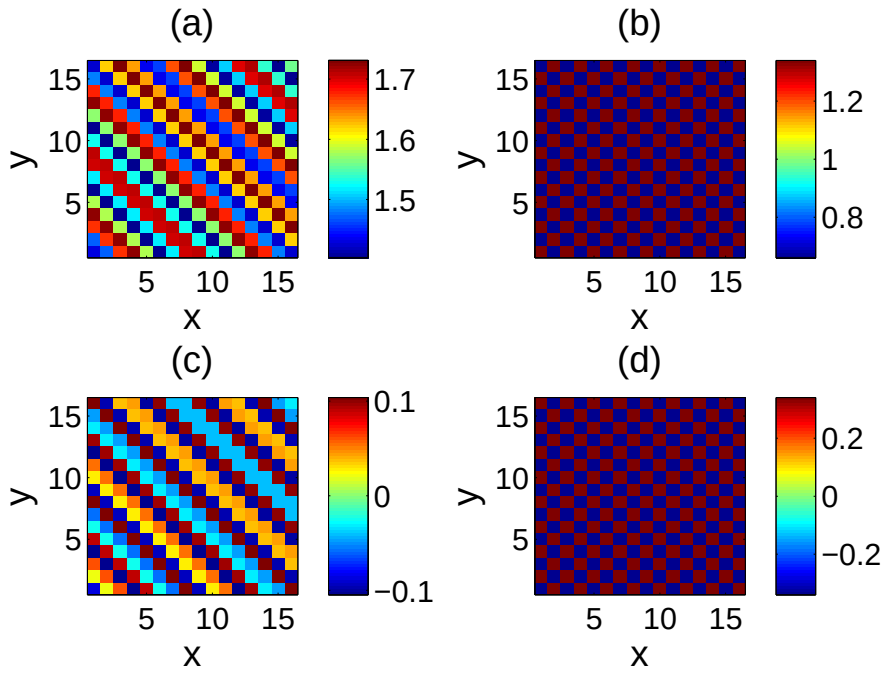

Figure 24: The density patterns in real space (showing 16×16 out of 300×300) obtained from real space mean field analysis. (a) The total density pattern with attractive interaction where $\mu = 0$. (b) The total density pattern with attractive interaction where $\mu = -1$. (c) The density difference pattern with repulsive interaction where $\mu = 0$. (d) The density difference pattern with repulsive interaction where $\mu = 1$.

ground state energy per site is -0.7826, lower than that of the homogeneous-density state -0.7731. Fourier series $M_{\alpha,\mathbf{r}} = a_0 + \sum_{n=1}^{\infty} [a_n \cos(n\mathbf{q}\cdot\mathbf{r}) + b_n \sin(n\mathbf{q}\cdot\mathbf{r})]$ are then used to fit Fig. 24(a) and (b). It can be seen that the chemical potential is modified to $\mu' = \mu - a_0 g$ by the background density a_0 (Hartree term), and the filling is determined by μ' instead of μ. We find $\mathbf{q} \approx (0.42\pi, 0.42\pi)$ by fitting Fig. 24(a). Higher order harmonics (the $n > 1$ Fourier components) are found non-vanishing in this case as expected in CDW, but are very weak compared to the first order terms ($a_n \ll a_1$, $b_n \ll b_1$, $n > 1$). The checkerboard pattern in Fig. 24(b) has momentum $\mathbf{q} = (\pi, \pi)$. The $\mathbf{q}$'s in both cases agree with Eq. (7.2) very well, with k_F determined by the effective chemical potential μ'.

For repulsive interaction $g = 2$, we find ODW ordering, where the densities of p_x and p_y orbital fermions are no longer the same, and the difference between them (ODW order parameter) oscillates in space. When $\mu = 0$ and $\mu = 1$, the density difference shows stripe and checkerboard patterns in Fig. 24(c) and (d), respectively. The Neel orbital ordering found in Ref. [85] at half filling and strong coupling limit $g \to +\infty$, where p_x and p_y Wannier orbitals alternate in space, can be understood as the extreme case of checkerboard ODW shown in Fig. 24(d), with density difference ± 1 alternating in space.

There are some general properties of the density wave ordering. (1) The checkerboard ordering at half filling has much higher transition temperature than the stripe ordering with other fillings due to the Umklapp process, which greatly enhances density waves at half filling [104]. (2) In general, increasing transverse hopping $t_\perp$ weakens the nesting Fermi surface condition and tends to destroy the stripe ordering. However, the checkerboard ordering at half filling is not affected by the Fermi surface curvature. It is because that a (π, π) momentum of checkerboard ordering always satisfies perfect nesting condition, independent of $t_\perp$ [104].

In experiments, a shallow harmonic trap $V(\mathbf{r})$ is present in addition to the optical lattice, and a spatial phase separation is expected due to the additional trapping potential [33]. With local density approximation $\mu(\mathbf{r}) \to \mu(\mathbf{r}) - V(\mathbf{r})$, a schematic phase diagram is shown in Fig. 25. At the center region of the trap where the local chemical potential is the highest, the stripe ordering exists due to large filling (region I). As one moves towards the edge of the trap, the filling decreases, and when the effective local chemical potential $\mu'(\mathbf{r}) \approx 0$, the checkerboard ordering appears and this region is at half filling (region II). As one moves towards the edge further, the filling becomes low and the stripe ordering emerges again (region III). Therefore, our theory predicts a spatial density profile of phase separation with stripe core $\to$ checkerboard shell $\to$ stripe edge. The phase coexistence here is due to the spatial varying trap potential, which modifies the local chemical potential. It is not the phase coexistence of degenerate ground states with domain walls separating different patterns. Therefore, the phase coexistence in Fig. 25 is stable.

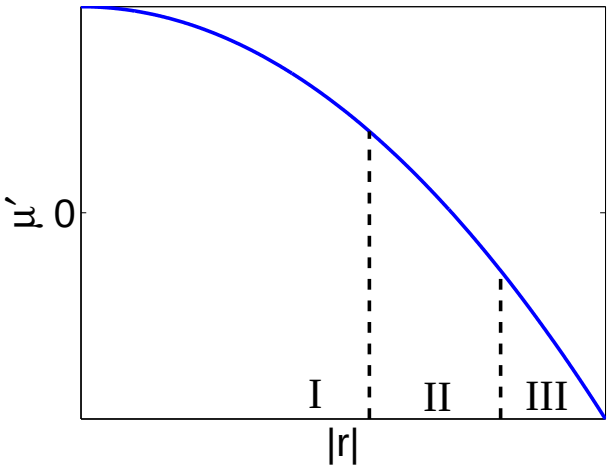

Figure 25: A schematic phase diagram in the presence of a trap with local density approximation. Here $|\mathbf{r}|$ is the distance from the center of the trap. I, II, and III are the regions of stripe, checkerboard, and stripe density waves, respectively.

7.4 LIQUID CRYSTAL PHASES AT $T \neq 0$

The above mean field analysis shows the existence of density wave ordering at $T = 0$. As one raises the temperature, thermal melting effect may drive the system to different nematic and smectic liquid crystal phases before it becomes normal Fermi liquid. Here the liquid crystal phases refer to the electronic liquid crystal phases [105], where the nematic and smectic liquid crystal phases here have the same symmetry breaking as the traditional definition of liquid crystal phases.

In this section, we will first define the liquid crystal phases in our system [105]. Afterward we will present a field theory which incorporates the thermal melting effect to study the liquid crystal phases in square lattice systems. Finally, we will comment on the advantages of our system to study liquid crystal phases.

For simplicity, we only consider liquid crystal phases from stripe CDW with attractive

interaction, where the densities of p_x and p_y orbital fermions are the same. The stripe CDW breaks the C_4 rotational symmetry of the square lattice down to C_2 (a Z_2 phase transition), and also breaks lattice translational symmetry, as shown in Fig. 24(a). As a result, two types of topological defects can occur at finite temperature: the Z_2 domain walls and the (edge) dislocations of stripes. The dislocations of stripes may drive the system to smectic or nematic liquid crystal phases. The smectic liquid crystal phase breaks both translational symmetry and C_4 rotational symmetry, which is essentially the same as the stripe order, while the nematic liquid crystal phase only breaks C_4 rotational symmetry and can be viewed as melted smectic stripes [105, 106].

The total density fluctuations associated with momenta $\mathbf{Q_{1,2}}$ can be parameterized as $\delta\rho = \left[\phi_1 e^{i\mathbf{Q_1}\cdot\mathbf{r}} + \phi_2 e^{i\mathbf{Q_2}\cdot\mathbf{r}} + c.c.\right]$. For the incommensurate case, by keeping only up to quartic terms, the effective action reads

$$S = \frac{1}{T}\int d^2r \ \sum_{\sigma=1,2}(j|\nabla\phi_\sigma|^2 + r|\phi_\sigma|^2 + u|\phi_\sigma|^4) + v|\phi_1|^2|\phi_2|^2 + S_t + ..., \tag{7.11}$$

where S_t denotes topological defects of stripe dislocations, similar to the vortex term in XY model. Eq. (7.11) is invariant under C_4 rotations of $\pi/2$, π, and $3\pi/2$, which yields $(\phi_1, \phi_2) \to (\phi_2^*, \phi_1)$, (ϕ_1^*, ϕ_2^*), and (ϕ_2, ϕ_1^*), respectively. Besides, Eq. (7.11) also has two U(1) symmetries, i.e., $\phi_{1,2} \to \phi_{1,2}e^{i\varphi_{1,2}}$, where φ_1 and φ_2 are arbitrary global phases.

The coupling constants j, r, u, v can be derived from the microscopic model Eq. (7.1) as shown in Appendix B. We have found $v = 4u$, which strongly suppresses the coexistence of ϕ_1 and ϕ_2. Without loss of generality, we assume ϕ_2 is suppressed, i.e., the saddle point is at $|\phi_1| = \Phi$ and $|\phi_2| = 0$, and write $\phi_1 = \Phi e^{i\varphi}$. Neglecting the gapped amplitude fluctuation of Φ, the low energy theory is described by φ as $S_\varphi = \frac{1}{T}\int d^2r \ j\Phi^2(\nabla\varphi)^2$, which reproduces the 2D XY model. A brief introduction of the 2D XY model is given in Appendix C.

The smectic and nematic order parameters can be defined as $\langle\phi_1 - \phi_2\rangle$ and $\langle|\phi_1|^2 - |\phi_2|^2\rangle$, respectively. At $T = 0$, $\langle\phi_1 - \phi_2\rangle \sim \langle\phi_1\rangle \sim \Phi e^{i\varphi_0} \neq 0$ with φ_0 an arbitrary global phase, and the system is smectic. The correlation function $\langle\phi_1(\mathbf{r})\phi_1(\mathbf{0})\rangle$ yields finite value as $|\mathbf{r}| \to \infty$. At arbitrary small temperature, the gapless U(1) mode of φ restores the translational symmetry, causing $\langle\phi_1\rangle = \langle\phi_2\rangle = 0$. The system is algebraic smectic, with algebraic order of ϕ_1. Here the algebraic order means the correlation function has a power law decay, i.e.,

$\langle\phi_1(\mathbf{r})\phi_1(\mathbf{0})\rangle \sim |\mathbf{r}|^{-\eta}$. As the temperature increases, the stiffness J defined as $J/2 \equiv j\Phi^2/T$ decreases from infinity according to microscopic calculation. When J reaches $2/\pi$, the system undergoes a Kosterlitz-Thouless transition and the algebraic order (the power law decay of the correlation function) of ϕ_1 is destroyed by proliferation of stripe dislocations, similar to the destroy of superfluidity by vortices in the XY model. The system becomes nematic with only short range correlation of ϕ_1, i.e., the correlation function exhibits exponential decay such that $\langle\phi_1(\mathbf{r})\phi_1(\mathbf{0})\rangle \sim e^{-|\mathbf{r}|/\xi}$ with ξ the correlation length. In this nematic phase, the C_4 rotational symmetry remains broken such that $\langle|\phi_1|^2 - |\phi_2|^2\rangle$ is still non-zero. Further increasing of temperature eventually drives a second order Ising-nematic phase transition (2D Ising universality class), above which the C_4 rotational symmetry is restored with $\langle|\phi_1|^2\rangle = \langle|\phi_2|^2\rangle$, and the system becomes normal. In 3D, the above analysis does not apply, since the fluctuation only reduces the strength of the density wave ordering in 3D, and we are not expecting liquid crystal phases from our model.

For the commensurate case with momentum $2k_F = 2\pi p'/p$, where p' and p are relatively prime integers, an additional term $w\cos(p\varphi)$ is allowed in Eq. (7.11). The U(1) symmetry of ϕ_1 is reduced to Z_p here, which means the action is invariant under translation $\varphi \to \varphi + 2\pi p''/p$, with non-negative integer $p'' < p$. With this additional cosine term, the action for φ naturally reduces to the Z_p compact clock model. According to the renormalization group analysis of the compact clock model as discussed in Appendix C, our system undergoes the smectic−nematic−normal transition as one increases the temperature when $1 < p \leq 4$, and the smectic−algebraic smectic−nematic−normal transition when $p > 4$. As $p \to \infty$ where the system approaches incommensurate, the smectic−algebraic smectic phase transition temperature reduces to zero, which is consistent with the incommensurate case discussed before.

As a specific, non-trivial example to make connections between the field theory Eq. (7.11) and the microscopic model Eq. (7.1), a system with commensurate 1/5 filling ($p = 5$) is studied. We focus on the temperature regime near the Ising-nematic phase transition point, so that in Eq. (7.11) the approximation $\Phi^2 = -r/2u$ for the saddle point is applicable. In order to obtain the coefficients in Eq. (7.11) by the procedure in Appendix B, the chemical potential is adjusted to make the filling 1/5 ($k_F = 4/5\pi$), with CDW momentum $\mathbf{Q} = (8\pi/5, 8\pi/5)$. A

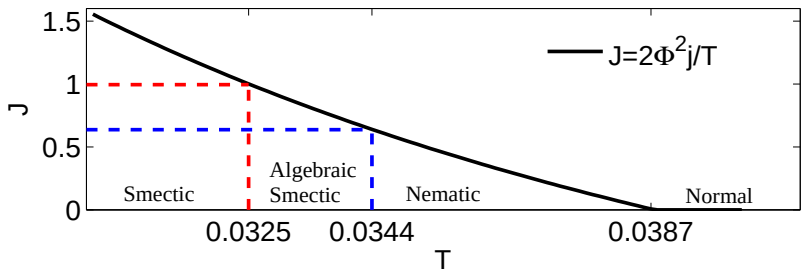

Figure 26: Phase diagram at 1/5 filling where $p = 5$. Red dashed line: determining the smectic−algebraic smectic phase transition temperature at $J = p^2/8\pi = 25/8\pi$. Blue dashed line: determining the algebraic smectic−nematic phase transition temperature at $J = 2/\pi$.

term $w\cos(5\varphi)$ produced by $(\phi_\alpha)^5 + c.c.$ also exists. In general w is small, because this term arises from higher order diagrams and is suppressed at finite temperature. The exact value of w is not important, but the existence of this term is crucial in the commensurate filling. After obtaining the coefficients r, j, u, v by Eq. (B.7), the phase transition temperature can be determined from the value of J according to the previous discussion. The phase diagram is shown in Fig. 26.

Our system has the following advantages to study liquid crystal phases. (1) There are no other competing orderings. A similar spinful condensed matter system was studied [107], which showed that a stripe CDW ordering of momentum $(2k_F, 2k_F)$ competes with a checkerboard CDW ordering of coexisting momenta $(2k_F, \pi)$ and $(\pi, 2k_F)$. This checkerboard ordering from interplay of $(2k_F, \pi)$ and $(\pi, 2k_F)$ orderings is different from the previous (π, π) checkerboard ordering in our system. Also, a similar spinful ultracold atomic system that has much more complicated interaction [108] may have many competing phases such as superconductivity, which is not as clean and simple as the proposed spinless system to study the liquid crystal phases. (2) The $2k_F$ momentum dependence of density wave ordering is highly tunable by changing the fillings, which makes it easy to adjust the commensurability.

7.5 EXPERIMENTAL REALIZATION

Our system can be realized by loading fermionic atoms such as ^{40}K or ^{6}Li of a single hyperfine state on square optical lattices. The fermions will automatically occupy p-orbital bands after the s band is fully filled. The interactions between spinless fermions can be tuned by p-wave Feshbach resonance, together with controlling the lattice spacing and potential depth. The cold gas is not required to be so close to the resonance, so the atom loss rate can be kept relatively low. The momenta of density waves $\mathbf{Q_{1,2}}$ can be detected by optical Bragg scattering [109]. Alternatively, *in-situ* imaging can directly show the density pattern $\delta\rho$. As discussed before, at half filling the checkerboard density waves are greatly enhanced by Umklapp process, and are not affected by the Fermi surface curvature caused by transverse hopping. Therefore, in experiments one should first search for the checkerboard density waves at half filling, which has the phase transition temperature $T_c \sim 0.2t_{\parallel}$ based on RPA (a mean-field-level estimate) as shown in Sec. 7.2, given that $|g/t_{\parallel}| = 2$. In addition, the hopping $t_{\parallel}$ of p-band fermions is in general an order of magnitude larger than the s-band hopping, which also enhances the phase transition temperature. With typical experimental parameters such that $\lambda \sim 500$ nm, $V_x \sim 5E_R$, and using ^{40}K, the estimated phase transition temperature for the checkerboard density waves at half filling is $T_c \sim 20$ nk.

8.0 ONE-DIMENSIONAL P-ORBITAL BOSONS IN OPTICAL LATTICES

Comparing with ultracold fermions, ultracold bosons are easier to study in both numerical and experimental aspects. The sign problem in quantum Monte Carlo methods, i.e. the unphysical negative probability appearing in the simulation due to the Fermi statistics, restricts the simulation scale of fermions [110]. At current experimental stage, people are still working hard on cooling fermions to quantum degeneracy regime. In contrast, bosonic systems are easy to simulate on computers and cool in experiments.

Bosons on higher orbital bands [88, 10] have been introducing great interest in recent years. Unlike fermions on higher orbital bands that can be stabilized by Pauli exclusion principle, bosons tends to occupy the lowest band to minimize the system energy, and therefore all the theoretical proposals [11, 12, 13, 14, 111, 37] regarding bosons on higher orbital bands are discussing meta-stable states of the system. There are two interesting features of bosons condensate on higher orbital bands. One is that induced by the onsite interaction, these condensate bosons may have complex ordering and form staggered angular momentum from site to site [88], similar as anti-ferromagnetism. Secondly, the bosons are condensed at finite momentum, because for example, p bands of square lattices have minima at the edge of the first Brillouin zone. In recent years, several experiments have been carried on to study this subject, and showing evidence of condensate bosons on higher orbital bands [16, 112, 17]. However, concrete experimental proof of the complex ordering has not been achieved yet.

In this chapter, we will discuss bosons loaded in p_x and p_y orbits of a 1D optical lattice with locally 2D isotropy at zero temperature [37], where the locally 2D isotropy means that at each lattice site the lattice potential is isotropic in x and y directions. We find two superfluid phases distinguished by an orbital order—an anti-ferro-orbital (AFO) superfluid and a para-orbital (PO) superfluid, and two Mott insulating phases—an AFO Mott and a p_x Mott

phase. The AFO order is characterized by ordering in the staggered orbital current $(p_x \pm ip_y)$ order [11, 12]. In the AFO superfluid phase, the inter-band phase difference is locked at $\pm\pi/2$ and the spontaneous AFO $(p_x \pm ip_y)$ order in this phase breaks the time reversal symmetry, whereas the fluctuations of the relative phase restore the time reversal symmetry in the PO superfluid phase. We also propose an experimental method to distinguish different phases by measuring momentum distribution, instead of directly measuring the local current flow resulting from time reversal symmetry breaking. The finite momentum peaks in the momentum distribution of the AFO superfluid phase make it distinguishable from the conventional 1D superfluid phases. In the AFO Mott phase the quantum noise measurement will be able to provide a concrete evidence of spontaneous time reversal symmetry breaking.

8.1 SYSTEM AND MODEL

We design the 1D system such that for each site, the local lattice potential is two-dimensionally isotropic. Consider a 2D lattice potential

$$V = V_x \sin^2(k_x x) + V_y \sin^2(k_y y), \tag{8.1}$$

where V_x, k_x (V_y, k_y) are the potential strength and wave vector of the laser beams in the x (y) direction. To make p_x and p_y orbitals locally degenerate, in harmonic approximation of tight-binding model, local isotropy requires

$$V_x k_x^2 = V_y k_y^2. \tag{8.2}$$

Meanwhile, we also want to make the system behave one-dimensionally, i.e, the hopping in y direction is much smaller than that in x direction. It can be realized by imposing a relatively larger laser strength and larger lattice constant in the y direction than those in the x direction, while satisfying Eq. (8.2). From Sec. 5.2, the ratio $t_x^{\parallel}/t_y^{\parallel}$ is estimated by

$$\frac{t_x^{\parallel}}{t_y^{\parallel}} = \frac{\alpha_x - 6}{\alpha_y - 6} e^{-\frac{1}{4}(\alpha_x - \alpha_y)} \tag{8.3}$$

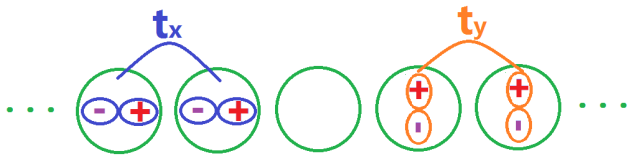

Figure 27: A schematic figure showing the parallel and transverse hoppings t_x and t_y in the 1D system along x direction. The green circles are used to denote the requirement of the approximate locally 2D isotropy of the lattice potential at each site.

with $\alpha_x = \pi^2\sqrt{V_x/E_{R,x}}$ and $\alpha_y = \pi^2\sqrt{V_y/E_{R,y}}$. The recoil energy $E_{R,x}$ is defined as $\hbar^2 k_x^2/2m_a$ and $E_{R,y}$ is defined in the same way. If we take $V_x/E_{R,x} = 6$, $V_y/E_{R,y} = 24$ and $a_y/a_x = \sqrt{2}$ ($k_y/k_x = 1/\sqrt{2}$, see Sec. 5.2), we get a locally isotropic system, while the hopping of p_y orbital in the y direction is smaller than one percent of the hopping of p_x orbital in the x direction. Therefore, the system is dynamically 1D.

In the rest of the chapter, we will work on the 1D system. The Hamiltonian describing bosons loaded on p_x and p_y orbits reads [12]

$$\begin{aligned} H &= \sum_{\langle jj'\rangle}\left[-t_x\hat{a}_x^\dagger(j)\hat{a}_x(j') - t_y\hat{a}_y^\dagger(j)\hat{a}_y(j')\right] - \sum_j \mu\hat{n}(j) \\ &\quad + \frac{U}{2}\sum_j\left[\hat{n}(j)\left(\hat{n}(j) - \frac{2}{3}\right) - \frac{1}{3}\hat{L}_z^2(j)\right]. \end{aligned} \tag{8.4}$$

Here $\hat{a}_x(j)$ ($\hat{a}_y(j)$) is the annihilation operator for p_x (p_y) orbital at site j. The discrete variable j labels the sites of the 1D chain, with the lattice constant a_x. The local particle number operator $\hat{n}(j)$ is defined as $\sum_{\alpha=x,y}\hat{a}_\alpha^\dagger(j)\hat{a}_\alpha(j)$, and the local angular momentum operator $\hat{L}_z(j)$ is defined as $-i\left[\hat{a}_x^\dagger(j)\hat{a}_y(j) - \hat{a}_y^\dagger(j)\hat{a}_x(j)\right]$. We have $U > 0$ as the repulsive Hubbard interaction. The average number of bosons per site is fixed by chemical potential μ. In Eq. (8.4), $t_x < 0$ is the longitudinal hopping of p_x bosons, and $t_y > 0$ is the transverse hopping of p_y bosons. Fig. 27 shows the hopping process of t_x and t_y. Due to anisotropy of the p-orbits, the longitudinal hopping of p_x-orbital fermions ("σ bond") is typically much

larger than the transverse hopping of p_y-orbital fermions ("π bond") [11, 13, 12]. In the following part, the ratio $|t_x/t_y|$ is taken as 9, which corresponds to $V_x \approx 6E_{R,x}$ (based on the estimation $|t_x/t_y| \approx \frac{1}{2}(\pi^2\sqrt{\frac{V_x}{E_{R,x}}} - 6)$ under harmonic approximation).

The presence of $\hat{L}_z^2$ is the key ingredient for the complex ordering, which comes from the term $\hat{a}_x^\dagger \hat{a}_x^\dagger \hat{a}_y \hat{a}_y + h.c.$ in Eq. (5.13). Such terms are forbidden for fermions by Pauli-exclusion principle, but are allowed for bosons. Intuitively, we consider a single-site problem with degenerate p_x and p_y orbitals, and ignore the hopping between sites for now. Suppose there are m particles at each site. This $\hat{L}_z^2$ term prefers m particles to condense at the single-particle state $\frac{a_x^\dagger \pm i a_y^\dagger}{\sqrt{2}}|0\rangle$, which yields the largest expectation value of $\hat{L}_z^2$ as m^2, i.e., the lowest energy in Eq. (8.4). In contrast, the energy gain of particles condensed at other single-particle state, such as $a_x^\dagger|0\rangle$, is smaller and not preferred with Eq. (8.4). For example, if we have $m = 2$ particles at each site, $\hat{L}_z^2$ has expectation value 4 in the former case compared to 2 in the latter case. When the hopping is turned on, the spatial configuration of alternating $\frac{a_x^\dagger + i a_y^\dagger}{\sqrt{2}}|0\rangle$ and $\frac{a_x^\dagger - i a_y^\dagger}{\sqrt{2}}|0\rangle$ is energetically favorable by the hopping term, and yields a staggered angular momentum or AFO pattern [88].

In Eq. (8.4), the hopping term has a U(1)×U(1) symmetry, which is given by $\hat{a}_\alpha(j) \to [e^{i\sigma_0\theta}e^{i\sigma_z\phi}]_{\alpha\beta}\hat{a}_\beta(j)$, with $\sigma_0 = \begin{bmatrix} 1 & 0 \\ 0 & 1 \end{bmatrix}$ and $\sigma_z = \begin{bmatrix} 1 & 0 \\ 0 & -1 \end{bmatrix}$. However the pair hopping term $\hat{a}_y^\dagger \hat{a}_y^\dagger \hat{a}_x \hat{a}_x$ from $\hat{L}_z^2$ does not conserve N_x and N_y separately, and thus breaks the U(1)×U(1) symmetry. Only the total particle number $N = N_x + N_y$ is conserved. The U(1)×U(1) symmetry is reduced to U(1)×Z_2 defined as $\hat{a}_\alpha(j) \to [e^{i\sigma_0\theta}e^{i\sigma_z\frac{\pi}{2}}]_{\alpha\beta}\hat{a}_\beta(j)$.

8.2 PHASE DIAGRAM FROM NUMERICAL CALCULATION

Numerical approaches using matrix product state such as the density matrix renormalization group [93] and the time-evolving block decimation [113, 114] can be implemented to study the ground state of 1D systems. Here the ground state is obtained by iterative optimization [93, 37]. The phase diagram is shown in Fig. 28. We will discuss the features of each phases in the rest of this section.

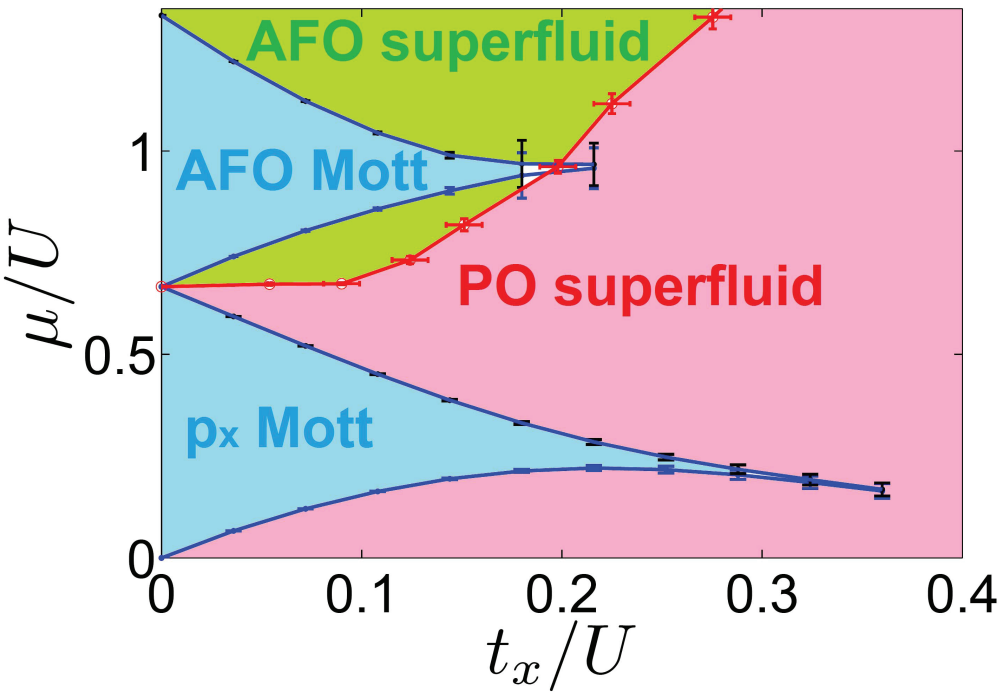

Figure 28: Phase diagram of a 1D lattice Bose gas with p_x and p_y orbital degrees of freedom. The lowest Mott lobe with filling $\nu = 1$ is dominated by p_x bosons. The Mott state with $\nu > 1$ has an AFO order (see text). We do not claim another phase for the tiny tip of the second Mott lobe beyond the red line because of numerical errors from the truncation in the matrix product state method. For sufficiently large hopping t_x or for low filling, the Bose gas has a crossover from a PO superfluid to a p_x superfluid phase, which will not be discussed here.

8.2.1 Mott Phases

Similar as the ordinary Bose-Hubbard model, for Mott phases in Fig. 28, the occupation number $\nu = \langle \hat{n}(j) \rangle$ at each site is integer. However, for each p_x and p_y orbitals, the occupation number is fractional. In Fig. 28, the p_x Mott phase corresponds to $\nu = 1$, which is similar to the ordinary Mott phase. The expectation value of the local angular momentum $\langle \hat{L}_z(j) \rangle$ is zero in this case. In contrast, the AFO Mott phase features a symmetry breaking of

U(1)×Z_2 to U(1), and the local angular momentum establish an staggered order $\langle \hat{L}_z(j) \rangle = (-1)^j |\langle \hat{L}_z(j) \rangle|$ or $(-1)^{j+1} |\langle \hat{L}_z(j) \rangle|$, corresponding to the two degenerate ground states from the broken Z_2 symmetry. We can thus define the order parameter as the Fourier transform of the local angular momentum that $\tilde{L}_z \equiv \frac{1}{L} \sum_j \langle e^{i\pi j} \hat{L}_z(j) \rangle$, which is finite in the AFO Mott phase and vanishes in the p_x Mott phase. Here L is the number of lattice sites. The time reversal symmetry is also broken in the AFO Mott phase since a finite $\hat{L}_z$ can be viewed as a finite local vortex-like current flow.

8.2.2 Superfluid Phases

By increasing the hopping magnitude, a phase transition from Mott insulator to superfluid occurs as discussed in Sec. 5.4. Here we find two different superfluid phases, where the AFO superfluid phase breaks the Z_2 symmetry and the other PO superfluid phase does not. The physical quantity characterizing the superfluid phase is the off-diagonal correlation function defined as $G_{\alpha\beta}(j, j') = \langle \hat{a}^\dagger_\alpha(j) \hat{a}_\beta(j') \rangle$. In a 3D superfluid this correlation function is finite when $|\mathbf{r}_j - \mathbf{r}_{j'}| \to \infty$ as the long range order. Here in the 1D superfluid at $T = 0$, the true long range order is absent, but a quasi-long-range order with power low decay still exists.

We first consider the AFO superfluid phase. The off-diagonal correlation functions are given by $G_{xx}(j, j') \sim e^{iQ(j-j')} |j - j'|^{-K/2}$, $G_{xy}(j, j') \sim i e^{iQj} |j - j'|^{-K/2}$ and $G_{yy}(j, j') \sim |j - j'|^{-K/2}$. The time reversal is broken in this phase, because the off-diagonal correlation $G_{xy}(j, j')$ is complex. The key feature is that the power law decay ($|j - j'|^{-K/2}$) correlations of G_{xx}, G_{xy}, and G_{yy} exhibit the same power exponent $K/2$.

Now we consider the PO superfluid phase. Here we have the off-diagonal correlation functions $G_{xx}(j, j') \sim e^{iQ(j-j')} |j - j'|^{-K_x/2}$, and $G_{yy}(j, j') \sim |j - j'|^{-K_y/2}$, while $G_{xy}(j, j')$ does not have such quasi-long-range order in this phase. We also have $K_x \ll K_y$ in this phase. Another difference of this PO superfluid phase from the AFO phase is that here the Z_2 symmetry is not broken.

8.3 QUANTUM PHASE TRANSITIONS FROM AFO TO PO SUPERFLUIDS

To understand the quantum phase transitions from AFO to PO superfluids, a low energy field theory can be used to describe the system. We use φ_x and φ_y to denote the phases of of the p_x and p_y superfluid components, and the Lagrangian describing the relative phase $\varphi_- = \varphi_x - \varphi_y$ is given by

$$\mathcal{L}[\varphi_-] = \frac{1}{2\pi K_-}\left[v_-^{-1}(\partial_\tau \varphi_-)^2 + v_-(\partial_x \varphi_-)^2\right] + m\cos(2\varphi_-), \tag{8.5}$$

where all the coefficients can be obtained from microscopic calculations. The ground state of this sine-Gordon model Eq. (8.5) depends on the magnitude of m. If m is greater than some critical value m_c, the cosine term is relevant in the sense of renormalization group, which means φ_- will choose $\pi/2$ or $3\pi/2$ (Z_2 symmetry breaking) to minimize Eq. (8.5). In other words, the relative phase between p_x and p_y superfluid components is locked and the system is at the AFO superfluid phase. On the other hand, if $m < m_c$, the cosine term becomes irrelevant and the φ_- is not locked to particular values. In other words, the Z_2 symmetry is restored in this case, and therefore the system is in the PO superfluid phase.

8.4 EXPERIMENTAL SIGNATURES

Due to the difference of the correlation functions of quantum phases discussed before, the time-of-flight imaging can be used to distinguish different phases. We first consider the two superfluid phases. From the orbital configuration as shown in Fig. 27, the non-interacting p_x bosons have p-band energy spectrum structure and tend to condense at momentum $k_x = \pm\pi/a$, while p_y bosons still have s-band energy spectrum structure and tend to condense at momentum $k_x = 0$. Therefore, in the superfluid regimes with interactions turned on, in the time-of-flight experiments we should check momentum peak near $k_x = \pi/a$ for the p_x bosons, and $k_x = 0$ for the p_y bosons. For the PO superfluid, the momentum distribution peak at $k_x = 0$ (p_y component) is weak and broad, while for the AFO superfluid, this peak

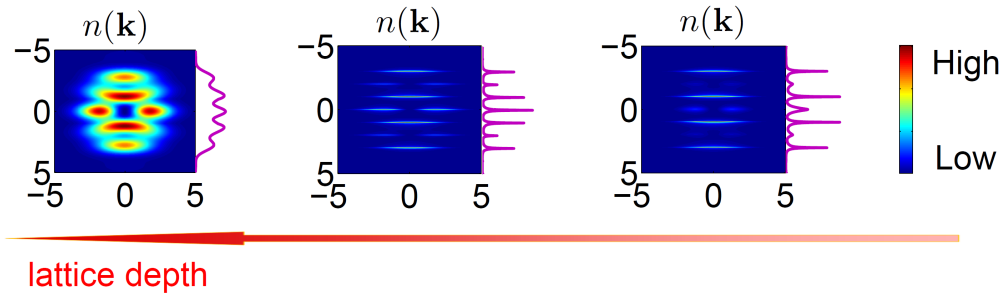

Figure 29: The schematic sketch of 2D momentum distributions $\tilde{n}(\mathbf{k})$ in different phases (PO superfluid, AFO superfluid and AFO Mott from right to left). In three subgraphs the horizontal (vertical) axis is $k_y a_y/\pi$ ($k_x a_x/\pi$). The purple wiggles along each subgraph shows $\tilde{n}_{1d}(k_x)$. In the AFO superfluid phase, the p_y peaks which are broad in PO SF, are replaced by sharp peaks. In the AFO Mott phase, there are no sharp peaks.

of p_y component is as strong and narrow as that of $k_x = \pm\pi/a$ peaks (p_x component). This feature comes from the fact that in the PO superfluid phase, the correlation of the p_y component decays much faster than p_x component, while in the AFO superfluid phase, the correlations of p_x and p_y components obey the same power law decay [37]. For the Mott phase, the condensate vanishes and the momentum peaks are smoothed out. A schematic sketch of 2D momentum distributions of different phases is shown in Fig. 29, as increasing lattice depth can enhance the onsite interaction, while it reduces the hopping, which means we should expect phase transitions from PO superfluid → AFO superfluid → Mott insulator, according to the phase diagram Fig. 28.

Inside Mott phases, we can use quantum noise measurement to determine whether it is a AFO or p_x Mott insulator. The AFO order in the Mott phase will have experimental signatures in the quantum noise measurement [115]. The quantum noise is defined as $C(\mathbf{d}) = \int d^2\mathbf{R} g(\mathbf{R}, \mathbf{d})$ with

$$g(\mathbf{R}, \mathbf{d}) = \langle n_{\text{tof}}(\mathbf{R} + \frac{1}{2}\mathbf{d}) n_{\text{tof}}(\mathbf{R} - \frac{1}{2}\mathbf{d})\rangle - \langle n_{\text{tof}}(\mathbf{R} + \frac{1}{2}\mathbf{d})\rangle \langle n_{\text{tof}}(\mathbf{R} - \frac{1}{2}\mathbf{d})\rangle,$$

where we have $\mathbf{R} = (R_x, R_y)$, $\mathbf{d} = (d_x, d_y)$. We can also understand $C(\mathbf{d})$ as the conditional probability of finding two particles separated by $\mathbf{d}$ with averaged over all such positions by integrating over $\mathbf{R}$. The brackets $\langle ... \rangle$ denote statistical averages of independently acquired time-of-flight images in experiments. For the Mott phases in our proposed 2D optical lattice, $g(\mathbf{R}, \mathbf{d})$ is given by

$$\begin{aligned} g(\mathbf{R}, \mathbf{d}) &= L \left\{ \sum_{\mathbf{K}} \delta^{(2)} \left(\frac{m_a}{\hbar t} \mathbf{d} - \mathbf{K} \right) \left(\zeta_{xx} n_x + \zeta_{yy} n_y \right)^2 \right. \\ &\quad \left. + \sum_{\mathbf{K}} \delta^{(2)} \left(\frac{m_a}{\hbar t} \mathbf{d} - \mathbf{K} + \mathbf{Q}_x + \mathbf{Q}_y \right) \left| \zeta_{xy} \mathcal{G}_{xy} + \zeta_{yx} \mathcal{G}_{xy}^* \right|^2 \right\}, \end{aligned} \tag{8.6}$$

where t is the time of flight. Here, $\mathcal{G}_{xy} = G_{xy}(0,0)$, $\zeta_{\alpha\beta} \sim (R_\alpha + \frac{1}{2} d_\alpha)(R_\beta - \frac{1}{2} d_\beta)$, $\mathbf{Q}_x = (\frac{\pi}{a_x}, 0)$, $\mathbf{Q}_y = (0, \frac{\pi}{a_y})$ and $\mathbf{K} = 2j_1 \mathbf{Q}_x + 2j_2 \mathbf{Q}_y$ (j_1 and j_2 are integers), where a_x and a_y are lattice constants along x and y directions.

In Eq. (8.6) the smooth Gaussian part of Wannier functions $\phi_\alpha(\mathbf{k})$ is approximated by a constant function, which is typical in quantum noise measurement [115]. The center of the trapped gas is taken as the origin of coordinates here. The sharp peaks of $C(\mathbf{d})$ at $\mathbf{d} = \mathbf{d}_0 \equiv \frac{\hbar t}{m_a} (\mathbf{K} - \mathbf{Q}_x - \mathbf{Q}_\mathbf{y})$ signify that the off-diagonal term $\mathcal{G}_{xy}$ is finite, which distinguishes the AFO Mott state from the p_x Mott. The experimental signature of an imaginary $\mathcal{G}_{xy}$ is predicted to be that $g(\mathbf{R}, \mathbf{d})$ exhibits nodal lines at $\mathbf{R} \parallel \mathbf{d}_0$. $\mathcal{G}_{xy}$ being imaginary indicates a local vortex-like current flow, which is a concrete evidence for the time reversal symmetry breaking.

9.0 CONCLUSION

In this concluding chapter, I will first summarize all the results from my graduate research. In Chapter 4 we discussed the damping phenomena of bulk Fermi gases in BCS-BEC crossover. We have found that the damping peak in the superfluid regime on the BCS side of the crossover is due to the coupling between the phonons of collective oscillations and thermally excited Bogoliubov quasi-fermions. Our results are compared quantitatively with the experiments, showing a good agreement. We also provide a general explanation to the damping phenomena discovered in other previous experiments. Such BCS-BEC crossover physics is quite unique in ultracold atomic physics and different from the traditional condensed matter physics, because it requires the tuning of the interaction using Feshbach resonance and the internal energy levels of the atom. Also, exciting collective modes of the trapped gases is experimentally feasible and widely used by releasing, contracting, or rotating the trap in ultracold quantum systems, which may be difficult to implement in materials.

In Chapter 6 we studied the ultracold fermionic atoms in a quasi-one-dimensional optical lattice system. We have presented our work of multi-band superconductivity induced from polarized fermions with one species occupied up to the p-orbital band and the other on s band in a quasi-one-dimensional optical lattice. We have found that, the formed Cooper pairs have center-of-mass momentum the sum of the two Fermi momenta, and have p-orbital center-of-mass motion. Ultracold quantum systems have the advantage to study the superconductive phases with finite center-of-mass momentum such as our p-orbital superconductivity or the FFLO phase, because a simple and clean quasi-one-dimensional lattice system can be easily engineered by laser beams [33], and such quasi-one-dimensional systems are shown to be very promising of sustaining FFLO states [79]. In condensed matter physics, in recent year people have found experimental signatures of FFLO phases in heavy fermion compound

$CeCoIn_5$ [73, 74, 116]. However, due to the complexity of the material, people are still trying to understand the physics there.

In Chapter 7 we studied the possible density wave orderings for single-species fermions on p-orbital bands in a 2D square optical lattice, and discussed the possible liquid crystal phases at finite temperature in such systems. Due to the quasi-one-dimensional structure of the Fermi surfaces, the density waves are robust and the wave vector of the density waves can be tuned by the fillings. Ultracold quantum systems provide an easier way to realize the platforms for such single-species fermionic problem.

In Chapter 8, we discussed a p-orbital bosonic system in 1D optical lattices with local isotropy. We have found that in such a system, the Mott insulator phase and the superfluid phase may break time reversal symmetry and induce anti-ferro-orbital patterns. The problem of bosonic particles with lattice potentials is also a unique feature of ultracold quantum gases, since in traditional material electrons are the elementary particles, and introducing bosons into the system seems not easy.

In my understanding, the most important feature of this new field of ultracold quantum gases focusing on many-body effects is that we can manipulate the spatial potential and inter-particle interaction in a relatively easy way to engineer the system we want. In other words, in the traditional condensed matter physics, nature provides us very rich and different kinds of materials. In ultracold atomic and molecular physics, human imagination allows us to utilize electric and magnetic fields, lasers, atoms and molecules to create numerous unconventional systems. Ultracold quantum systems can also be viewed as quantum simulators [117], i.e., highly controllable ultracold quantum systems that can be used to simulate the behavior of other complex quantum systems. For example, as a first step to simulate high T_c superconductors, people are working on realizing antiferromagnetism of the Fermi-Hubbard model in optical lattices. Ultracold quantum systems also provide very clean and highly controllable systems for testing fundamental theoretical concepts, e.g., the realization of BEC. Moreover, new physics which can only be realized in ultracold quantum gases so far is also developing, e.g., BCS-BEC crossover.

Finally, to conclude my graduate research, I have explored some physical problems such as damping phenomena in ultracold quantum systems, and also proposed some new ultracold

quantum systems to realize unconventional quantum phases.

APPENDIX A

FESHBACH RESONANCE

We will discuss Feshbach resonance in this appendix [118, 38, 64]. An effective two-channel Hamiltonian [119, 120] describing both the fermionic atomic and bosonic molecular contributions reads

$$\begin{aligned}\hat{H} &= \sum_{\mathbf{k},\sigma}(\epsilon^a_{\mathbf{k}}-\mu)\hat{a}^\dagger_{\mathbf{k},\sigma}\hat{a}_{\mathbf{k},\sigma}+\sum_{\mathbf{q}}(\epsilon^m_{\mathbf{q}}-2\mu+\nu)\hat{b}^\dagger_{\mathbf{q}}\hat{b}_{\mathbf{q}} \\ &\quad +g\sum_{\mathbf{q},\mathbf{k}}(\hat{b}^\dagger_{\mathbf{q}}\hat{a}_{\mathbf{k}+\mathbf{q}}\hat{a}_{-\mathbf{k}}+\hat{a}^\dagger_{-\mathbf{k}}\hat{a}^\dagger_{\mathbf{k}+\mathbf{q}}\hat{b}_{\mathbf{q}}),\end{aligned} \tag{A.1}$$

where we set the Planck constant $\hbar$, the volume V, and the Boltzmann constant k_B equal to unity here. In Eq. (A.1), $\epsilon^a_{\mathbf{k}} = \mathbf{k}^2/2m_a$ and $\epsilon^m_{\mathbf{q}} = \mathbf{q}^2/2m_m$ are the kinetic energy for fermionic atoms and bosonic molecules with masses $m_m = 2m_a$. The chemical potential is μ. We have ignored the bare fermionic interaction (background scattering) for now, since it is unessential for the resonance physics [118]. The detuning parameter $\nu = \mu_M(B - B_{\text{bare}})$ tells the energy difference between the bare closed channel (weakly bound state) and the bare open channel (free scattering state) in an external magnetic field. Here, B_{bare} is the bare resonance magnetic field at which the energies of the two bare channels are the same, where μ_M is the difference between the magnetic moments of the close and open channel.

Since we are interested in the scattering between fermions, we can write Eq. (A.1) in path integral form and integrate out the bosonic field [64]. The effective interaction between fermions becomes

$$V_{eff}(\mathbf{q}) = \frac{g^2}{i\omega_n - \epsilon^m_{\mathbf{q}} - 2\mu - \nu}. \tag{A.2}$$

Here $\omega_n = 2n\pi T$ is the bosonic Matsubara frequency with n integers.

The corresponding interaction U in the Hamiltonian form of a two-body scattering problem can be obtained by setting $T = 0$ and $\mu = 0$ in Eq. (A.2) as

$$U(\mathbf{q}) = \frac{g^2}{-\epsilon_{\mathbf{q}}^m - \nu}. \tag{A.3}$$

With such an interaction, the scattering length of two fermionic atoms in the low energy limit is [118]

$$\frac{m_a}{4\pi a} = \frac{1}{U_0} + \sum_{\mathbf{k}} \frac{1}{2\epsilon_{\mathbf{k}}^a}, \tag{A.4}$$

where we define

$$U_0 \equiv U(\mathbf{q} = 0) = -\frac{g^2}{\nu} = -\frac{g^2}{\mu_M(B - B_{\text{bare}})}. \tag{A.5}$$

The summation term in Eq. (A.4) needs an ultraviolet cutoff, since we are in the low energy limit. This cutoff is from that in our original Hamiltonian Eq. (A.1), we also need to set an ultraviolet cutoff for the Fermi-Bose coupling term, since it is unphysical to keep this coupling g a constant for large momentum.

Eq. (A.4) can be rewritten as

$$\frac{m_a}{4\pi a} = -\frac{\mu_M(B - B_{\text{bare}})}{g^2} + \sum_{\mathbf{k}} \frac{1}{2\epsilon_{\mathbf{k}}^a} \equiv -\frac{\mu_M(B - B_0)}{g^2}. \tag{A.6}$$

In Eq. (A.6),

$$B_0 = B_{\text{bare}} + \frac{g^2}{\mu_M} \sum_{\mathbf{k}} \frac{1}{2\epsilon_{\mathbf{k}}^a} \tag{A.7}$$

is the resonance magnetic field [118], which is shifted from the bare resonance B_{bare}. As a result, the scattering length will diverge and change sign when B reaches the resonance magnetic field B_0.

Eq. (A.4) provides a simple contact interaction U_0, which can be applied in a so-called single-channel model. In a single-channel model, only fermionic atoms are present and the interaction is simply the contact interaction U_0. Eq. (A.4) also provides the connection between this contact interaction U_0 and the scattering length a, which is also called a regularization procedure [23, 45]. It can be shown that the ultraviolet momentum cutoff we mentioned before can be safely extended to infinity, when we evaluate the gap equation of

the single-channel model [51]. The justification of this regularization procedure is discussed in Ref. [121].

To reproduce the resonance formula Eq. (2.23), an intuitive and simple way is to consider the background scattering length a_{bg} of the bare fermions. By adding this a_{bg} to Eq. (A.6), we get

$$a = a_{bg}\left(1 - \frac{\Delta_B}{B - B_0}\right), \tag{A.8}$$

with the resonance width $\Delta_B = \frac{m_a g^2}{4\pi a_{bg}\mu_M}$. More detailed and rigorous derivations of the scattering length are discussed in Ref. [122, 123].

As shown in Ref. [118], we can associate a length scale $r^* = \frac{1}{2m_a a_{bg}\mu_M \Delta_B}$. When $k_F r* \ll 1$ with k_F the Fermi momentum as defined in Sec. 3.2, it is a broad resonance. The above procedure reducing the two-channel model to a single-channel model can be applied in BCS-BEC crossover problem for broad resonance cases [118]. In most experiments, the system is in the broad resonance regime, where the single-channel model is applicable [123].

APPENDIX B

FIELD THEORY OF LIQUID CRYSTAL PHASES

To relate a fermionic microscopic Hamiltonian to a field theory of the order parameter, a general procedure is to introduce Hubbard-Stratonovich fields and then integrate out the fermionic field. This method is introduced in Ref. [60] to derive the theory of BCS order parameter in the fermionic superconductive problem. Here we follow this procedure to derive the theory for the density wave ordering. The Fermi Hubbard model Eq. (7.1) can be written in path integral form, where the partition function is given by e^{-S_F} and the effective action reads

$$\begin{aligned} S_F &= \int d\tau \sum_{\mathbf{r},\alpha} \psi^*_\alpha(\mathbf{r},\tau)(\partial_\tau - \mu)\psi_\alpha(\mathbf{r},\tau) + \sum_{\mathbf{r}\alpha\beta} t_{\alpha\beta}(\psi^*_\alpha(\mathbf{r}+\mathbf{e}_\beta,\tau)\psi_\alpha(\mathbf{r},\tau) + h.c.) \\ &\quad + g\sum_{\mathbf{r}} \psi^*_x(\mathbf{r},\tau)\psi^*_y(\mathbf{r},\tau)\psi_y(\mathbf{r},\tau)\psi_x(\mathbf{r},\tau). \end{aligned} \tag{B.1}$$

In Eq. (B.1), the interaction term can be rewritten as

$$\psi^*_x\psi^*_y\psi_y\psi_x = \frac{(\psi^*_x\psi_x + \psi^*_y\psi_y)^2 - (\psi^*_x\psi_x - \psi^*_y\psi_y)^2}{4}. \tag{B.2}$$

Consider two auxiliary Hubbard-Stratonovich fields $\int D(\rho_{1,2})e^{S_{\rho_{1,2}}}$, where we have $S_{\rho_{1,2}} = \int d\tau \frac{g}{4}\sum_{\mathbf{r}} \rho^2_{1,2}(\mathbf{r},\tau)$. By shifting $\rho_{1,2} \to \rho_{1,2} - (\psi^*_x\psi_x \pm \psi^*_y\psi_y)$, ρ_1 and ρ_2 denote total density field and density difference field, respectively. Multiplying $\int D(\rho_{1,2})e^{S_{\rho_{1,2}}}$ with shifted $\rho_{1,2}$ to e^{-S_F}, the quartic interaction between fermions in Eq. (B.2) is eliminated. According to the mean field analysis of CDW, the density difference has the mean field value zero. It

means we can ignore the density difference field ρ_2 in the CDW case here. As a result, the interaction term in Eq. (B.1) is replaced by

$$-\frac{g}{4}\int d\tau \sum_{\mathbf{r}} \rho_1^2 - 2\rho_1(\psi_x^*\psi_x + \psi_y^*\psi_y). \tag{B.3}$$

From mean field analysis, the total density ρ_1 is fluctuating around momenta $0, \pm\mathbf{Q_1}$, and $\pm\mathbf{Q_2}$. The fluctuation around zero momentum is the fluctuation of the average density, which tends to zero in thermodynamic limit. By ignoring such contribution, ρ_1 reduces to $\delta\rho$, which reproduces the total density fluctuation $\delta\rho$ around $\mathbf{Q_{1,2}}$. In the long wavelength limit, the density fluctuations around $\mathbf{Q_{1,2}}$ can be rewritten as

$$\delta\rho(\mathbf{r},\tau) = \frac{T}{N^2}\sum_{|\mathbf{q}|<\Lambda,\omega,\sigma} [\delta\rho_\sigma(\mathbf{Q}_\sigma+\mathbf{q},\omega)e^{i(\mathbf{Q}_\sigma+\mathbf{q})\cdot\mathbf{r}}e^{-i\omega\tau} + c.c.] \tag{B.4}$$

by Fourier transform, where Λ is some momentum cutoff of the long wavelength limit, and $\sigma = 1, 2$. Recall that the ϕ fields are defined through

$$\delta\rho(\mathbf{r},\tau) = \sum_\sigma \left[\phi_\sigma(\mathbf{r},\tau)e^{i\mathbf{Q}_\sigma\cdot\mathbf{r}} + c.c.\right]. \tag{B.5}$$

By Fourier transform

$$\phi_\sigma(\mathbf{r},\tau) = \tfrac{T}{N^2}\textstyle\sum_{|\mathbf{q}|<\Lambda,\omega} e^{i(\mathbf{q}\cdot\mathbf{r}-\omega\tau)}\phi_\sigma(\mathbf{q},\omega), \tag{B.6}$$

and comparing Eq. (B.4) with Eq. (B.5), we reach the relationship $\delta\rho(\mathbf{Q}_\sigma+\mathbf{q},\omega) = \phi_\sigma(\mathbf{q},\omega)$. The effective action is then written in momentum space, where $\delta\rho_\sigma$ can be replaced by ϕ_σ. Finally, the fermionic fields are integrated. The ϕ fields are kept up to quartic terms, and we reach the expression Eq. (7.11). The coefficients in Eq. (7.11) are

$$\begin{aligned}
r &= -\frac{g}{2T} - \frac{g^2}{4N^2T}\sum_{\mathbf{k}}\frac{1-2n_F(\xi_{\mathbf{k}})}{2\xi_{\mathbf{k}}},\\
j &= \frac{g^2}{16N^2T}\sum_{\mathbf{k}}\frac{\partial^2 n_F}{\partial\xi_{\mathbf{k}}^2}\frac{(t_\parallel\sin k_x)^2}{\xi_{\mathbf{k}}},\\
u &= \frac{g^4}{32N^2T}\sum_{\mathbf{k}}\left(\frac{1-2n_F}{4\xi_{\mathbf{k}}^3} + \frac{\partial n_F}{\partial\xi_{\mathbf{k}}}\frac{1}{2\xi_{\mathbf{k}}^2}\right),\\
v &= 4u,
\end{aligned} \tag{B.7}$$

in static limit. We do not consider quantum fluctuations in the present work. Here, $\xi_{\mathbf{k}}$ is the spectrum of free p_x orbital fermions.

APPENDIX C

THE 2D XY MODEL AND CLOCK MODEL

In this appendix we briefly introduce the 2D XY model and clock model. A full derivation that we follow in this appendix can be found in Ref. [124, 100], and here we only outline the procedure and present the results.

A classical XY model is defined as a classical spin model in a 2D square lattice with Hamiltonian [124]

$$H = -J \sum_{\langle ij \rangle} \mathbf{I}_i \cdot \mathbf{I}_j = -J \sum_{\langle ij \rangle} \cos(\theta_i - \theta_j), \tag{C.1}$$

where $\mathbf{I}_i = (\cos\theta_i, \sin\theta_i)$ is the unit 2D classical spin at lattice site i with position $\mathbf{R}_i$, and J is the coupling constant. Here $\langle ij \rangle$ indicates nearest-neighbor sites. As shown in Ref. [124], for this lattice model, at low temperature the correlation function has a power-law decay

$$\langle \mathbf{I}_i \cdot \mathbf{I}_j \rangle \sim |\mathbf{R}_i - \mathbf{R}_j|^{-T/2\pi J}, \tag{C.2}$$

where $\langle ... \rangle$ means the expectation value. At high temperature, the correlation function has an exponential decay

$$\langle \mathbf{I}_i \cdot \mathbf{I}_j \rangle \sim e^{-|\mathbf{R}_i - \mathbf{R}_j|/\xi}, \tag{C.3}$$

where ξ is the correlation length. We call the situation with power law decay the algebraic order, or quasi-long-range order, where the true long range order is absent. For the exponential decay, it is a disordered phase.

We are more interested in the continuum limit of Eq. (C.1). Assume that $\theta_i - \theta_j$ is small, i.e., the spin varies very smoothly in space, and expand Eq. (C.1) to second order. The Hamiltonian after switching from lattice summation to spatial integration is [124]

$$H = \frac{J}{2} \int d^2\mathbf{R} \left[\nabla\theta(\mathbf{R})\right]^2 . \tag{C.4}$$

In Eq. (C.4), we need to keep in mind that a short distance (large momentum) cutoff is inherent, which is the lattice constant in this case.

If we simply calculate the correlation function between θ from Eq. (C.4), at high temperature the correlation function is still power-law decay [100]. The reason is that the singularity contribution from the θ field [124] must be considered. As a result, we can write $\theta = \theta_r + \theta_s$, where the θ_r and θ_s are the regular and singular parts. For a vortex configuration, if θ_s has the value as the angle of $\mathbf{R} = (x, y)$ (the argument of the complex number $z = x + iy$ that $\theta_s = \arg(z)$), the Hamiltonian Eq. (C.4) yields

$$E_{\text{vortex}} = \frac{J}{2} \int_a^{R_c} dR\ 2\pi R \frac{1}{R^2} + E_{\text{core}} = \pi J \ln \frac{R_c}{a} + E_{\text{core}}, \tag{C.5}$$

where R_c measures the size of the system, and a is the lattice constant. The vortex core energy E_{core} is the energy for the $|\mathbf{R}| < a$ part of a vortex, which is a finite value compared with divergent $\ln R_c/a$ and will be ignored.

On the other hand, if only one of such vortices occurs in the system, the possibility of placing the vortex center in the 2D system is $\sim R_c^2/a^2$. Therefore, the entropy of a single vortex is

$$S_{\text{vortex}} = \ln \left(\frac{R_c}{a}\right)^2 = 2 \ln \frac{R_c}{a}. \tag{C.6}$$

From Eq. (C.5) and (C.6), we get the free energy of a single vortex

$$F_{\text{vortex}} = E - TS = (\pi J - 2T) \ln \frac{R_c}{a}. \tag{C.7}$$

In Eq. (C.7), if $\pi J > 2T$, a single vortex will cost free energy, which is not favored. The behavior of the system is then determined by the regular part θ_r, which yields a power-law decay of the correlation function [100]. In contrast, if $\pi J < 2T$, a single vortex will gain free energy, which is favored. The creations of such vortices will change the correlation function

to a short-range correlation, i.e., the system becomes disordered. Thus the phase transition temperature from this consideration is

$$T_c = \pi J/2. \tag{C.8}$$

However, the above argument is incomplete. It is possible that at low temperature, the vortices appear in pair with opposite winding numbers, i.e., two vortices with $\theta_s = \pm\arg(z)$ can appear simultaneously. Therefore, a more rigorous description is to apply a renormalization group (RG) study. For the RG method, there is a very classical introductory review article [104]. One can also refer to Ref. [60]. The basic idea of RG is to keep integrating out the fast fields sector (larger momentum) and renormalizing the theory of the remaining slower fields (smaller momentum). During this process, some terms in the Hamiltonian (or Lagrangian in a path-integral description) will become smaller and smaller, which means these terms are less and less important in the long wavelength limit. These terms are called irrelevant or marginal irrelevant, depending on how they become smaller in RG process. We also have marginal terms, which are unchanged in RG process. For the terms becomes larger and more important, we call them relevant or marginal relevant, depending on how they become larger in RG process.

To apply the RG study on the 2D XY model, a commonly used approach is to first map the 2D XY model with vortices to a 2D clock model without vortices (or sine-Gordon model, Potts model). We first rewrite Eq. (C.4) in the classical action form to incorporate the temperature and get [100]

$$S = \frac{J}{2T}\int d^2\mathbf{R}\,[\nabla\theta(\mathbf{R})]^2\,. \tag{C.9}$$

Meanwhile, we consider the following action for the clock model without vortices

$$S_{\text{clock}} = \int d^2\mathbf{R}\left[\frac{\kappa}{2}(\nabla\theta_c)^2 - g\cos(n\theta_c)\right], \tag{C.10}$$

which is called the non-compact clock model [100]. It can be shown that Eq. (C.10) is equivalent to the XY model Eq. (C.9) via the following connection. The κ is connected with J through the relation [100]

$$\frac{1}{2\pi\kappa} = \frac{2\pi J}{T}. \tag{C.11}$$

Therefore, the cosine term in the non-compact clock model Eq. (C.10) corresponds to the vortex contribution in the XY model Eq. (C.9), with n corresponding to the winding number of vortices that $z = n\arg(z)$. The factor g is related to the energy of vortex core.

It can be shown from RG analysis [100, 60] that for a small $g \to 0$ case, when $\kappa > n^2/8\pi$ ($\kappa < n^2/8\pi$), the g term is relevant (irrelevant), i.e., the cosine term will become more and more important (unimportant) in RG process. From Eq. (C.11), the corresponding XY model has the following property: when $J/T < 2/n^2\pi$ ($J/T > 2/n^2\pi$), the vortex contribution is relevant (irrelevant). Obviously the $n = 1$ yields the lowest phase transition temperature, i.e., $T_c = \pi J/2$, above (below) which the vortex contribution is relevant (irrelevant). Surprisingly, the T_c obtained from this RG process is the same as the result Eq. (C.8) from a simple free energy argument we discussed before.

We can extend the above discussion to the compact clock model, which allows vortex fluctuation of θ in Eq. (C.10). We know that the cosine term is relevant as $\kappa > n^2/8\pi$. We also know that given a XY model with $J/T \equiv \kappa$, the vortex contribution is relevant when $\kappa < 2/\pi$. Therefore, we have the following conclusion for the compact clock model.

(a) $n > 4$. For $\kappa > n^2/8\pi$, the cosine term is relevant and the vortex contribution is irrelevant, which means the ground state is determined by the cosine term. The ground state will choose a particular θ as a symmetry-breaking phase. For $\kappa < 2/\pi$, the cosine term is irrelevant and the vortex contribution is relevant, which means the ground state is determined by the vortex contribution, i.e., a disordered phase. For $2/\pi < \kappa < n^2/8\pi$, both cosine term and vortex contribution are irrelevant, which means the system is in algebraic order.

(b) $n = 4$. For $\kappa > 2/\pi$, the cosine term is relevant and the vortex contribution is irrelevant, where the system is in symmetry breaking phase. For $\kappa < 2/\pi$, the cosine term is irrelevant and the vortex contribution is relevant, where the system is in the disordered phase. There is no algebraic order in the system.

(c) $n < 4$. For $\kappa > 2/\pi$, the cosine term is relevant and the vortex contribution is irrelevant, where the system is in symmetry breaking phase. For $\kappa < n^2/8\pi$, the cosine term is irrelevant and the vortex contribution is relevant, where the system is in the disordered phase. However, for $n^2/8\pi < \kappa < 2/\pi$, both terms are relevant, and the phase transition in

this regime is described by Ginzburg-Landau theory [100].

BIBLIOGRAPHY

[1] M. Bartenstein, A. Altmeyer, S. Riedl, R. Geursen, S. Jochim, C. Chin, J. Hecker Denschlag, R. Grimm, A. Simoni, E. Tiesinga, C. J. Williams, and P. S. Julienne. Precise determination of ^{6}Li cold collision parameters by radio-frequency spectroscopy on weakly bound molecules. *Phys. Rev. Lett.*, 94:103201, Mar 2005.

[2] G. M. Bruun and H. Smith. Frequency and damping of the scissors mode of a fermi gas. *Phys. Rev. A*, 76:045602, Oct 2007.

[3] R.Grimm (private communication).

[4] M. J. Wright, S. Riedl, A. Altmeyer, C. Kohstall, E. R. Sánchez Guajardo, J. Hecker Denschlag, and R. Grimm. Finite-temperature collective dynamics of a fermi gas in the bec-bcs crossover. *Phys. Rev. Lett.*, 99:150403, Oct 2007.

[5] M. H. Anderson, J. R. Ensher, M. R. Matthews, C. E. Wieman, and E. A. Cornell. Observation of bose-einstein condensation in a dilute atomic vapor. *Science*, 269(5221):198–201, 1995.

[6] C. C. Bradley, C. A. Sackett, J. J. Tollett, and R. G. Hulet. Evidence of bose-einstein condensation in an atomic gas with attractive interactions. *Phys. Rev. Lett.*, 75:1687–1690, Aug 1995.

[7] K. B. Davis, M. O. Mewes, M. R. Andrews, N. J. van Druten, D. S. Durfee, D. M. Kurn, and W. Ketterle. Bose-einstein condensation in a gas of sodium atoms. *Phys. Rev. Lett.*, 75:3969–3973, Nov 1995.

[8] Markus Greiner, Olaf Mandel, Tilman Esslinger, Theodor W. Hansch, and Immanuel Bloch. Quantum phase transition from a superfluid to a mott insulator in a gas of ultracold atoms. *Nature*, 415(6867):39–44, January 2002.

[9] Toshiya Kinoshita, Trevor Wenger, and David S. Weiss. A quantum newton's cradle. *Nature*, 440(7086):900–903, April 2006.

[10] M. Lewenstein and W. Vincent Liu. Optical lattices: Orbital dance. *Nat. Phys.*, 7:101 – 103, 2011. and references therein.

[11] A. Isacsson and S. M. Girvin. Multiflavor bosonic hubbard models in the first excited bloch band of an optical lattice. *Phys. Rev. A*, 72:053604, Nov 2005.

[12] W. Vincent Liu and Congjun Wu. Atomic matter of nonzero-momentum bose-einstein condensation and orbital current order. *Phys. Rev. A*, 74(1):013607, Jul 2006.

[13] A. B. Kuklov. Unconventional strongly interacting bose-einstein condensates in optical lattices. *Phys. Rev. Lett.*, 97:110405, Sep 2006.

[14] Congjun Wu, W. Vincent Liu, Joel Moore, and Sankar Das Sarma. Quantum stripe ordering in optical lattices. *Phys. Rev. Lett.*, 97:190406, Nov 2006.

[15] Matthias Ölschläger, Georg Wirth, and Andreas Hemmerich. Unconventional superfluid order in the f band of a bipartite optical square lattice. *Phys. Rev. Lett.*, 106:015302, Jan 2011.

[16] Georg Wirth, Matthias Olschlager, and Andreas Hemmerich. Evidence for orbital superfluidity in the p-band of a bipartite optical square lattice. *Nat. Phys*, 7(2):147–153, February 2011.

[17] Parvis Soltan-Panahi, Dirk-Soren Luhmann, Julian Struck, Patrick Windpassinger, and Klaus Sengstock. Quantum phase transition to unconventional multi-orbital superfluidity in optical lattices. *Nat. Phys*, advance online publication:–, October 2011.

[18] B. DeMarco and D. S. Jin. Onset of fermi degeneracy in a trapped atomic gas. *Science*, 285(5434):1703–1706, 1999.

[19] K. M. O'Hara, S. L. Hemmer, M. E. Gehm, S. R. Granade, and J. E. Thomas. Observation of a strongly interacting degenerate fermi gas of atoms. *Science*, 298(5601):2179–2182, 2002.

[20] C. Chin, M. Bartenstein, A. Altmeyer, S. Riedl, S. Jochim, J. Hecker Denschlag, and R. Grimm. Observation of the pairing gap in a strongly interacting fermi gas. *Science*, 305(5687):1128–1130, 2004.

[21] M. Bartenstein, A. Altmeyer, S. Riedl, S. Jochim, C. Chin, J. Hecker Denschlag, and R. Grimm. Collective excitations of a degenerate gas at the bec-bcs crossover. *Phys. Rev. Lett.*, 92:203201, May 2004.

[22] J. Kinast, A. Turlapov, and J. E. Thomas. Damping of a unitary fermi gas. *Phys. Rev. Lett.*, 94:170404, May 2005.

[23] Stefano Giorgini, Lev P. Pitaevskii, and Sandro Stringari. Theory of ultracold atomic fermi gases. *Rev. Mod. Phys.*, 80:1215–1274, Oct 2008.

[24] M. W. Zwierlein, J. R. Abo-Shaeer, A. Schirotzek, C. H. Schunck, and W. Ketterle. Vortices and superfluidity in a strongly interacting fermi gas. *Nature*, 435(7045):1047–1051, June 2005.

[25] A. Altmeyer, S. Riedl, M. J. Wright, C. Kohstall, J. Hecker Denschlag, and R. Grimm. Dynamics of a strongly interacting fermi gas: The radial quadrupole mode. *Phys. Rev. A*, 76:033610, Sep 2007.

[26] Michael Köhl, Henning Moritz, Thilo Stöferle, Kenneth Günter, and Tilman Esslinger. Fermionic atoms in a three dimensional optical lattice: Observing fermi surfaces, dynamics, and interactions. *Phys. Rev. Lett.*, 94:080403, Mar 2005.

[27] Robert Jordens, Niels Strohmaier, Kenneth Gunter, Henning Moritz, and Tilman Esslinger. A mott insulator of fermionic atoms in an optical lattice. *Nature*, 455(7210):204–207, September 2008.

[28] U. Schneider, L. Hackermller, S. Will, Th. Best, I. Bloch, T. A. Costi, R. W. Helmes, D. Rasch, and A. Rosch. Metallic and insulating phases of repulsively interacting fermions in a 3d optical lattice. *Science*, 322(5907):1520–1525, 2008.

[29] Thereza Paiva, Yen Lee Loh, Mohit Randeria, Richard T. Scalettar, and Nandini Trivedi. Fermions in 3d optical lattices: Cooling protocol to obtain antiferromagnetism. *Phys. Rev. Lett.*, 107:086401, Aug 2011.

[30] Xin Wang, Qi Zhou, and S. Das Sarma. Mott-insulating phases and magnetism of fermions in a double-well optical lattice. *Phys. Rev. A*, 84:061603, Dec 2011.

[31] Peter Fulde and Richard A. Ferrell. Superconductivity in a strong spin-exchange field. *Phys. Rev.*, 135(3A):A550–A563, Aug 1964.

[32] A. I. Larkin and Y. N. Ovchinnikov, Zh. Eksp. Teor. Fiz. **47**, 1136 (1964) [Sov. Phys. JETP **20**, 762 (1965)].

[33] Yean-an Liao, Ann Sophie C. Rittner, Tobias Paprotta, Wenhui Li, Guthrie B. Partridge, Randall G. Hulet, Stefan K. Baur, and Erich J. Mueller. Spin-imbalance in a one-dimensional fermi gas. *Nature*, 467(7315):567–569, September 2010.

[34] Zixu Zhang and W. Vincent Liu. Finite-temperature damping of collective modes of a bcs-bec crossover superfluid. *Phys. Rev. A*, 83:023617, Feb 2011.

[35] Zixu Zhang, Hsiang-Hsuan Hung, Chiu Man Ho, Erhai Zhao, and W. Vincent Liu. Modulated pair condensate of p-orbital ultracold fermions. *Phys. Rev. A*, 82(3):033610, Sep 2010.

[36] Zixu Zhang, Xiaopeng Li, and W. Vincent Liu. Stripe, checkerboard, and liquid-crystal ordering from anisotropic p-orbital fermi surfaces in optical lattices. *Phys. Rev. A*, 85:053606, May 2012.

[37] Xiaopeng Li, Zixu Zhang, and W. Vincent Liu. Time-reversal symmetry breaking of p-orbital bosons in a one-dimensional optical lattice. *Phys. Rev. Lett.*, 108:175302, Apr 2012.

[38] Christopher J Pethick and Henrik Smith. *Bose-Einstein Condensation in Dilute Gases; 2nd ed.* Cambridge Univ. Press, Cambridge, 2008.

[39] Kerson Huang and C. N. Yang. Quantum-mechanical many-body problem with hard-sphere interaction. *Phys. Rev.*, 105:767–775, Feb 1957.

[40] R. Grimm. Ultracold Fermi gases in the BEC-BCS crossover: a review from the Innsbruck perspective. *ArXiv:0703091*, March 2007.

[41] C. A. Regal, M. Greiner, and D. S. Jin. Observation of resonance condensation of fermionic atom pairs. *Phys. Rev. Lett.*, 92:040403, Jan 2004.

[42] M. W. Zwierlein, C. A. Stan, C. H. Schunck, S. M. F. Raupach, A. J. Kerman, and W. Ketterle. Condensation of pairs of fermionic atoms near a feshbach resonance. *Phys. Rev. Lett.*, 92:120403, Mar 2004.

[43] Roberto B. Diener and Tin-Lun Ho. Projecting fermion pair condensates into molecular condensates. *arXiv:0404517*, 2004.

[44] Ehud Altman and Ashvin Vishwanath. Dynamic projection on feshbach molecules: A probe of pairing and phase fluctuations. *Phys. Rev. Lett.*, 95:110404, Sep 2005.

[45] Wilhelm Zwerger. *The BCS-BEC Crossover and the Unitary Fermi Gas*. Lecture Notes in Physics. Springer, Berlin, 2012.

[46] J. Carlson, S.-Y. Chang, V. R. Pandharipande, and K. E. Schmidt. Superfluid fermi gases with large scattering length. *Phys. Rev. Lett.*, 91:050401, Jul 2003.

[47] Evgeni Burovski, Nikolay Prokof'ev, Boris Svistunov, and Matthias Troyer. Critical temperature and thermodynamics of attractive fermions at unitarity. *Phys. Rev. Lett.*, 96:160402, Apr 2006.

[48] P Nozières and S. Schmitt-Rink. Bose condensation in an attractive fermion gas: From weak to strong coupling superconductivity. *J. Low Temp. Phys.*, 59:195, 1985.

[49] C. A. R. Sá de Melo, Mohit Randeria, and Jan R. Engelbrecht. Crossover from bcs to bose superconductivity: Transition temperature and time-dependent ginzburg-landau theory. *Phys. Rev. Lett.*, 71:3202–3205, Nov 1993.

[50] Jan R. Engelbrecht, Mohit Randeria, and C. A. R. Sáde Melo. Bcs to bose crossover: Broken-symmetry state. *Phys. Rev. B*, 55:15153–15156, Jun 1997.

[51] Roberto B. Diener, Rajdeep Sensarma, and Mohit Randeria. Quantum fluctuations in the superfluid state of the bcs-bec crossover. *Phys. Rev. A*, 77:023626, Feb 2008.

[52] A.L. Fetter and J.D. Walecka. *Quantum Theory of Many-Particle Systems*. Dover Books on Physics. Dover Publications, 2003.

[53] R. Combescot, M. Yu. Kagan, and S. Stringari. Collective mode of homogeneous superfluid fermi gases in the bec-bcs crossover. *Phys. Rev. A*, 74:042717, Oct 2006.

[54] J. Joseph, B. Clancy, L. Luo, J. Kinast, A. Turlapov, and J. E. Thomas. Measurement of sound velocity in a fermi gas near a feshbach resonance. *Phys. Rev. Lett.*, 98:170401, Apr 2007.

[55] M. Bartenstein, A. Altmeyer, S. Riedl, S. Jochim, C. Chin, J. Hecker Denschlag, and R. Grimm. Crossover from a molecular bose-einstein condensate to a degenerate fermi gas. *Phys. Rev. Lett.*, 92:120401, Mar 2004.

[56] P. Nozières and D. Pines. *Theory Of Quantum Liquids*. Number v. 1 in Advanced Book Classics. Perseus Books, 1999.

[57] M. Bartenstein, A. Altmeyer, S. Riedl, S. Jochim, R. Geursen, C. Chin, J. Hecker Denschlag, and R. Grimm. Exploring the BEC-BCS Crossover with an Ultracold Gas of ^{6}Li Atoms. In L. G. Marcassa and Kristian V. S. Bagnato, Helmerson, editors, *ATOMIC PHYSICS 19: XIX International Conference on Atomic Physics*, volume 770 of *American Institute of Physics Conference Series*, pages 278–288, May 2005.

[58] Michael Urban and Peter Schuck. Dynamics of a trapped fermi gas in the bcs phase. *Phys. Rev. A*, 73:013621, Jan 2006.

[59] Michael Urban. Radial quadrupole and scissors modes in trapped fermi gases across the bcs phase transition. *Phys. Rev. A*, 78:053619, Nov 2008.

[60] Alexander Altland and Ben Simons. *Condensed Matter Field Theory*. Cambridge University Press, 2006.

[61] Arun Paramekanti, Mohit Randeria, T. V. Ramakrishnan, and S. S. Mandal. Effective actions and phase fluctuations in d-wave superconductors. *Phys. Rev. B*, 62:6786–6799, Sep 2000.

[62] E. Taylor, A. Griffin, N. Fukushima, and Y. Ohashi. Pairing fluctuations and the superfluid density through the bcs-bec crossover. *Phys. Rev. A*, 74:063626, Dec 2006.

[63] N. Fukushima, Y. Ohashi, E. Taylor, and A. Griffin. Superfluid density and condensate fraction in the bcs-bec crossover regime at finite temperatures. *Phys. Rev. A*, 75:033609, Mar 2007.

[64] Edward Taylor. Phd thesis. *University of Toronto*, 2007.

[65] W. Vincent Liu. Theoretical study of the damping of collective excitations in a bose-einstein condensate. *Phys. Rev. Lett.*, 79:4056–4059, Nov 1997.

[66] J. Struck, C. Ölschläger, R. Le Targat, P. Soltan-Panahi, A. Eckardt, M. Lewenstein, P. Windpassinger, and K. Sengstock. Quantum simulation of frustrated classical magnetism in triangular optical lattices. *Science*, 333(6045):996–999, 2011.

[67] P. Soltan-Panahi, J. Struck, P. Hauke, A. Bick, W. Plenkers, G. Meineke, C. Becker, P. Windpassinger, M. Lewenstein, and K. Sengstock. Multi-component quantum gases in spin-dependent hexagonal lattices. *Nat. Phys*, 7(5):434–440, May 2011.

[68] D. Jaksch, C. Bruder, J. I. Cirac, C. W. Gardiner, and P. Zoller. Cold bosonic atoms in optical lattices. *Phys. Rev. Lett.*, 81:3108–3111, Oct 1998.

[69] N.W. Ashcroft and N.D. Mermin. *Solid State Physics*. Brooks Cole, Philadelphia, 1976.

[70] Immanuel Bloch, Jean Dalibard, and Wilhelm Zwerger. Many-body physics with ultracold gases. *Rev. Mod. Phys.*, 80:885–964, Jul 2008.

[71] Matthew P. A. Fisher, Peter B. Weichman, G. Grinstein, and Daniel S. Fisher. Boson localization and the superfluid-insulator transition. *Phys. Rev. B*, 40:546–570, Jul 1989.

[72] B. Capogrosso-Sansone, N. V. Prokof'ev, and B. V. Svistunov. Phase diagram and thermodynamics of the three-dimensional bose-hubbard model. *Phys. Rev. B*, 75:134302, Apr 2007.

[73] V. F. Mitrović, M. Horvatić, C. Berthier, G. Knebel, G. Lapertot, and J. Flouquet. Observation of spin susceptibility enhancement in the possible fulde-ferrell-larkin-ovchinnikov state of $cecoin_5$. *Phys. Rev. Lett.*, 97:117002, Sep 2006.

[74] M. Kenzelmann, Th. Strssle, C. Niedermayer, M. Sigrist, B. Padmanabhan, M. Zolliker, A. D. Bianchi, R. Movshovich, E. D. Bauer, J. L. Sarrao, and J. D. Thompson. Coupled superconducting and magnetic order in cecoin5. *Science*, 321(5896):1652–1654, 2008.

[75] G. Koutroulakis, M. D. Stewart, V. F. Mitrović, M. Horvatić, C. Berthier, G. Lapertot, and J. Flouquet. Field evolution of coexisting superconducting and magnetic orders in $cecoin_5$. *Phys. Rev. Lett.*, 104:087001, Feb 2010.

[76] Roberto Casalbuoni and Giuseppe Nardulli. Inhomogeneous superconductivity in condensed matter and qcd. *Rev. Mod. Phys.*, 76:263–320, Feb 2004.

[77] Daniel E. Sheehy and Leo Radzihovsky. Bec-bcs crossover, phase transitions and phase separation in polarized resonantly-paired superfluids. *Ann. Phys. (NY)*, 322(8):1790 – 1924, 2007.

[78] Leo Radzihovsky and Daniel E Sheehy. Imbalanced feshbach-resonant fermi gases. *Rep. Prog. Phys.*, 73(7):076501, 2010.

[79] Meera M. Parish, Stefan K. Baur, Erich J. Mueller, and David A. Huse. Quasi-one-dimensional polarized fermi superfluids. *Phys. Rev. Lett.*, 99:250403, Dec 2007.

[80] H. Müther and A. Sedrakian. Spontaneous breaking of rotational symmetry in superconductors. *Phys. Rev. Lett.*, 88:252503, Jun 2002.

[81] Armen Sedrakian, Jordi Mur-Petit, Artur Polls, and Herbert Müther. Pairing in a two-component ultracold fermi gas: Phases with broken-space symmetries. *Phys. Rev. A*, 72:013613, Jul 2005.

[82] W. Vincent Liu and Frank Wilczek. Interior gap superfluidity. *Phys. Rev. Lett.*, 90:047002, Jan 2003.

[83] Michael McNeil Forbes, Elena Gubankova, W. Vincent Liu, and Frank Wilczek. Stability criteria for breached-pair superfluidity. *Phys. Rev. Lett.*, 94:017001, Jan 2005.

[84] André Schirotzek, Cheng-Hsun Wu, Ariel Sommer, and Martin W. Zwierlein. Observation of fermi polarons in a tunable fermi liquid of ultracold atoms. *Phys. Rev. Lett.*, 102:230402, Jun 2009.

[85] Erhai Zhao and W. Vincent Liu. Orbital order in mott insulators of spinless p-band fermions. *Phys. Rev. Lett.*, 100(16):160403, Apr 2008.

[86] Congjun Wu. Orbital ordering and frustration of p-band mott insulators. *Phys. Rev. Lett.*, 100(20):200406, May 2008.

[87] Predrag Nikolić, A. A. Burkov, and Arun Paramekanti. Finite momentum pairing instability of band insulators with multiple bands. *Phys. Rev. B*, 81:012504, Jan 2010.

[88] Congjun Wu. Unconventional boseceinstein condensations beyond the "no-node" theorem. *Mod. Phys. Lett*, 23(1):1, 2009.

[89] Leo Radzihovsky and Sungsoo Choi. p-wave resonant bose gas: A finite-momentum spinor superfluid. *Phys. Rev. Lett.*, 103:095302, Aug 2009.

[90] B. S. Chandrasekhar. A note on the maximum critical field of high-field superconductors. *Appl. Phys. Lett.*, 1:7, 1962.

[91] A. M. Clogston. Upper limit for the critical field in hard superconductors. *Phys. Rev. Lett.*, 9:266–267, Sep 1962.

[92] A. E. Feiguin and F. Heidrich-Meisner. Pair correlations of a spin-imbalanced fermi gas on two-leg ladders. *Phys. Rev. Lett.*, 102:076403, Feb 2009.

[93] U. Schollwöck. The density-matrix renormalization group. *Rev. Mod. Phys.*, 77:259–315, Apr 2005.

[94] A. E. Feiguin and F. Heidrich-Meisner. Pairing states of a polarized fermi gas trapped in a one-dimensional optical lattice. *Phys. Rev. B*, 76:220508, Dec 2007.

[95] Erhai Zhao and W. Vincent Liu. Theory of quasi-one-dimensional imbalanced fermi gases. *Phys. Rev. A*, 78:063605, Dec 2008.

[96] Vadim Oganesyan, Steven A. Kivelson, and Eduardo Fradkin. Quantum theory of a nematic fermi fluid. *Phys. Rev. B*, 64:195109, Oct 2001.

[97] Benjamin M Fregoso et al. Biaxial nematic phases in ultracold dipolar fermi gases. *New J. Phys.*, 11(10):103003, 2009.

[98] Chungwei Lin, Erhai Zhao, and W. Vincent Liu. Liquid crystal phases of ultracold dipolar fermions on a lattice. *Phys. Rev. B*, 81:045115, Jan 2010.

[99] L. Radzihovsky. Quantum liquid-crystal order in resonant atomic gases. *ArXiv:1112.0773*, December 2011.

[100] X.-G. Wen. *Quantum Field Theory of Many-Body Systems*. Oxford Univ. Press, 2004.

[101] H. Ehrenreich and M. H. Cohen. Self-consistent field approach to the many-electron problem. *Phys. Rev.*, 115:786–790, Aug 1959.

[102] S. Biermann, A. Georges, A. Lichtenstein, and T. Giamarchi. Deconfinement transition and luttinger to fermi liquid crossover in quasi-one-dimensional systems. *Phys. Rev. Lett.*, 87(27):276405, Dec 2001.

[103] Thierry Giamarchi. *Quantum Physics in One Dimension*. Oxford University Press, 2004.

[104] R. Shankar. Renormalization-group approach to interacting fermions. *Rev. Mod. Phys.*, 66(1):129–192, Jan 1994.

[105] S. A. Kivelson, E. Fradkin, and V. J. Emery. Electronic liquid-crystal phases of a doped mott insulator. *Nature*, 393(6685):550–553, June 1998.

[106] Kai Sun, Benjamin M. Fregoso, Michael J. Lawler, and Eduardo Fradkin. Fluctuating stripes in strongly correlated electron systems and the nematic-smectic quantum phase transition. *Phys. Rev. B*, 78:085124, Aug 2008.

[107] Hong Yao, John A. Robertson, Eun-Ah Kim, and Steven A. Kivelson. Theory of stripes in quasi-two-dimensional rare-earth tellurides. *Phys. Rev. B*, 74:245126, Dec 2006.

[108] Zi Cai et al. Stable fulde-ferrell-larkin-ovchinnikov pairing states in two-dimensional and three-dimensional optical lattices. *Phys. Rev. A*, 83:063621, Jun 2011.

[109] Hirokazu Miyake, Georgios A. Siviloglou, Graciana Puentes, David E. Pritchard, Wolfgang Ketterle, and David M. Weld. Bragg scattering as a probe of atomic wave functions and quantum phase transitions in optical lattices. *Phys. Rev. Lett.*, 107:175302, Oct 2011.

[110] Matthias Troyer and Uwe-Jens Wiese. Computational complexity and fundamental limitations to fermionic quantum monte carlo simulations. *Phys. Rev. Lett.*, 94:170201, May 2005.

[111] Zi Cai and Congjun Wu. Complex and real unconventional bose-einstein condensations in high orbital bands. *Phys. Rev. A*, 84:033635, Sep 2011.

[112] Matthias Weidemüller, Andreas Hemmerich, Axel Görlitz, Tilman Esslinger, and Theodor W. Hänsch. Bragg diffraction in an atomic lattice bound by light. *Phys. Rev. Lett.*, 75(25):4583–4586, Dec 1995.

[113] Guifré Vidal. Efficient classical simulation of slightly entangled quantum computations. *Phys. Rev. Lett.*, 91:147902, Oct 2003.

[114] Guifré Vidal. Efficient simulation of one-dimensional quantum many-body systems. *Phys. Rev. Lett.*, 93:040502, Jul 2004.

[115] Simon Fölling *et al.* Spatial quantum noise interferometry in expanding ultracold atom clouds. *Nature*, 434:481, March 2005.

[116] K. Kumagai, H. Shishido, T. Shibauchi, and Y. Matsuda. Evolution of paramagnetic quasiparticle excitations emerged in the high-field superconducting phase of $cecoin_5$. *Phys. Rev. Lett.*, 106:137004, Mar 2011.

[117] Immanuel Bloch. Ultracold quantum gases in optical lattices. *Nat. Phys*, 1(1):23–30, October 2005.

[118] R. B. Diener and T.-L. Ho. The Condition for Universality at Resonance and Direct Measurement of Pair Wavefunctions Using rf Spectroscopy. *eprint arXiv:cond-mat/0405174*, May 2004.

[119] M. Holland, S. J. J. M. F. Kokkelmans, M. L. Chiofalo, and R. Walser. Resonance superfluidity in a quantum degenerate fermi gas. *Phys. Rev. Lett.*, 87:120406, Aug 2001.

[120] G. M. Bruun and C. J. Pethick. Effective theory of feshbach resonances and many-body properties of fermi gases. *Phys. Rev. Lett.*, 92:140404, Apr 2004.

[121] Mohit Randeria, Ji-Min Duan, and Lih-Yir Shieh. Superconductivity in a two-dimensional fermi gas: Evolution from cooper pairing to bose condensation. *Phys. Rev. B*, 41:327–343, Jan 1990.

[122] A. J. Moerdijk, B. J. Verhaar, and A. Axelsson. Resonances in ultracold collisions of ^{6}Li, ^{7}Li, and ^{23}Na. *Phys. Rev. A*, 51:4852–4861, Jun 1995.

[123] Cheng Chin, Rudolf Grimm, Paul Julienne, and Eite Tiesinga. Feshbach resonances in ultracold gases. *Rev. Mod. Phys.*, 82:1225–1286, Apr 2010.

[124] N. Nagaosa. *Quantum Field Theory in Condensed Matter Physics*. Texts and Monographs in Physics. Springer, 1999.